Study of Lipid Coatings on Titanium Surfaces by X-ray and Neutron Scattering Techniques

Dissertation

zur Erlangung des Doktorgrades

des Department Physik

der Universität Hamburg

vorgelegt von

Maksym Golub

aus Chernigov, Ukraine

Hamburg

2014

Gutachter der Dissertation:

Prof. Dr. A. Schreyer

Prof. Dr. R. Willumeit

Gutachter der Disputation:

Prof. Dr. A. Schreyer

Dr. V. Haramus

Datum der Disputation:

14. March 2014

Vorsitzender des Prüfungsausschusses:

Prof. Dr. H. P. Oepen

Vorsitzender des Promotionsausschusses:

Prof. Dr. D. Pfannkuche

Leiter des Departments Physik:

Prof. Dr. P. Hauschildt

Dekan der MIN-Fakultät:

Prof. Dr. H. Graener

Abstract

Permanent implants made from titanium and its alloys are widely used and successfully implemented in medicine to address problems related to orthopedic and oral disorders. However, artificial implants that interact optimally and durable with bone tissue have yet to be developed. Here, we suggest a lipid coating to partially mimic the biological cell membrane. This thesis is focused on finding the most appropriate method to deposit POPE lipids on titanium surfaces. This is important for future applications on real implant materials. Two approaches are considered for lipid deposition.

The first approach is controlled deposition, which includes Langmuir-Blodgett and Langmuir-Schaefer techniques in combination with a previously covalently attached monolayer of N-octadecylphosphonic acid. A neutron specular reflectivity experiment permits the determination of the efficiency of the controlled deposition at each step.

The second approach considered in this work is lipid adhesion from organic solvents. Here it is shown that the simple drop deposition, which can be successfully applied to make a lipid multilayer stack on a surface, is not an appropriate method for lipid deposition on a titanium surface. To improve the homogeneity of the POPE distributions on the metal surface, a spray coating is applied. The spray coating is assessed under dry and liquid conditions using a combination of X-ray and neutron scattering techniques. The spray coating leads to two types of multilamellar POPE structures. These coatings are stable in a liquid environment in the range of physiological temperatures. A simultaneous analysis of the specular and off-specular data provides structural information necessary to assess the quality of the coating for future applications.

Abstract

Permanente Implantate aus Titan und seine Verbindungen werden schon intensiv genutzt und im medizinischen Bereich erfolgreich bezüglich orthopädischer und oraler Störungen eingesetzt. Künstliche Implantate, die optimal und ausdauernd mit dem Knochengewebe wechselwirken, müssen jedoch noch entwickelt werden. Wir schlagen hier eine Lipidbeschichtung vor, die zum Teil biologische Zellmembrane nachahmen. Die Arbeit ist fokussiert auf das Bestimmen der besten Anwendung auf realen Implantat-Materialien. Zwei Ansätze werden hierbei für das Aufbringen der Lipide betrachtet:

Der erste Ansatz besteht in der kontrollierten Aufbringung, welches die Langmuir-Blodgett und Langmuir-Schäfer Techniken umfassen in Kombination mit einer kovalent gebundenen Monolagenschicht aus N-Octadecyl-Phosphat-Säure. Spekuläre Neutronenreflektivitäts-messungen erlauben die Bestimmung der Effizienz der kontrollierten Aufbringung in jedem Schritt.

Der zweite Ansatz, der in dieser Arbeit berücksichtigt wird, ist die Adhäsion der Lipiden von organischen Lösungen. Hier wird gezeigt, dass die einfache Tropfenablagerung, die erfolgreich für die Herstellung von Lipid Vielschichtlagensystemen auf Oberflächen angewandt wird, keine geeignete Methode für die Lipiddeposition auf Titanoberflächen ist. Um die Homogenität der POPE Verteilung auf der Metalloberfläche zu verbessern, wird hier eine Sprühauftragung angewandt. Diese Methode wurde untersucht unter trockenen und flüssigen Rahmenbedingungen mittels einer Kombination aus Röntgen und Neutronenstreutechniken. Die Sprühauftragung führt dabei zu zwei Arten von multilamellaren POPE Strukturen. Diese Beschichtungen sind stabil in flüssigen Umgebungen in dem Bereich von physiologischen Temperaturen. Eine simultane Analyse der spekulären und off-spekulären Streudaten liefert die strukturellen Informationen, die notwendig ist, um die Qualität der Beschichtungen für zukünftige Anwendungen zu bewerten.

1 Introduction

The use of medical implants as a safe, long-term solution for musculoskeletal system problems is rapidly increasing. Their use has changed dramatically in recent decades due to increased life expectancy, changing lifestyles and improved implant technology [1]. Annually orthopedic, oral and maxillofacial disorders affect millions of patients. Diseases and problems caused by damaged or diseased bone tissue represent a global annual cost of more than 40 billion Euros [2]. Furthermore, the rapid worldwide increase in the number of elderly people with different types of degenerative-dystrophic changes, such as osteoarthritis and rheumatoid arthritis [3], requires more durable implants (f.e. knee or hip joints) that can function even in the presence of compromised health conditions [4]. Modern science has provided novel insights into the biological mechanisms responsible for bone healing. These achievements have facilitated the development of artificial implants that interact optimally with the bone tissue with a so-called “smart implant surface”. Consequently, implants have become increasingly important in regaining health and improving quality of life.

The materials that are implanted in bone tissue must be non-toxic, non-immunogenic, non-thrombogenic, and non-carcinogenic [5]. Due to the formation of a thin but a very stable oxide layer on the surface [6] which offers the aforementioned properties, titanium and its alloys have become preferred materials. In addition they off a high specific strength which makes the implant safe even under high-load conditions such as stumbling or jumping.

Several attempts have been made to develop new implant surface modifications that may prolong the lifespan of an implant and ensure quicker and more stable implant incorporation, therefore decreasing patient recovery time. To obtain biologically active materials that provide biological cues for tissue regeneration, various coatings have been applied. Phospholipid coatings on titanium surfaces have been intensively studied in terms of adhesion, the proliferation and differentiation of human bone-derived cells (HBDC) [7], human chondrocytes, human mesenchymal stem cells and macrophage stimulation [8]. These coatings have been shown to be a positive factor for cell-implant interactions.

In this work, the lipid POPE (phospholipids 1-palmitoyl-2-oleoyl-sn-glycero-3-phospho-ethanolamine) was used. POPE contains the polar head group

phosphatidylethanolamine (PE), which is one of the most common head groups found in nature. This polar group is found in all living cells and comprises up to 30% of membrane phospholipids. In humans, PE is found in nervous tissue, such as the white matter of the brain, nerves, neural tissue, and in the spinal cord [9]. In addition, PE is thought to be important in the heart. When blood flow to the heart is restricted, the asymmetrical distribution of PE between membrane leaflets is disrupted, resulting in membrane disruption [10].

POPE lipid has two, non-identical alkyl chains. One alkyl chain is saturated, while the other is unsaturated at position C_9-C_{10} (see Figure 1). POPE was used in this investigation due to its unique biophysical properties, such as polymorphism, i.e., the ability to form inverse hexagonal structures, which is a prerequisite for cell division [11].

An important physical characteristic of phospholipids is the phase transition from the crystalline solid state to the crystalline fluid state. This face transition occurs at the melting temperature, which is 25 °C for POPE [12].

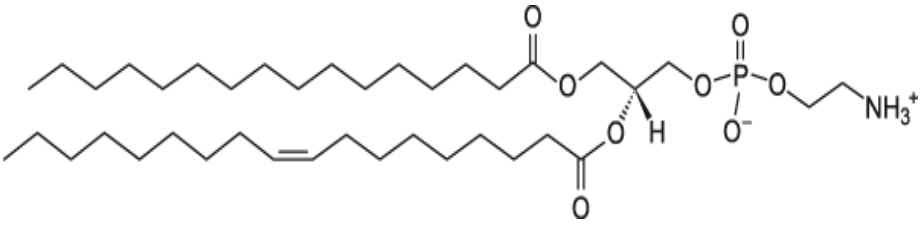

Figure 1. Schematic of the POPE molecule [12]

In general, a lipid coating in contact with water or a humid environment is a self-organized system. POPE will form bilayers with a repeat d-spacing due to the hydration force, which leads to bilayer formation, and to the van der Waals force, which limits the hydration of bilayers [13].

The main objects of this investigation are the POPE multilayer and the alteration of its surface upon exposure to water, growth medium and growth medium containing human serum albumin (HSA), conditions that favor cell adhesion. The study of the structure of the multilayer, including the structure normal to the surface and the lateral structure, will facilitate the identification of key parameters to understand the interaction between cells and lipid-coated implants.

The selected protein, HSA ($C_{2918}H_{5691}O_{1473}N_{786}S_{41}$), is an important blood protein for which the molecular dimensions are well known [14]. Crystallographic data suggest that the quaternary structure of HSA is heart-shaped (see Figure 2) with a

width of 82 Å, a maximum dimension from the apex of the heart to the end of the domains on each side of 83 and 70 Å, respectively, and a depth of approximately 30 Å [15, 16].

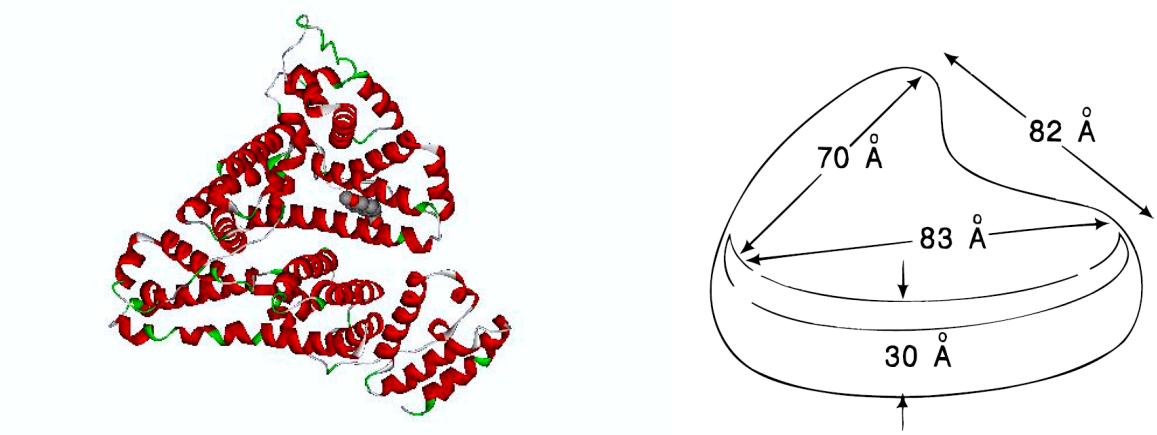

Figure 2. HSA molecule [14, 17]

It is interesting to elucidate the changes in thickness and structure of the lipid film in contact with liquids. In addition, it is unclear if the actual trigger for the improved cell reaction is the thick, soft and liquid crystalline surface supplied by the lipids or the protein coating on the lipid layers

The phospholipid coating of the implant surface must remain stable in body fluids and at implant site. One would expect that this coating is not stable in liquid environments because phospholipid molecules tend to form micelles or vesicles in water, and thus, the coating might disappear over time. One potential means of improving the stability of the coating is to create a strong van der Waals interaction between the implant surface and the phospholipid coating. This interaction can be obtained by generating an appropriate interface between the metal surface and the phospholipid layer(s). In this study, the implant surface was coated by a self-assembled monolayer (SAM) of OPA (n-octadecylphosphonic acid - $C_{18}H_{38}O_3P$). The SAM of OPA forms a highly stable phosphate-metal cation under specific conditions (e.g., temperature) because the affinity of the phosphate of the OPA molecule for Ti(IV) is very high. These bonds directly link the phosphate head group to the metal cation through either one oxygen atom (monodentate) or two oxygen atoms (bidentate) [18]. The hydrophobic surface then formed by the alkyl chains will offer a more stable configuration for stronger van der Waals interactions with the phospholipids than the configuration without OPA thin films [19].

Therefore, the main goals of the present work are the following: 1) to determine which method of lipid deposition provides a more stable and uniform lipid structure on a titanium surface; and 2) to study the lipid bilayer structure under different environmental conditions, such as air, water, growth medium and growth medium containing human serum albumin.

In this work, X-rays and neutron scattering techniques were utilized to investigate the lipid coating on a Ti surface. These methods permitted the investigation of the structure and interaction of the lipid bilayer with membrane-active molecules, such as proteins [20]. Of the methods that have been used to study ultra-thin organic films, the X-ray and neutron reflectivity techniques are two of the most appropriate [21]. Both techniques are very sensitive to changes in the scattering length density (SLD) profile normal to the interface. This profile can be defined with angstrom resolution [22]. These techniques also facilitate the investigation of the lateral structure within the bilayers.

While X-ray reflectivity technique allows to reach a higher Q range compare to the neutron reflectivity technique [22], for biological subjects, the neutron reflectivity technique is particularly useful because the high penetration depth of neutrons in silicon permits measurement at solid/liquid interphase [23]. In addition, the neutron SLD of alkyl chains, D_2O and titanium are very different, permitting enhanced contrast for the self-assembled lipid bilayers.

2 Materials and Methods

2. 1 Sample Preparation

2. 1. 1 Sputter Deposition Technique

For X-ray reflectivity, two model implant surfaces were used: a layer of titanium (99.7% pure, PureTech, New York, USA) that was sputtered on top of a silicon substrate (DXL Darmstadt, Germany) with a polished surface and a layer of titanium alloy (87% - Ti, 6% - Al, 7% - Nb 99.7% pure, PureTech, New York, USA).

For the neutron reflectivity experiments, only titanium was deposited on a silicon crystal (dimension 8x5x1 cm) with a polished surface provided by Siltronix Archamps Technopole (Archamps, France). The model implant surfaces for the X-ray experiments and for the neutron experiments were different due to the setups of the instruments, however, since the surface chemistry remained unaffected, it was expected that the lipid coatings were identical for the all used specimens.

All depositions on the silicon bases were performed at the Helmholtz Zentrum Geesthacht (HZG) by a magnetron sputter deposition chamber capable of handling large substrates [24]. The chamber operated with a base pressure P_{base} in the range of 10^{-8} mBar and a working Ar pressure $P_{working}$ of $0.2x10^{-3}$ mBar (see Figure 3 for a schematic representation of the chamber).

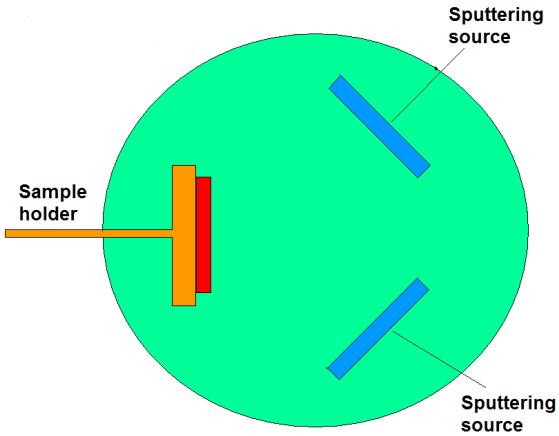

Figure 3. Schematic representation of the HZG sputter deposition chamber

The advantages of the magnetic field sputtering technique are the increase in the ionization probability for the working gas before recombination and the increased efficiency with which the ionized working gas atoms are directed toward the target surface. These two effects allow the working gas pressure to be decreased to 10^{-3} mBar, enabling a cleaner deposition process.

The two circular (7.6 cm in diameter) magnetron sputter sources were installed in the high-vacuum sputter chamber. To ensure more homogeneous film thicknesses, the substrate was rotated around its normal. The samples were loaded through a special airlock system to avoid disrupting the vacuum. Implementation of a nitrogen cryostat in the chamber increased the quality of the vacuum. The temperature of the substrate during the coating process was measured using a thermostat connected to the bottom of the substrate and was maintained at 25±3°C, as monitored by a Pt/PtHh thermocouple. The distance between the substrate and the sputter sources was approximately 25 cm, and the angle to the substrate normal was 22.5°. The deposition speed was 0.04 nm per second, and thus, the amount of deposited titanium can be predicted based on the time of deposition. However, the precise thickness of the deposited titanium layer and the thickness of the titanium dioxide layer, which appears immediately when the titanium surface is in contact with air, must be determined by X-ray (neutron) reflectometry.

2. 1. 2 Lipid Absorptive Deposition

In this experiment, we examined a POPE lipid covering obtained by dropping or spreading lipids from a methanol-chloroform solution on a silicon block coated with a titanium layer; the concentration was 1 mmol POPE (20% methanol and 80% chloroform). The concentration of lipids in the solvent solution and the amount of deposited solution remained constant for both deposition techniques. For lipid spreading, the air brush was connected to a weak flow of nitrogen (0.5 Bar). After coating, to evaporate the solvent from the surface, the samples were dried by a steam of nitrogen for 30 seconds. The amount of the deposited solution (0.25 μL) and the area of the substrate (4 cm^2) were constant throughout the experiment. In the case of X-ray experiment measurements were usually taken the next day after the samples were covered with or immersed in fluid. During that day, the sample was kept in air at a temperature lower than the phase transition temperature of POPE lipids. For the neutron experiment a spray coating was first measured in D_2O, and the D_2O was then exchanged with D_2O-based growth medium or D_2O-based growth medium with deuterated HSA. Growth medium powder was dissolved at 0.02 g of growth medium powder per 1 mL of D_2O. All samples were kept in a liquid environment for at least 2 hours before beginning measurement; some measurements were repeated to confirm the stability of the system and the

reproducibility of the effects. The sample cells were connected to a water-cooled thermostat to maintain a constant temperature of 20 °C during all measurements.

Growth medium powder was dissolved at a concentration of 0.02 g per 1 mL water. Two types of DMEM powder were used: growth medium containing Na-pyruvate and 1 g/L D glucose and growth medium without Na-pyruvate containing 4.5 g/L D glucose. All samples were kept in a liquid environment for at least 2 hours before the beginning of the measurement.

2. 1. 3 Controlled Deposition

2. 1. 3. 1 OPA Coating

The OPA coating procedure relies on the T-BAG (Tethering by Aggregation and Growth) technique, which is a simple method for the synthesis of self-ordered, self-assembled and continuous monolayers. The procedure was adapted from [25]. The samples were cleaned with double-distilled water, followed by acetone (Sigma-Aldrich Chemie GmbH, Munich, Germany) and finally methanol (Sigma-Aldrich Chemie GmbH, Munich, Germany). The strongly bound monolayer film of OPA on the native oxide surface of the Ti samples was obtained by immersion in and slow evaporation of a dry tetrahydrofuran solution of OPA (Sigma-Aldrich Chemie GmbH, Munich, Germany). The concentration of the diluted solution was 33.4 mg of OPA in 100 mL of tetrahydrofuran. After heating at 120 °C for 64 hours, unbound OPA was removed by sonication of the specimen in tetrahydrofuran, followed by in methanol (Sigma-Aldrich Chemie GmbH, Munich, Germany). This procedure should result in the production of a homogeneous OPA monolayer on the metal surface.

2. 1. 3. 2 Langmuir – Blodgett Deposition

To prepare the asymmetric lipid bilayers, the Langmuir-Blodgett (LB) technique was used. Here, we used a Langmuir-Blodgett Trough Nima 611 [26], which has a special reservoir for large-sized samples (5x8x1 cm). The monolayer of POPE lipids was formed in a LB reservoir filled with water in between two special barriers. These barriers controlled the surface tension of the monolayer. The principle of the LB deposition is illustrated in Figure 4.

The formation of a lipid monolayer is based on the properties of phospholipids, which orient themselves at the air/water interface to minimize their free energy and

form an insoluble monolayer called a Langmuir film [27]. After dropping a dilute solution of POPE in methanol-chloroform (20% methanol and 80% chloroform), molecules of POPE were spread over the interface. A monolayer was formed after solvent evaporation. It was assumed that the surface tension between the barriers in the LB reservoir was stabilized when the solvent evaporation was complete. In the next step, the surface tension of the monolayer of POPE was driven to 35 mN/m^2 by changing the area between the barriers. This value of surface tension, which was stably maintained throughout the deposition process, is in the range at which the POPE molecules in the monolayer are in the liquid-condensed phase [28]. Moreover, this value in agreement with the constraint of the density of lipids in a bilayer within narrow limits equivalent to surface pressures in a monolayer in the region of 32–34 mN/m^2 [29].

After preparing the monolayer, the deposition process was initiated. Phospholipids are supported on the top of the Ti coated Si-crystal. This crystal was previously coated with OPA as described above.

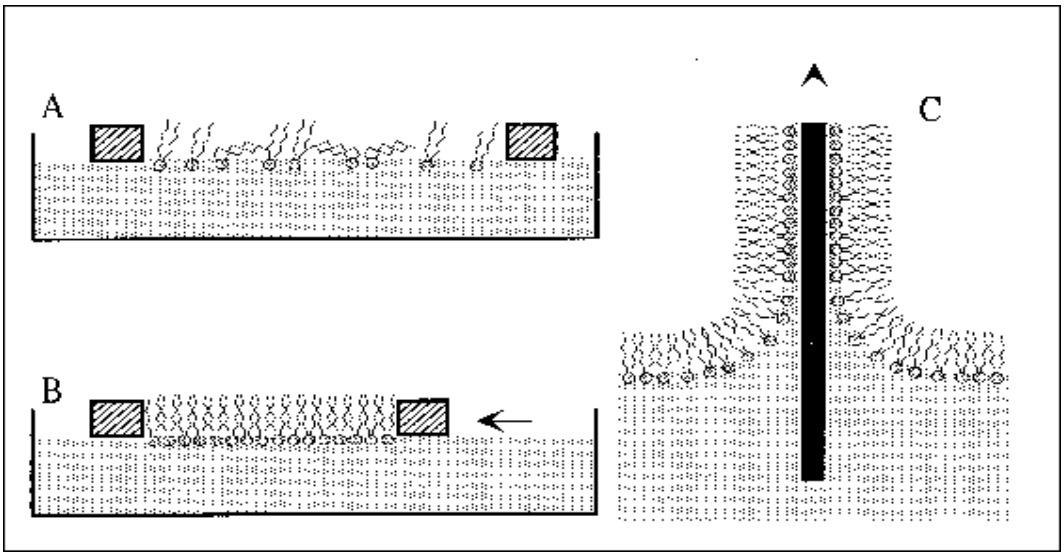

Figure 4. The principle of Langmuir-Blodgett deposition [30]

The transfer of POPE lipids onto the OPA-coated specimen was performed in three steps:

1) Dipping the crystal through the monolayer of lipids into the subphase while keeping the crystal perpendicular to the water surface.

2) Moving the crystal up from the subphase though the monolayer of lipids while keeping the crystal perpendicular to the water surface, as in the previous step.

3) Pushing the crystal through the monolayer of lipids while keeping the crystal parallel to the water surface.

The speed of dipping and moving up was the same, 0.2 mm per second – the lowest speed for this device. For the third step, the speed was 5 mm per second – the highest speed for this device.

This sample prepared according to the three steps described above was probed only by neutron reflectivity because it had to remain in liquid after the last step of the deposition procedure.

The materials and chemicals used are described in Table 1.

Table 1. Materials

Deposition materials	Purity (%)	Supplier
Titanium	99.7	PureTech, New York, USA
Titanium alloy	99.7	PureTech, New York, USA
Substrates	Supplier	
Silicon wafer	DXL dynacore GmbH, Darmstadt, GermanySilicon wafer	
Silicon crystal	Siltronix Archamps Technopole, Archamps, France	
Solvents	Purity (%)	Supplier
Methanol		Sigma-Aldrich Chemie GmbH, Munich, Germany
Acetone		Sigma-Aldrich Chemie GmbH, Munich, Germany
Tetrahydrofuran		Sigma-Aldrich Chemie GmbH, Munich, Germany
Chemicals	Purity (%)	Supplier
OPA		Sigma-Aldrich Chemie GmbH, Munich, Germany
POPE		Sigma-Aldrich Chemie GmbH, Munich, Germany
Deuterated HSA		Grenoble, France
Growth medium		Biouchrom AG, Berlin, Germany

2. 2 Sample Analysis Techniques

2. 2. 1 Atomic Force Microscopy (AFM)

AFM provides a three-dimensional surface profile. The principle behind this technique is the measurement of the force of interaction between a very sharp tip (usually less than 100 Å in diameter) and the surface of a sample (see Figure 5). The tip is located on the free end of a cantilever 100 μm to 200 μm in length. The greatest advantage of AFM is that it avoids the risk of damaging/changing the sample surface, e.g., by metal/carbon coatings, inherent in the use of other techniques. The van der Waals interaction between the tip and the surface leads to the deflection of the cantilever according to Hooke's law. This deflection is usually measured with a laser and photodiodes.

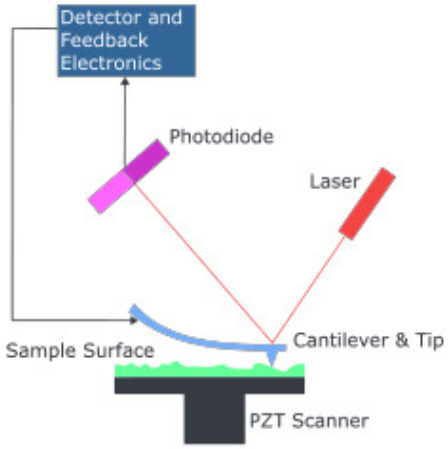

Figure 5. Diagram of AFM [31]

There are two basic modes of AFM operation: static and dynamic. In static (contact) mode, the cantilever deflection is kept constant, while in dynamic ("tapping") mode, the cantilever is vibrated and is only periodically tapped onto the surface. Both regimes of AFM operation give the local sample height, which can be presented as a map of the surface topography. For biological objects, the "tapping" mode is preferable because it leads to less surface damage.

In this investigation, samples were probed in HZG with a Park AFM XE-100 (Schaerfer Technologie, Langen, Germany) [32]. Depending on the type (contact mode or tapping mode) of measurement, contact cantilevers PSIA 910M-NSC36 or non-contact PSIA cantilevers 910M-NCHR (Schaerfer Technologie, Langen, Germany) were used.

2. 2. 2 Scanning Electron Microscopy (SEM)

In SEM, a surface is scanned by a focused beam of electrons whose energy is higher than that of the ionization potential. Due to the interaction of the beam with the electrons of the investigated surface, several signals that contain information about the composition and topology of the surface can be detected. In general, two types of signals are used: second electrons (SE) and back scattered electrons (BSE). SE are a result of the emission of electrons by the surface due to hitting by the beam. The SE signal is useful for obtaining high-resolution images of surfaces. The magnification of such images is 500 times better than the best light microscope and is limited only by the wavelength of the electrons. The BSE signal represents electrons reflected from a surface by elastic scattering. This regime is useful for clarifying a chemical distribution over a surface because BSE depends on the atomic number of the specimen.

In this investigation, SEM measurements were performed with the Auriga scanning electron microscope (Zeiss, Oberkochen, Germany) shown in Figure 6. Both SE and BSE regimes were probed. SEM images were acquired at an accelerating voltage of 1-6 kV with the SE detector or the InLens detector, which collects both SE and BSE signals.

In addition to the SEM experiments, element mapping was performed with 7 regions of interest in the respective dispersive X-ray spectrum, Ti, Al, Nb, C, P, O, and Si, to identify the element distribution of a biomimetic model implant.

For some POPE-coated samples, a cut was made with a Ga beam with an energy of 30 kV. The cut was made to assess the thickness of the POPE coating.

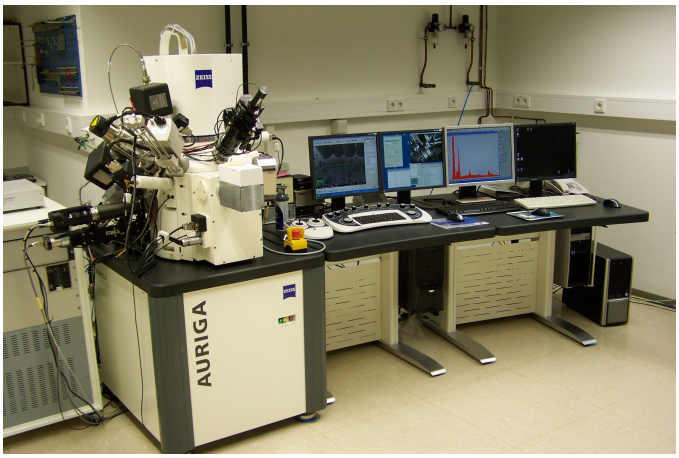

Figure 6. Scanning electron microscope Auriga

All measurements were performed under vacuum (8 10^{-5} mBar). The distance between the electron gun and the surface was maintained at 4.7 mm during the measurements. The aperture size was 30 μm.

SEM is able to provide images of POPE-coated titanium implants on the micrometer scale without an additional coating of the surface by conducting glue. No damage to the POPE coating was detected after SEM scanning. The test measurement, which was performed as a few repeated scans of the same region, did not indicate any changes in the SEM images afterwards. *In situ* measurements were not performed because the samples for SEM must be completely dry due to the high vacuum in the sample chamber.

2. 2. 3 X-ray Diffractometer RöDi

The X-ray experiments were performed at HZG with a XRD 3003 PTS X-ray diffractometer (Seifert & Co, Germany) using a Cu tube [33] (CuKα radiation λ=1.541 Å) and a Göbel mirror for vertical collimation onto a sample to increase the intensity. The scattering plane lies in the horizontal direction.

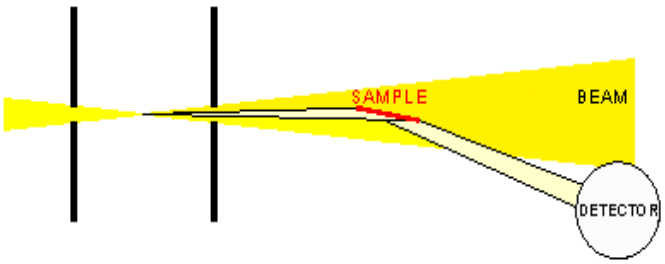

Figure 7. Model of the over- illumination effect [34]

The measured intensity of the scattered beam must be altered in correspondence with the width of the incident beam and sample size. At very small angles, part of the full beam does not hit the sample surface and thus does not contribute to the scattering process, which must be corrected with a so-called footprint correction. Because the sample's shape is rectangular and the beam is defined by a slit with a width W of 0.2 mm, the footprint correction can be written as:

$$C(\theta_i) = \frac{W}{L \sin \theta_i} \quad \text{for } \sin\theta_i < W/L$$

For $\sin\theta_i \geq W/L$, $C(\theta_i)$ is 1 [35], L is the length of the sample (2 cm in our case), θ_i is the incident reflection angle with respect to the sample surface, and θ_f indicates the

corresponding angle of the reflected beam and is equal to the incident angle θ_i for the specular reflectivity measurement.

To evaluate the specular X-ray spectra, the diffuse background must be subtracted from the measured reflectivity scan. The latter can be recorded by an offset scan, which is a longitudinal scan with a slight offset in the θ-2θ condition ($\theta_i \neq \theta_f$) [36]. The momentum transfer along the sample plane and sample normal, Q_x and Q_z, respectively, can be calculated as

$$Q_z = (2\pi/\lambda)(\sin\theta_i + \sin\theta_f) \quad (1)$$

$$Q_x = (2\pi/\lambda)(\cos\theta_f - \cos\theta_i) \quad (2)$$

The more detailed theoretical description is given in Chapter 2. 3. 1. In the first approximation, Q_x can be considered to be constant if the offset is small.

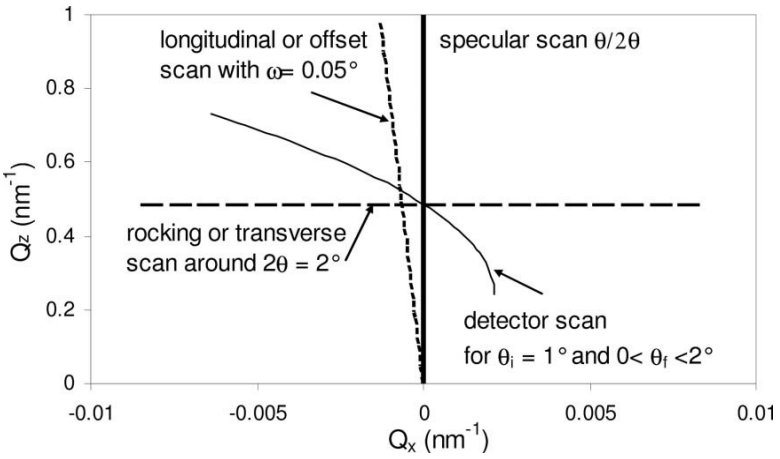

Figure 8. Schematic representation of reciprocal space [34]

The offset used in the experiment was equal to 0.05 degree, which was determined by rocking scans at several selected positions to ensure that we are far enough to avoid any specular contributions as well as close enough to detect the real background signal.

The main drawback of the method is that the reflectivity curves for nonmagnetic systems cannot be interpreted unambiguously. In general it is possible to build a family of scattering length density profiles that result into the same reflectivity curve [35] because only the scattered intensity is detected without any phase information of the interfering waves. In order to receive a realistic model of the sample some additional information has to be taken into account. The final models presented here are chosen as the most reasonable models. The other shortcoming of the experiment on RöDi is that there is no sample cell for the environment condition control, therefore all samples were measured at dry conditions and at a room temperature.

2. 2. 4 Neutron Membrane Diffractometer V1

The diffractometer used in this work is located in the curved neutron guide NL 1A (Helmholtz Zentrum Berlin). The vertically focusing graphite monochromator provides a beam with a constant wavelength, which can be selected in the range of 3-6 Å [37]. The maximum Q value is limited (2.2 $Å^{-1}$) by the Be filter. The V1 diffractometer is equipped with a high-resolution area detector – the sensitive area is 19x19 (cm) with a spatial resolution of 1.5x1.5 (mm). The setup of this instrument is particularly useful for investigating biological samples when temperature and humidity control are available. A more detailed description of this instrument can be found elsewhere [38, 39].

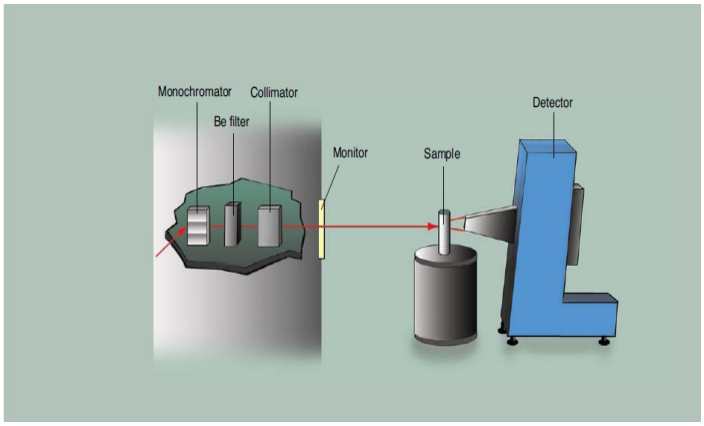

Figure 9. Illustration of the V1 diffractometer (Helmholtz Zentrum Berlin) [40]

Due to the structure of the sample holder, the samples were placed vertically in a special aluminum cylinder. The environmental humidity inside the sample chamber was kept stable (98%) by adding a solution of K_2SO_4 salt in water to a special Teflon bath at the base of the aluminum container. The ability to conduct measurements at 98% humidity is the advantage of this experiment technique compared to X-ray measurements, which must be conducted under dry conditions. POPE lipids were placed on the mica plate by dropping them into methanol-chloroform solution. The sample was measured at two temperatures, 20 °C and 37 °C, to obtain a SLD profile at the gel phase and the liquid crystalline phase.

To perform the contrast variation experiment, we used three compositions of D_2O:H_2O: 8%, 20% and 50% D_2O in H_2O. To achieve equilibrium inside the chamber, the samples with different D_2O compositions were kept in the chamber for at least 24 hours prior to measurement. During the diffraction experiment, rocking scans were performed for five orders of Bragg peaks by rocking the samples around

the expected position θ by θ ± 2°. The time of the measurement for each peak was chosen based on the intensity of the reflection and varied from 20 min to 6 hours. All measurements were repeated to confirm the experimental reproducibility of the intensity and peak positions.

2. 2. 5 Neutron Monochromatic Reflectometer V6

When applying monochromatic reflectometers, the wavelength is fixed (4.66 Å for the V6 reflectometer at HZB). A beam of neutrons for this type of instrument can be obtained by using a single crystal as a monochromator so that only neutrons with a fixed wavelength are reflected, as defined by Bragg's law. Reflectivity curves are obtained by changing the incident angle.

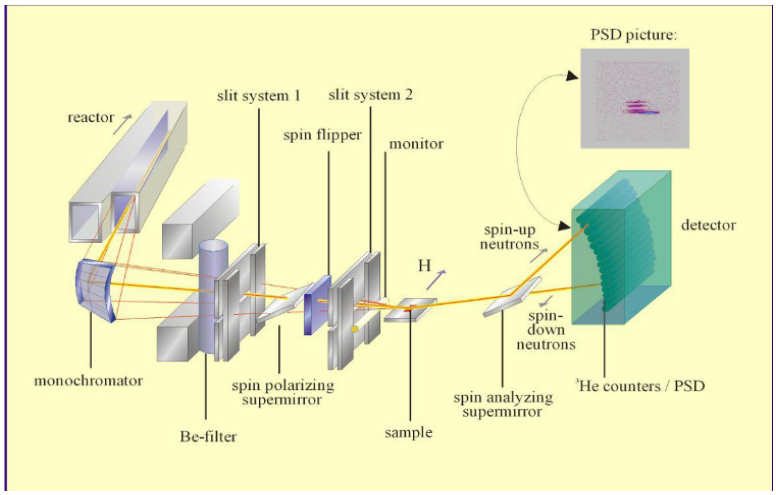

Figure 10. Schematic diagram of the V6 reflectometer (Helmholtz Zentrum Berlin) [41]

The graphite monochromator permits a lambda resolution of 2%. Together with the collimation slit system, the monochromator gives a constant ΔQ resolution of 0.002 $Å^{-1}$. A detailed description of the instrument can be found elsewhere [41]. The range of the incident angle was 0.1-3.4 degree, enabling the measurement of a reflectivity curve up to Qz = 1.6 $Å^{-1}$. For data collection, a 2D detector was used to enable the measurement of both diffuse and specular scattering. The neutron beam was targeted by a slit in front of the sample with dimensions of 0.5x24 mm^2.

The coated substrate was a pure silicon crystal with a polished surface provided by Siltronix. According to the X-ray reflectivity measurement, the roughness of the surface was about 7 Å. The lipid coating was prepared with an air brush using the method described in Section 2. 1. 2. The sample was measured against D_2O or D_2O/H_2O mixtures. These measurements were repeated after some time (the time in

between two measurements was 5-16 hours) to assess the stability of the coating. The temperature inside the sample cell remained constant at 20 °C throughout the experiment.

2. 2. 6 Time of Flight Reflectometer Figaro

In time-of-flight reflectometers, a pulsed of a white neutron beam, which is selected by a chopper, is directed onto the sample. The incident angle is fixed; thus the reflectivity curve is obtained by measuring the reflectivity signal for each wavelength of the available spectrum. According to (1) and (2), each wavelength corresponds to a different scattering wave vector [35]. In general, to increase the Q-range, several incident angles are used for the reflectivity curves. A schematic representation of the time of flight reflectometer is shown in Figure 11.

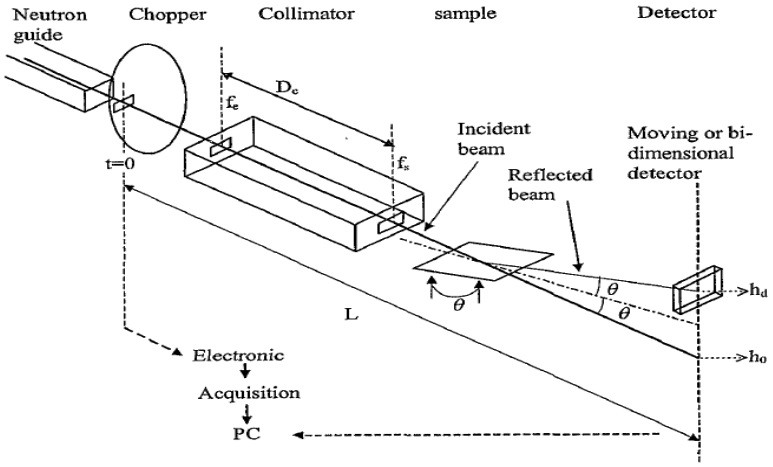

Figure 11. Sketch of the time-of-flight spectrometer [42]

The wavelength of neutrons varies as the inverse of the speed, which is directly related to the time needed to travel from the chopper to the detector (which corresponds to the distance L in Figure 11), and thus it is possible to write

$$\lambda = \frac{h}{mL} t \qquad (3)$$

where m is the mass of neutrons. This formula is slightly inaccurate because the chopper also has some length. The longer the distance from the chopper to the detector, the smaller is the inaccuracy [35].

Two incident angles (0.624 and 3.78 degree) were here used. Applying these two angles permitted the measurement of a reflectivity curve up to 0.3 $Å^{-1}$ in Q_z

considering that the wavelengths of the incoming beam were between 2 Å and 30 Å. The lambda resolution for this measurement was maintained at 4.2% by the collimation system. The divergence of the incident beam was less than 2%. For the data collection, a 2D Helium detector was used. The active area of the detector was 500x250 mm^2, and the resolution was 2x7 mm^2. A more detailed description of the Figaro reflectometer at the ILL can be found elsewhere [42].

For the data treatment, the raw data were converted into Q_x-Q_z maps [43]. At this step, the gravity effect on the neutrons due to horizontal scattering geometry were taken into account [44, 45]. Considering cuts over the Q_x-Q_z maps at constant Q_z, it was possible to separate the specular region and perform a proper background subtraction.

2. 2. 7 Angular Resolution

To properly interpret the neutron data, it is important to know the beam divergence and homogeneity. The divergence of the incident beam is determined by two slits. There are two effects: 1) the amplitude of the oscillations (Ti in our case) is decreased, and 2) the discontinuity at the critical angle is rounded.

In the case of wavelength dispersion, which is strongly dependent on the time resolution in the time-of-flight mode, there is an additional effect – the washing out of oscillations at high angles.

Presenting information on the beam angular divergence and wavelength resolution is important because experiments on samples with a nonhomogeneous thickness yield a very similar effect (see Figure 12). A wavelength resolution can be used to model thickness variations on the sample surface [35].

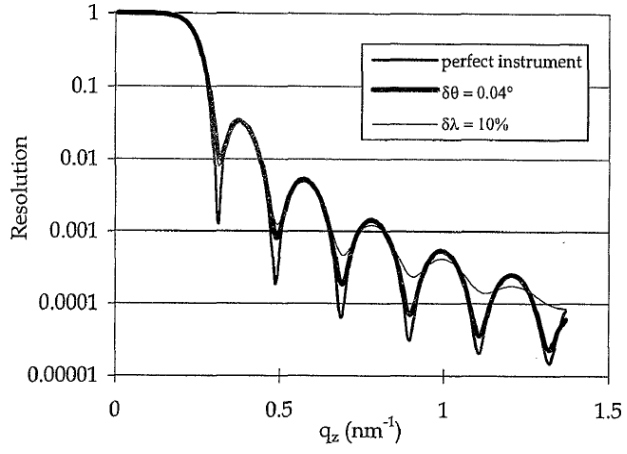

Figure 12. Effect of the angular divergence and wavelength dispersion [35]

2. 3 Theoretical Part

2. 3. 1 X-ray Scattering

The X-ray radiation interacts mainly with the electron shell and only extremely weakly with atomic nuclei (the ratio of the amplitude is the inverse of the masses). The interaction is essentially strong between the electric field of the X-rays and the charge of the electrons and there is only a much weaker interaction manifested between the electromagnetic field and the spin. The X-ray scattering of electrons is also called Thomson scattering.

By assuming that every point of the electron scatters independently and that the scattered amplitudes add coherently, the general optical formalism can be applied to X-ray scattering from a surface and interfaces [46]. The refractive index of matter for X-ray can be written as

$$n = 1 - \delta - i\beta \quad (4)$$

where δ is the dispersion coefficient and β is the abortion coefficient. The classical model of an elastically bound electron yields the following expression for the dispersion coefficient δ:

$$\delta = \frac{\lambda^2}{2\pi} r_e \rho_e \quad (5)$$

Where $r_e = \frac{e^2}{m_e c^2}$ is the classical electron radius, e is the charge of an electron, m_e is the mass of an electron, c is the light velocity, λ is the wavelength and ρ_e is the electron density of the material. The typical range of δ is 10^{-5} – 10^{-6}, and β is ten times smaller [35]. Because the refractive index is less than 1, an incident beam can be totally reflected if the incidence angle θ between the ray and the surface is less than the critical angle θ_c. The critical angle can be calculated from Snell-Descartes' law with $\cos\theta_c = 1$, assuming that there is no absorption:

$$\cos\theta_c = n = 1 - \delta \quad (6)$$

Because the critical angle is small, the previous relationship can be rewritten as

$$\theta_c = \sqrt{2\delta} \quad (7)$$

On each interface, the electromagnetic wave with wave vector k_{in} and an angle of incidence θ_i is split into a reflected and a transmitted wave as shown in Figure 13. According to Fresnel theory, it is possible to write coefficients for reflection and transmission as

$$r = \frac{k_{in,z} - k_{tr,z}}{k_{in,z} + k_{tr,z}} \tag{8}$$

$$t = \frac{2k_{in,z}}{k_{in,z} + k_{tr,z}} \tag{9}$$

where $k_{in,z} = -k_{r,z} = k\sin(\theta_i)$ and $k_{tr,z} = nk\sin(\theta_t)$ [35].

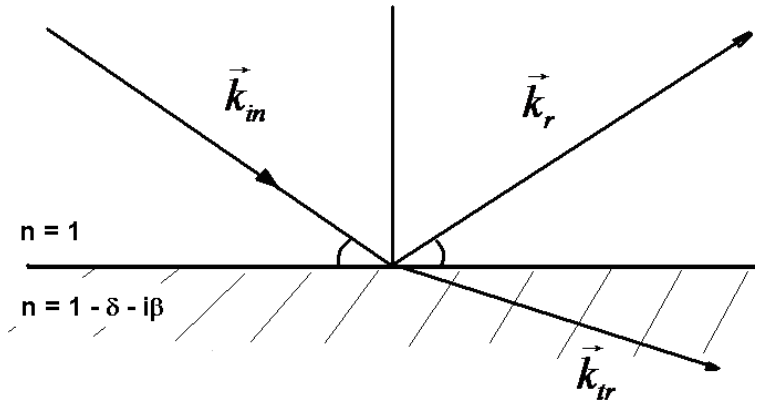

Figure 13. Reflectivity at an air/solid interface

Under the specular reflectivity conditions, the incident angle and the reflected angle are equal, and thus, the wave vector transfer can be written $Q_z = k_{r,z} - k_{in,z} = \frac{4\pi}{\lambda}\sin(\theta_i)$, where λ is the wavelength of the X-rays. In this case, the parallel wave vector transfer is zero, and thus, there is no direct access to the in-plane structure, just about the average structure in the z direction perpendicular to the surface. The reflectivity, which is the square of the modulus of the reflection coefficient, can be written as

$$R(\theta) = \left| \frac{\theta - \sqrt{\theta^2 - \theta_c^2 - 2i\beta}}{\theta + \sqrt{\theta^2 - \theta_c^2 - 2i\beta}} \right|^2 \tag{10}$$

Or in terms of the wave vector transfer Q:

$$R(q_z) = \left| \frac{Q_z - \sqrt{Q_z^2 - Q_z^2 - \frac{32i\pi^2\beta}{\lambda^2}}}{Q_z + \sqrt{Q_z^2 - Q_z^2 - \frac{32i\pi^2\beta}{\lambda^2}}} \right|^2 \tag{11}$$

When the wave vector transfer is large compared to $Q_c = \frac{4\pi}{\lambda}\sin(\theta_c)$ the reflectivity has the following asymptotic behavior:

$$R(Q_z) = \frac{Q_c^4}{16Q_z^4} \tag{12}$$

2. 3. 2 Neutron Scattering

The optical formalism can be applied to neutrons as well as to X-rays. Nevertheless, neutron scattering has other physical origins compared to X-ray radiation. Because neutrons have a neutral electrical charge, they are not disturbed by electron shells. Instead, neutrons interact with the Fermi potential of the atomic nuclei [47]. The reflective index for neutron scattering is similar to that for X-ray (see Formula 4). Usually, the absorption is not taken into account, with the exception of specific materials, such as B, Cd and Gd, which are used as absorbers for neutrons. For neutrons, the dispersion coefficient is dependent on the scattering length b and can be written as $\delta = \frac{\lambda^2}{2\pi}\rho b$, where ρ is its density of the material. It is possible to write analogous formulas for the Fresnel reflectivity coefficient. In general the neutron flux generated by reactors or spallation sources are many magnitudes smaller compared to a typical photon flux provided by synchrotron sources which makes neutron experiments more time-consuming and usually also more limited in the accessible Q range. Nevertheless, neutron scattering is extremely useful for soft matter research because it provides the possibility of contrast variation analysis. The scattering length density of D_2O is larger and the scattering length density of H_2O is lower than that of any biological molecule [48]. This phenomenon enables all biological molecules to be matched by utilizing an appropriate mixture of the two solvents. Figure 14 shows some examples of the average scattering length densities of common biological macromolecules as a function of the concentration of D_2O.

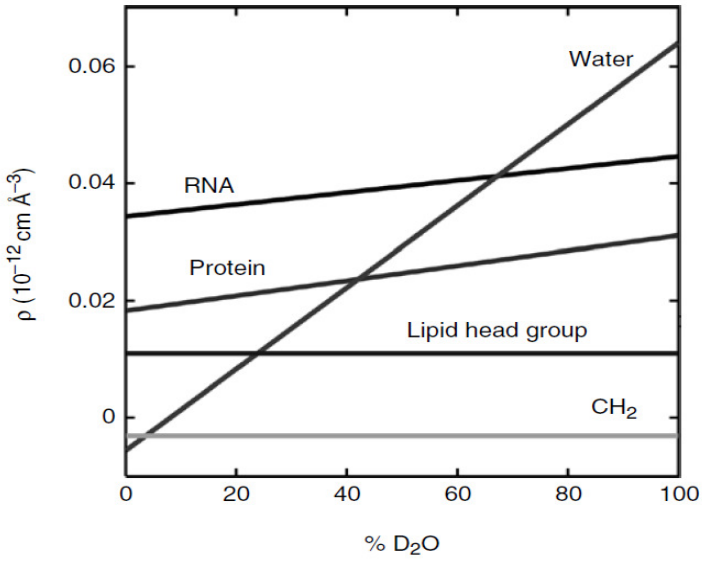

Figure 14. SLD dependence of biological molecules on D_2O concentration [48]

2. 3. 3 Kinematic Approximation

The semi-kinematic theory is derived from the dynamic theory by three approximations [49]:

1) no multiple reflections at the interfaces are taken into account;
2) the effects of refraction can be neglected;
3) Q_z does not change at each interface, and thus, the reflection coefficient is proportional only to the difference in electron density.

The Born approximation cannot be used in the lowest angular regions, where the scattering is dominated by optical effects, but it is very useful for quantitative interpretation [22]. The final equation for reflectivity in the kinematical approach is given by the following [50]:

$$R(Q_z) = rr^* = R_F(Q_z)\left|\frac{1}{\rho_s}\int_{-\infty}^{\infty}\frac{d\rho(z)}{dz}\exp[iQ_z z]dz\right|^2 \quad (13)$$

For a periodic multilayer structure, which is ideally flat with parallel layers of uniform density and thickness, the reflectivity in the Born approximation can be written as [51]

$$R_{multilayer}(Q_z) = \frac{4\pi}{iQ_z}\frac{Sin(MQ_zD/2)}{Sin(Q_zD/2)}\exp[i(M-1)DQ_z]\int_0^D \rho_{film}(z)\exp[iQ_z z]dz \quad (14)$$

Where M is a number of a unit film (e.g., the bilayer) of thickness D in a multilayer structure. The integral over $\rho_{film}(z)$ is limited to the size of the unit film, and $R_{multilayer}$ peaks strongly at $Q_z = \frac{2\pi m}{D}$, where m=1, 2, 3…, in the manner of Bragg peaks in crystallography [52].

2. 3. 4 Fourier Analysis of Multilamellar Samples

This type of analysis offers the possibility of building a one-dimensional SLD profile of a lipid bilayer using a discrete set of Fourier coefficients f_n [53] and only requires integrated Bragg peaks. The exact relation between the Bragg peak intensity and the Fourier coefficient is an open question [54]. A widely used correction factor is $I_n = \frac{|f_n|^2}{Q_z}$, where Q_z^{-1} is a Lorentz factor for oriented bilayers. Such a

correction gives the most appropriate results compare to another empirical corrections [20]. The SLD profile can be calculated according to

$$\rho_{bilayer}(z) = \frac{2}{D}\sum_{n=1}^{M}\sqrt{\frac{2n\pi}{d_z}}\sqrt{I_n}v_v\cos(\frac{2n\pi}{D}z) \qquad (15)$$

Where $z \in \left[-\frac{D}{2};\frac{D}{2}\right]$, I_n is the integrated intensity of the nth Bragg peak, v_n is the corresponding phase of f_n and D is the periodicity of the bilayers in the z direction. An example of such a profile is given in Figure 15.

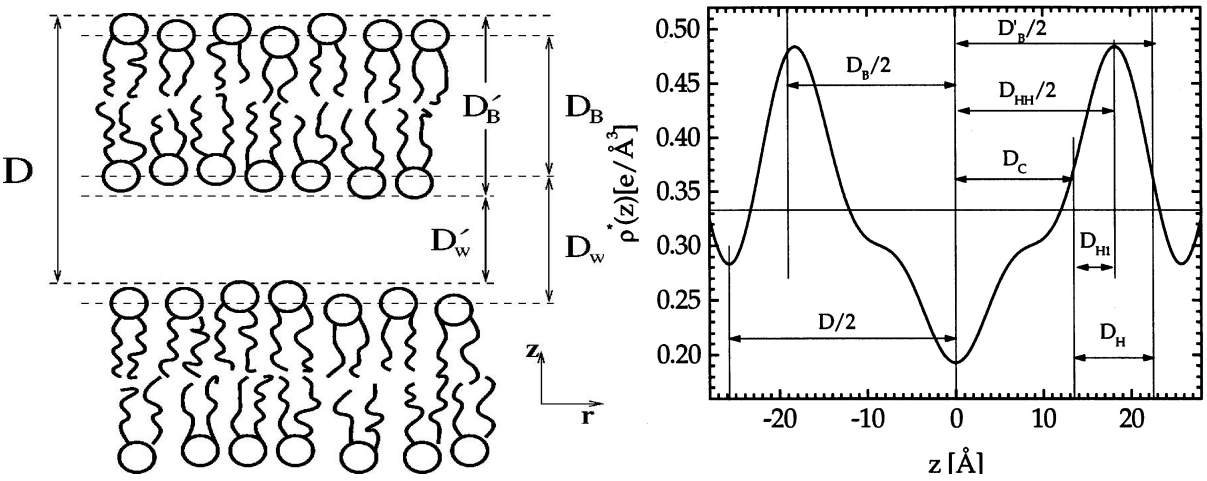

Figure 15. Lipid bilayer spacing and corresponding SLD profile [55] [56]

2. 3. 5 The Effect of Roughness on the Specular Reflectivity

All physical interfaces exhibit some type of roughness or interdiffusion on an atomic scale. Different types of roughness can be distinguished by their origin and roughness scales:

1) Interdiffusion of the species between two successive layers. This happens mostly when a top layer mixes with the bottom material during the deposition process. For this type of system, the lateral length scale of the roughness is usually $\xi < 0.5$ μm. ξ is defined as the maximal distance between two different irregularities at which the heights are still correlated [35].

2) Roughness induced by initial roughness of the substrate or by grains in the case of two successive layers. This type of roughness corresponds to thin film growth, for example, the formation of an oxide layer (1 μm < ξ < 100 μm).

3) Flatness of the sample, which depends on the deposition process (ξ>100 μm).

These three roughness scales can be modeled and induce very different effects on the experimental reflectivity curves.

Because specular reflectivity gives only information about the average SLD over large lateral areas of the sample, it cannot be used to analyze the lateral structure in detail. However, the reflectivity signal on interdiffused or rough interfacial structures drop off faster compared to an ideally sharp interfaces. In the case of a rough interface, the loss of intensity in the specular path is re-distributed into the off-specular diffuse region of the scattering [57].

Let us consider that a function z(x, y) is the precise description of the surface roughness. Usually, a full definition is not necessary for describing a system; the information about certain statistical properties of a surface, including the height-height correlation, will be here sufficient.

In a first approximation, a random function could be applied to describe the rough surface. In that case, the height probability distribution could be approximated as a Gaussian [35]

$$p(z) = \frac{1}{\sigma\sqrt{2\pi}} \exp[-\frac{z^2}{2\sigma^2}] \tag{16}$$

where σ is the root-mean-square (rms) roughness.

Here, the Fresnel coefficient is reduced by a term in the form of the Debye-Waller factor:

$$\frac{r_{j,j+1}^{rough}}{r_{j,j+1}^{flat}} = \exp[-\frac{Q_z^2 \sigma_{j+1}^2}{2}] \tag{17}$$

This is a widely used method for programs based on the Parratt optical formalism to describe rough interfaces.

For a non-Gaussian roughness, which is defined by the condition $\frac{\sigma}{D} > 0.3$, the electron density or the scattering length density profile (SLD) of the neutrons may be approximated by cutting the interface into thin slabs of varying electron density [57].

2. 3. 6 Diffuse Scattering in the Born Approximation

The specular scattering provides information only about the average SLD profile along the z direction. To obtain insight into the lateral structure, we need to analyze the scattered intensity in the off-specular direction. The differential cross section for scattering of X-rays or neutrons by a sample system is given by the Born approximation:

$$\frac{d\sigma}{d\Omega}=\left(\frac{Nb}{Q_z}\right)^2 L_x L_y \iint_{L_x L_y} dxdy \exp\left[-\frac{Q_z^2 g(x,y)}{2}\right]\exp\left[-i(Q_x x+Q_y y)\right]=(Nb)^2 L_x L_y S(\vec{Q}) \quad (16)$$

Where L_x L_y is an area of the reference surface, N is the number density of the scattering particles, b is the coherent scattering length, and g(x, y) is the correlation function, which is defined as $g(x,y)=\left\langle\left(z(x,y)-z(0,0)\right)^2\right\rangle$. It is possible to denote the in-plane vector r, which has coordinates x and y, by g(x, y) = g(r). $S(\vec{q})$ is the scattering function defined according to [58] as

$$S(\vec{q})=\frac{\exp[-Q_z{}^2\sigma^2]}{Q_z{}^2}\int \exp[Q_z{}^2 C(r)]\exp[-i\vec{Q}\vec{r}]d^2r \quad (19)$$

where σ is the root mean square deviation of the surface (rms roughness), C(r) is the height-height correlation function of the surface on the lateral structure of the sample. The height-height correlation function can be written in general in terms of the correlation function as $C(r)=\left\langle\left(z(r)z(0)\right)\right\rangle=\sigma^2-\frac{1}{2}g(r)$.

The scattering function can be now separated into a specular part and a diffuse part:

$$S(\vec{Q})=S_{spec}(\vec{Q})+S_{diff}(\vec{Q}) \quad (17)$$

with the specular and diffuse contributions written as

$$S_{spec}(\vec{Q})=\frac{\exp[-Q_z^2\sigma^2]}{Q_z^2}\int_A \exp[-i\vec{Q}\vec{r}]d^2r \quad (18)$$

$$S_{diff}(\vec{Q})=\frac{\exp[-Q_z^2\sigma^2]}{Q_z^2}\int_A (\exp[-iQ_z^2 C(\vec{r})]-1)\exp[-i\vec{Q}\vec{r}]d^2r \quad (19)$$

The statistical description of surface morphologies with a height-height correlation function permits the use of some distinct parameters, such as rms roughness σ, the correlation length ξ and the Hurst parameter h. The Hurst parameter characterizes the jaggedness of the interface (h=1 corresponds to a smooth interface, and the jaggedness increases with decreasing h). The parameter h is also related to the fractal dimensionality D of self-affinity surfaces via D=3-h [58]. For a single rough interface with a cut-off, the height-height correlation function can be represented as [58]

$$c(r)=\sigma^2\exp\left[-\left(\frac{r}{\xi}\right)^{2h}\right] \quad (20)$$

When Q_z is a constant, the scattering function solely depends on the form of C(r), for example, when h=0.5, the scattering function has a Lorentzian shape, whereas for h=1, the shape of $S(\vec{Q})$ is Gaussian. Some examples of surfaces calculated according to equation 23 are presented in Figure 16.

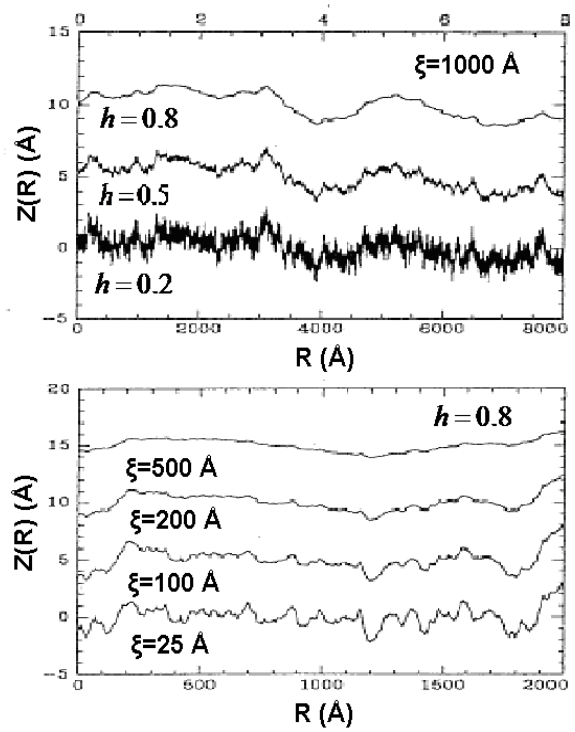

Figure 16. One-dimensional surface structures calculated for different values of the Hurst parameter and the correlation length [59]

2. 3. 7 Capillary Waves

The capillary wave theory is a widely used model for describing lateral structures, such as a polymer film or a monolayer of lipids deposited by the LB technique [60, 61]. Due to fluctuation processes, the surface of liquids is not completely flat. Fluid dynamics are dominated by the effects of surface tension, leading to the appearance of waves that travel along the phase boundary of fluids. The height-height correlation function in this case can be written for a large r as

$$C(r) \approx \frac{k_b T}{2\pi\gamma}\left[\gamma_E + \ln\left(\frac{\sqrt{\frac{g\rho_m}{\gamma}}r}{2}\right)\right] \qquad (21)$$

Here, γ_E is the Euler constant, which is equal 0.577, ρ_m is the density and γ is the surface tension. Using the last formula, the scattering function is written as:

$$S(\vec{Q}) = \frac{2\pi \exp[-Q_z^2 \sigma_{eff}^2]}{Q_z^2 \Delta Q^2} \Gamma(1-\frac{\eta}{2}) F_1(1-\frac{\eta}{2}, 1, \frac{-Q^2}{2\Delta Q^2}) \quad (22)$$

With $\eta = \frac{Q_z^2 B}{2}$, $B = \frac{k_b T}{\pi\gamma}$ and $\sigma_{eff}^2 = \sigma^2 + \frac{1}{2} B\gamma_E - \frac{1}{2} B \ln(\frac{\sqrt{2}\Delta Q}{\sqrt{\frac{g\rho_m}{\gamma}}})$

Here ΔQ denotes the Q resolution, and σ_{eff} describes an effective roughness, which includes an experimental resolution. $\Gamma(x)$ is the Gamma function, and $F_1(i, k, x)$ is the Kummer function.

It is possible to show that within the framework of this theory, at constant Q_z and far from the specular peak, the diffuse scattering function has a characteristic power law, which can be written as

$$S_{diff}(Q_x) \sim Q_x^{\frac{k_B T}{2\pi\gamma} Q_z^2 - 2} \quad \text{for small L} \quad (23)$$

$$S_{diff}(Q_x) \sim Q_x^{\frac{k_B T}{2\pi\gamma} Q_z^2 - 1} \quad \text{for large L [62]} \quad (24)$$

Because a separation into a specular and a diffuse component is not performed for the capillary waves model, the Kummer function is needed to provide a smooth transition between the Gaussian-like specular scattering and the power law tails of the diffuse scattering.

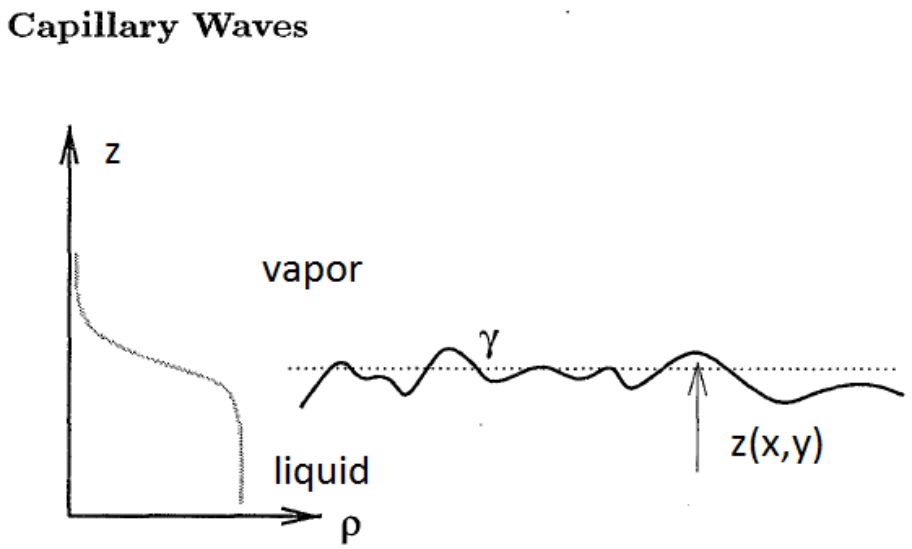

Figure 17. Schematic illustration of the vapor/liquid interface in terms of the capillary wave theory, where γ is the surface tension, and z (x, y) is the interface height. The corresponding average density profile is given on the left [35].

2. 3. 8 Distorted Wave Born Approximation

The Born approximation is not valid near the critical angle for total external reflection since it does not take into account any dynamical effects as multiple scattering. To go beyond this approximation and to take the optical properties of the waves into account, the distorted-wave Born approximation (DWBA) needs to be applied. Following the classical work of Sinha, it is possible to define the scattering wave vector $\vec{k}_1$ with the corresponded incident angle θ_1 and the time reverse scattering wave vector $-\vec{k}_2$ - θ_2, (see Figure 18).

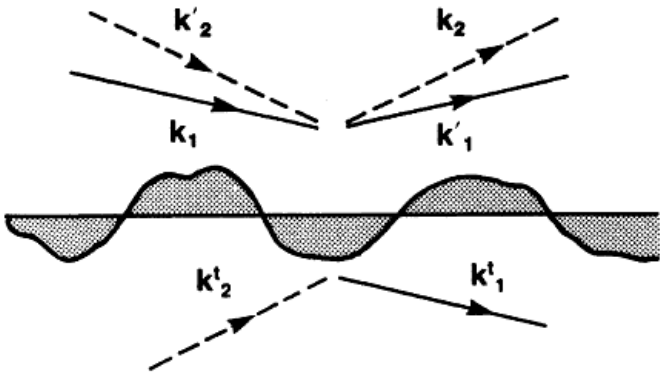

Figure 18. Rough surface. The horizontal line is the average surface (z=0). The regions of perturbations are presented by the shaded regions. $\vec{k}_1$ and $-\vec{k}_2$ are the incident scattering wave vectors, $\vec{k}_1'$ and $-\vec{k}_2'$ the reflected scattering wave vectors. $\vec{k}_1^t$ and $-\vec{k}_2^t$ the transmitted scattering wave vectors [58].

The exact solution of the wave equation for a rough surface is defined using perturbation theory. In this instance, the differential cross section can be written as [58]

$$\frac{d\sigma}{d\Omega_{DWBA}} = L_x L_y \frac{(Nb)^2}{{Q_z}^2} \left|T(k_i)\right|^2 \left|T(k_f)\right|^2 S(\vec{Q}_t) \qquad (25)$$

Where $\vec{Q}_t = \vec{k}_2^t - \vec{k}_1^t$ is the wave vector transfer in the medium. $\left|T(k_i)\right|$ and $\left|T(k_f)\right|$ are the Fresnel transmission coefficients. As defined in [63], for a large Q_z, the transitivity coefficients are equal to 1, and equation 28 reduces to the Born approximation. Whenever θ_1 or θ_2 is equal to the critical angle, the diffuse scattering will have peaks known as Yoneda scattering.

More generally, for the case of a multilayer system, the scattering function should be defined by taking into account the correlation between the roughnesses at

different interfaces i and j. This can be done by applying an additional cross-cross correlation function:

$$C_{i,j}(r) = \left\langle \left(z_i(0) z_j(r) \right) \right\rangle \quad (29)$$

For $C_{i,j}(r) > 0$, it corresponds to the case of conformal roughness, and a characteristic distribution of the diffuse scattering is expected in the reciprocal space. The analysis could be simplified, compared to the general situation, in the case of multilayer systems with highly correlated interfaces. From the experimental point of view, conformal roughness can be recognized in scans parallel to the specular ridge: in the case of conformal roughness, the diffuse intensity will form ridges of scattering extending perpendicular to the specular scattering (so-called Bragg sheets); in the case of a roughness without any interfacial cross-cross correlation, diffuse scattering will not be particularly ordered along the direction parallel to the specular ridge [57].

3 Results

3. 1 Surface Pre-characterization

Here, and in the following chapters, the optical matrix method is used to analyze the reflectivity data. Layers are modeled by boxes of a specific thickness and SLD. A single Gaussian roughness is used to smear the interface, and the final input is compared to the measured data [64]. In this work, two programs (Parrat32 and Motofit) are applied to model the extracted reflectivity curves [65]. By considering the least squares fitting, it was possible to generate model reflectivity curves that reproduce the experimentally measured curves.

There are two types of metal surfaces prepared by the magnetron deposition chamber. The silicon wafers (1 mm thick) were covered with Ti or with a Ti6Al7Nb alloy (87% Ti, 6% Al and 7% Nb). Those samples were used in a set of X-ray experiments. For neutron experiments, to obtain a pure titanium covering, we used Si crystals with a dimensions of 8x5x1 cm^3 to obtain a pure titanium covering.

In general, to construct a proper SLD profile for such samples, a model has to take into account the following layers:

1) silicon wafer (crystal);
2) layer of silicon dioxide;
3) titanium (titanium alloy) layer;
4) layer of titanium dioxide.

3. 1. 1 Titanium Coated Si-Wafer (630 Å)

The X-ray specular reflectivity curve for the first Si-wafer coated with pure titanium is shown in Figure 19. According to the simulations, the assumption of a layer of silicon dioxide did not improve the fit. The best fitting result was achieved with a thickness of the titanium layer of 636 Å and a roughness of 10 Å (for more details, see Table 2).

The reflectivity curve includes the point at which the oscillations of the metal layer disappear and break the oscillations into two parts. That point is recognized as the so-called “beating point”, which is determined by the titanium dioxide layer. The position of the “beating point” corresponds to the thickness of the titanium dioxide

layer as $Thickness_{TiO_2} = \frac{4\pi}{q_{beating\_point}}$ [35]. Refining the parameters by the best fit, the thickness and roughness of the titanium dioxide layer could be determined to be 36.9 Å and approximately 10 Å, respectively.

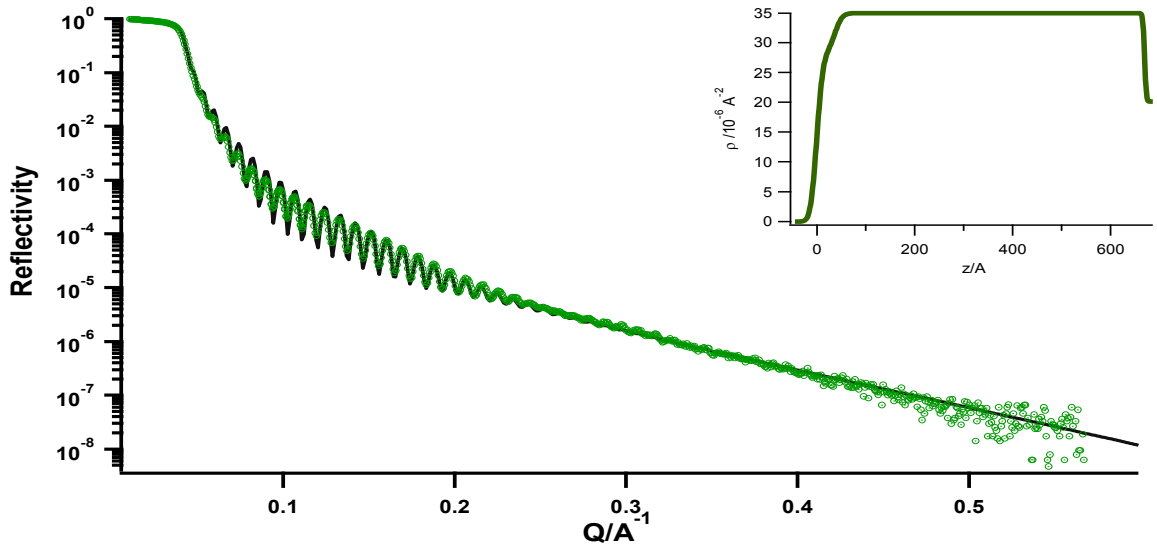

Figure 19. X-ray reflectivity curve (green curve) of the uncoated Ti coated Si-wafer together with the theoretical curve (black curve) and calculated SLD profile, for which the start of the scale corresponds to the border air/TiO_2.

3. 1. 2 Titanium Alloy Coated Si-Wafer (1390 Å)

For the Si-wafer covered with the alloy, the layers of TiO_2 and SiO_2 wafers were used to fit maximums at 0.15 $Å^{-1}$ and 0.33 $Å^{-1}$, respectively (see Figure 20). In this case, the "beating point" was hardly visible. The key parameter for the "beating point" effect is the roughness of the Ti6Al7Nb layer because it affects the oscillation at high Q_z. According to the simulations, the "beating point" for such a thick Ti alloy layer can be observed only when the roughness of the Ti alloy layer is less than 4 Å. However, the analysis indicates that the roughness of the Ti alloy layer was 10 Å and thus oscillations were not visible on the reflectivity curve for Q_z higher than 2.2 Å. The final model is described in more detail in Table 2.

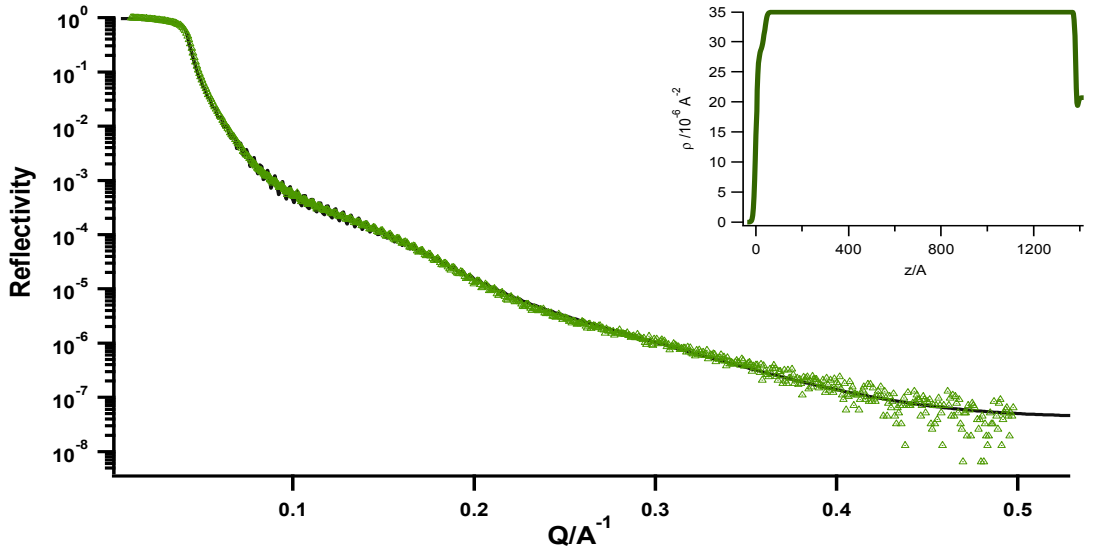

Figure 20. X-ray reflectivity curve of the Si-wafer coated with alloy (green triangles) and the theoretical curve

Table 2. Titanium coated Si-wafers, X-ray SLD profiles

Sample	Material	Thickness, Å	SLD, 10^{-6}Å^{-2}	Roughness, Å
Titanium coated Si-wafer	Air	None	0	None
	TiO_2	37±1	30±4	10±3
	Ti	636±5	36±2	10±3
	SiO_2	None		
	Si	None	20±1	3±1
Si-wafer coated with Ti6Al7Nb alloy	Air	None	0	None
	TiO_2	39±1	28±4	8.5±3
	Ti6Al7Nb	1390±6	36±1	10±3
	SiO_2	8±2	19±1	4±1
	Si	None	20±1	3±1

3. 1. 3 Titanium coated Si-crystals (1000 Å and 400 Å)

To perform the neutron experiments at solid/liquid interphase e.g. at the beamline Figaro, a few Si-crystal substrates were used as a substrate. In order to get information about the surface roughness of the initial Si crystals were characterized by X-ray reflectometry before the deposition of a titanium layer. The measurement of the Si crystals (see Figure 21) enabled the calculation of the roughness of the silicon surface (8 Å), which was maintained as a constant in our subsequent analysis. Additionally, X-ray reflectivity experiments showed that all Si-crystal substrates used in this investigation were identical.

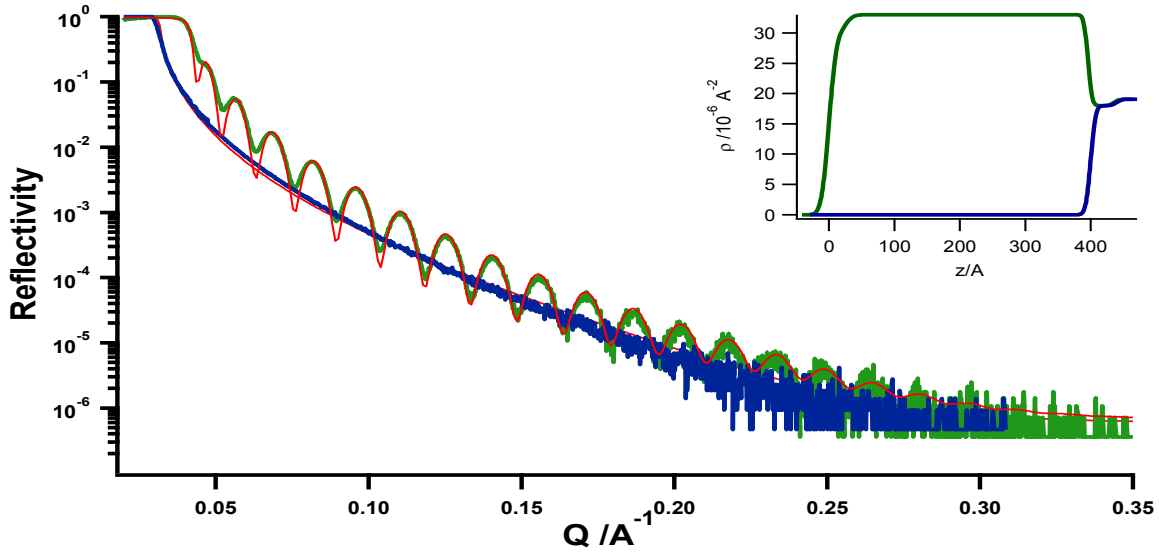

Figure 21. X-ray reflectivity curves and SLD profiles: 1) the blue curve corresponds to the Si crystal, and the green curve corresponds to the Si crystal coated with titanium. The fits are indicated by red curves. 2) Calculated SLD profiles are given in the upper right corner

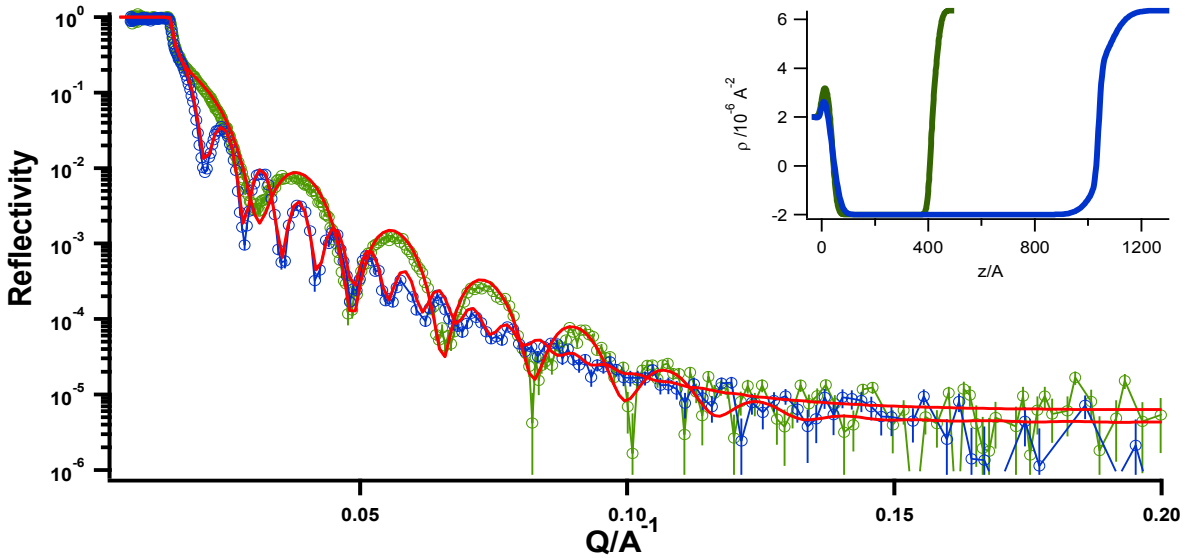

Figure 22. Neutron reflectivity curves of the Si crystals coated with titanium: 1) blue rings correspond to 1000 Å thick titanium coating; 2) green rings – 400 Å. The theoretical curves (red curve).

Three Si crystals were coated in a similar way with the 400 Å thick Ti layer by the sputter deposition technique (see Chapter 2. 1. 1). The fit shows the following parameters for the titanium layer: a thickness of 39.5 Å and a roughness of 8.5 Å. In this case, adding a titanium dioxide layer was not improving the fits significantly. It should be mentioned, however, that X-ray reflectometry cannot always deliver the proper parameters of an oxide layer due to the similarity of SLDs for titanium and titanium dioxide in the X-ray regime.

The Ti-coated Si-crystals were remeasured one more time with neutrons before the further coating with POPE lipids. The measurements of the neutron

specular curves demonstrated that the coating was completely reproducible for each of the three Ti coated Si-crystals. The fitting of the data allowed one to gain even more precisely information on the surface quality in comparison with the X-ray data, since SLD contrasts between silicon and silicon dioxide and between titanium and titanium dioxide are more pronounce for neutrons. Additional layers of silicon dioxide and titanium dioxide were applied to fit the neutron data. In that experiment, a model with a Ti layer (365 Å) and a TiO_2 layer (25.42 Å) with a roughness of 12 Å for both layers (see Figure 22) was used. This model was then successfully applied to the previous X-ray data.

In addition to these three Ti coated Si-crystals, a crystal with a thicker titanium layer was prepared. This additional substrate was characterized by neutron reflectivity measurements against D_2O (see Figure 22). The model used for the fitting was the same as that for the first type of Ti coated Si-crystal. The final fitting parameters can be found in Table 3. The use of these two types of Ti coated Si-crystals allowed us to avoid the phase problem of a reflectivity experiment and keep the same surface chemistry.

Table 3. Si crystals coated with titanium, neutron SLD profiles

Sample	Material	Thickness, Å	SLD, 10^{-6} Å^{-2}	Roughness, Å
Titanium coating – 400 Å	Si	None	2±0.3	None
	SiO_2	40±5	3.4±0.3	8±3
	Ti	368±4	-1.96±0.2	12±4
	TiO_2	24±3	2.4±0.3	12±4
	Intermediate layer	None	6.36±0.2	15±8
	D_2O	None	6.36±0.2	0
Titanium coating – 1000 Å	Si	None	2±0.3	None
	SiO_2	40±5	3.4±0.3	8±3
	Ti	1000±4	-1.96±0.2	25±4
	TiO_2	20±2	2.4±0.3	10±4
	Intermediate layer	None	6.36±0.2	30±10
	D_2O	None	6.36±0.2	0

3. 2 Drop Coating

For implant modification, a stable and complete POPE coating of implant surfaces in a liquid environment is extremely important. Phospholipids can stay on a solid surface in contact with water only as a multilayer structure. With respect to implant modification, the following questions must be addressed: 1) what is the optimal method for lipid deposition on a titanium surface so that the multilayer stack will be evenly distributed on top of the titanium implant; 2) how stable is the coating; and 3) what is the lateral structure and the structure in the z direction of this multilayer system.

Therefore a POPE multilayer stack deposited on titanium-based surfaces was examined by the X-ray diffractometer described in Section 2. 2. 3. Because the setup of the RoeDi diffractometer does not permit measurements at the solid-liquid interface, the investigation of the water effect was conducted in the following manner: the sample was first exposed to water for some time, followed by measurement by the diffractometer against air.

The easiest way to prepare a lipid multilayer stack on a solid surface is to dissolve the lipids in an organic solution and drop this solution onto the surface. After solvent evaporation, the lipids should be self-organized in a multilayer structure due to the hydrophobic force. This sample preparation method is widely applied in the literature and would be the most feasible if real implants with a complex geometry are considered.

3. 2. 1 Silicon Surface

The experiment in which a silicon wafer was used as substrate to be coated is a classical experiment performed in a number of works to investigate lipids multilayer structure [66]. Because methanol and chloroform are adhesive liquids for a silicon surface, the POPE lipids were homogeneously distributed on the top of the silicon wafer.

The lipid coating on the silicon wafer results in the presence of strong Bragg peaks in the reflectivity curve (see Figure 23), which was measured the day after one hour of exposure of the sample to water.

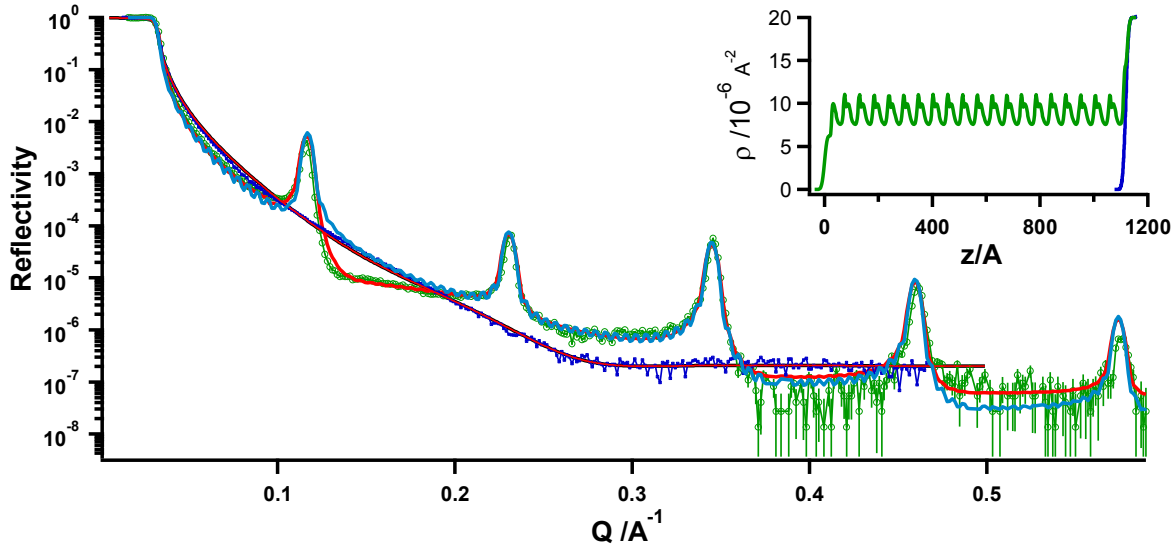

Figure 23. X-ray reflectivity and SLD profiles of the POPE drop-coated silicon wafer: 1) the blue curve corresponds to the silicon wafer; 2) the green curve corresponds to the POPE drop-coated silicon wafer; 3) the red curves correspond to the model reflectivity curves obtained from the fit. The corresponding SLD profiles are presented in the upper right corner; 4) the cyan curve corresponds to the model curve, in which the intermediate layer is not taken into account.

These data were first analyzed via Fourier analysis (see Chapter 2. 3. 4). Bragg peaks (five orders) are separated from the specular reflectivity curve and then fitted by a Gaussian function (an example of such a fit is given in Figure 24). The such determined values for the integrated intensities of the peaks are used to calculate the one-dimensional scattering length density profile. It is not possible to precisely define the phase factors in equation 33 from the X-ray data because the phase factors can be found only by applying a contrast variation analysis. Thus, all possible combinations of phase factors have been considered, and the final profile presented in Figure 25 was selected as the most reasonable.

To estimate the average number of bilayers, the “Debye-Scherrer method” is applied. The full width of the Bragg peak at half maximum (FWHM) is related to the number of bilayers N within the sample [67]**:**

$$FWHM = \frac{K * 2\pi}{d * N},$$

where K=0.88 is a shape factor for crystalline systems and d is a repeat distance[68].

After calculating the FWHM and taking into account the resolution of the measurement, the number of coherent scattering domains was determined to be approximately equal to 25-35. The precise number of bilayers cannot be truly defined because the upper bilayers coat the surface only partially. Thus, there are no Kiessig

fringes visible on the reflectivity curve due to interference between the external interfaces of the system [50].

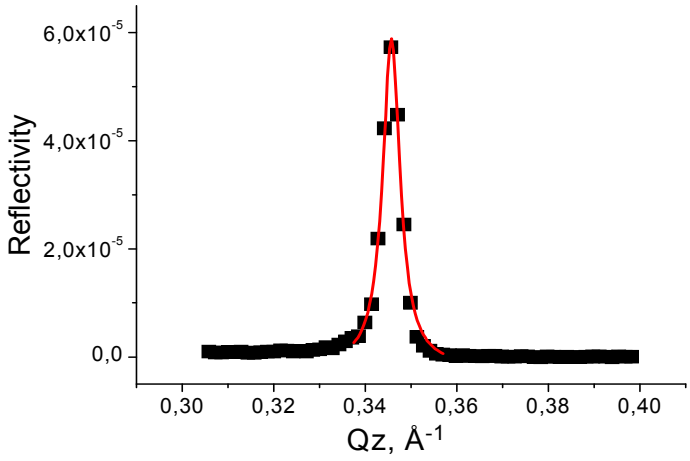

Figure 24. FWHM analysis of the third Bragg peak

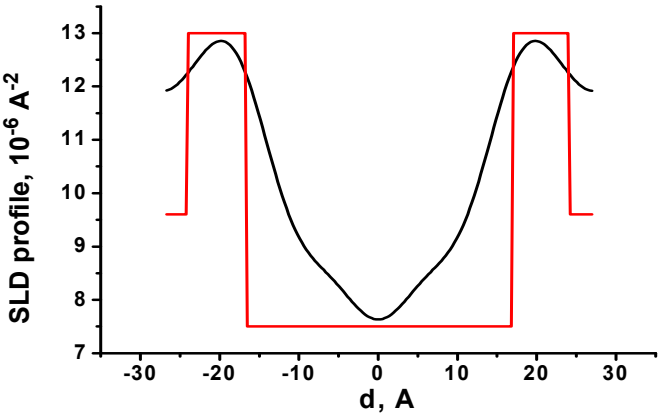

Figure 25. SLD profiles of the POPE bilayer: 1) the black curve is the SLD profile calculated by Fourier analysis of the Bragg peaks; 2) the red curve is the SLD box profile obtained from the fit (roughnesses are not included).

The subsequent simulations of the specular reflectivity curve are performed based on the determined range of the average number of bilayers. Thus, the starting model for the analysis of the reflectivity curve included 30 bilayers on the top of the silicon wafer.

The SLD profile of the POPE bilayer was modeled by 5 box layers, which take into account the intermediate water layer, the head group regions of POPE and the tail group regions of POPE. According to the simulations, the intermediate water layer between the bilayers was 12 Å thick with a roughness of 2 Å, the thickness of the head group region was 6 Å with a roughness of 5 Å and the thickness of the hydrophobic part of the POPE membrane was approximately 37 Å with a roughness of 10 Å (for more details, see Table 4). The SLD values of the POPE head and tail

groups were obtained from the simulations by considering the least squares fitting. The SLD values determined in this manner are reasonable when compared to the known SLD values for other lipids, such as DPPC.

The 30 bilayer model, however, can fit only the shapes of the Bragg peaks and not the general shape of the reflectivity curve (see the cyan reflectivity curve in Figure 23). According to the simulations, the model reflectivity curve is sensitive to a intermediate layer, which is placed on the top of the multilayer structure. The thickness of the intermediate layer was approximately 25 Å with a roughness of 8 Å. The SLD of this layer was slightly less than the SLD of the tail group. Thus, this layer can be interpreted as an incomplete monolayer of POPE on top of the multilayer structure, which actually makes the surface extremely hydrophobic, as observed after exposure to water. The final fit is presented in Figure 23.

Table 4. X-ray SLD profile of the drop-coated silicon wafer.

Sample	Material	Thickness, Å	SLD, 10^{-6} Å^{-2}	Roughness, Å
Si+POPE	Air	None	0	None
	Intermediate layer	25±1	6.5±0.5	8±2
	Lipid multilayer structure 30 repetitions			
	Water layer	3±1	9.6±0.5	2±1
	Head group	6±2	13±1	5±2
	Tail group	36.7±3	7.5±0.8	10±4
	Head group	6±2	13±1	5±2
	Water layer	3±1	9.6±0.5	2±1
	Substrate			
	Silicon	None	20±1	8±2

It is possible to summarize that drop-deposition of POPE lipids on the silicon surface yields a classical phospholipid multilayer system with approximately 30 well-defined bilayers that remain on the surface after one hour of exposure to water.

3. 2. 2 Titanium and Ti6Al7Nb Surfaces

At the next stage of this investigation, the drop-coating method was used to prepare a POPE multilayer stack on the titanium surface. As a result, POPE lipids were extremely unevenly distributed over the surface because titanium does not attract methanol or chloroform, the preferable solvents for POPE lipids. As a

consequence, the solution deposited on the sample surface tries to occupy as little area as possible. This leads to an extremely high concentration of lipids on some zones of the sample surface, while most of the surface does not appear to be coated with POPE lipids (see Figure 26).

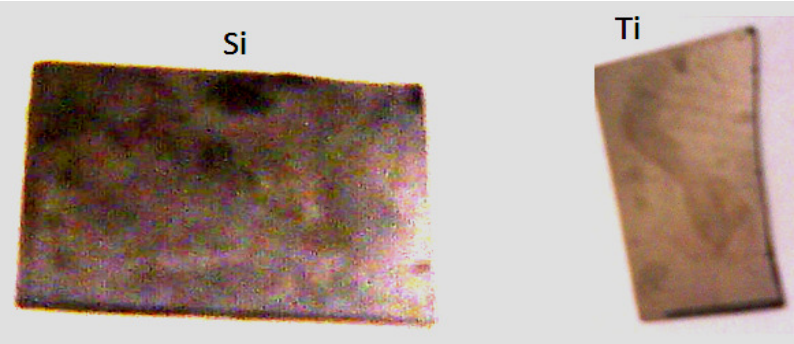

Figure 26. Comparison of Si and Ti drop-coated wafers. The photo shows that POPE lipids are mostly concentrated in the middle of the Ti coated Si-wafer, while for the Si-wafer POPE lipids are eventually separated.

The result of the X-ray experiment with the titanium surface is opposite to that of the silicon surface. The specular reflectivity curve measured from such a drop-coated sample show no Bragg peaks and thus no indication of a ordered multilayer structure. The reason for the missing Bragg peaks is the fact that hydration is needed for the ordering of the lipid. The off-set scan on the other hand displayed a peak at the position in 2Theta=1.656° (see Figure 27), which indicates the presence of a Bragg sheet. Because the Bragg sheet occurs, it is possible to conclude the following:

1) There is some POPE multilayer structure on the top.
2) The layers should be quite rough and laterally correlated.

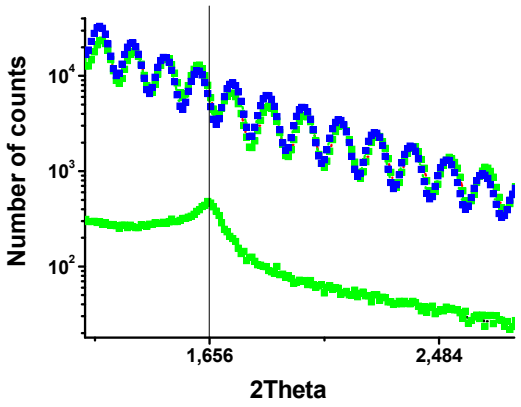

Figure 27. Non-normalized X-ray data: 1) the blue dots correspond to the specular reflectivity curve, which was measured from the Ti coated Si-wafer; 2) the green dots correspond to the specular curve and the off-specular curve, which were obtained from the Ti coated Si-wafer with POPE (drop coating).

The position of the Bragg sheet corresponds to the repeat distance of a multilayer structure 54.7 Å

The POPE drop-coated titanium substrate was then exposed to water for two hours and measured again one day after its exposure. In principle, there are two possible scenarios: 1) a negative scenario in which the POPE lipids are washed away by the water; and 2) a positive scenario in which the POPE remains attached to the titanium surface and starts to form ordered lipid bilayers. The X-ray reflectivity experiment clearly demonstrates that the second scenario occurs because there is a weak Bragg peak present on the reflectivity curve (see Figure 28). Moreover, this peak indicates that the POPE bilayer in the multilayer structure is less rough after exposure to water. Here, the first very interesting feature of POPE lipids is observed – the POPE coating of a titanium surface is extremely stable in water. A reason for this can be that in contrast to other lipids such as DPPC, POPE lipids do not spontaneously form vesicles upon exposure to water and thus, the coated surface preserves its homogeneous properties.

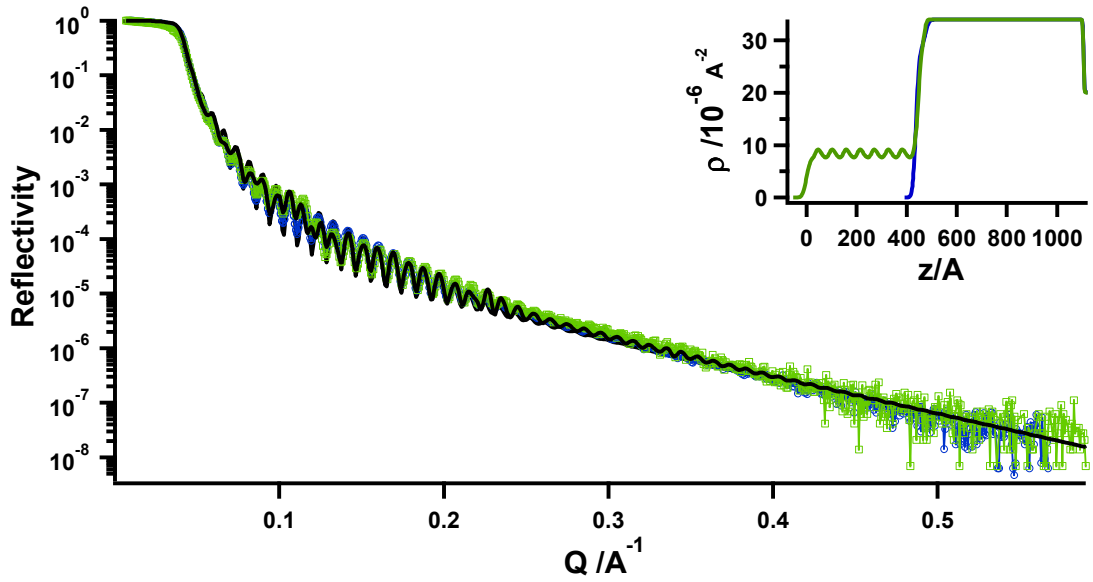

Figure 28. X-ray reflectivity and SLD profiles of the Ti+POPEdrop coated Si-wafer: 1) the blue curve corresponds to the Ti coated Si-wafer; 2) the green curve corresponds to the Ti+POPE drop coated Si-wafer; 3) the black curve corresponds to the model reflectivity curves obtained from the fit. The corresponding SLD profiles are presented in the upper right corner.

Because the signal from the multilayer structure is weak, i.e., only one broad Bragg peak is observed at Q_z=0.11 Å^{-1}, a SLD profile of the bilayer cannot be obtained in detail. Therefore, to fit the data, the simplest model is applied containing a multilayer system of two layers, is applied. The first layer corresponds to the POPE tail's group, and the second layer combines the POPE head group regions with a

very thin water layer in between. Finally, the curve is fitted by modeling 8 bilayers on the top of the Ti coated Si-wafer. According to the simulations, the first layer is 37 Å thick and 12 Å rough; the thickness of the second layer is 19 Å, and the roughness is 8 Å. The parameters for the titanium layer and the titanium dioxide layer are obtained from the fit of the Ti coated Si-wafer and kept constant (for more details, see Table 5).

However, drying POPE lipids from a chloroform-methanol solution onto a titanium surface is not a rational way to prepare this multilayer structure, since,the majority of the lipids are concentrated on small areas of the sample. The specular reflectivity takes into account only the average SLD over the surface, and thus, the signal of the multilayer structure is hardly visible on the reflectivity curve. Therefore it can be assumed that the number of bilayers in the multilayer structure will increase if POPE lipids are uniformly deposited on the titanium surface that is the goal of the next step..

Table 5. X-ray SLD profile of the Ti+drop coated Si-wafer.

Sample	Material	Thickness, Å	SLD, 10^{-6} Å^{-2}	Roughness, Å
Ti coated Si-wafer + POPE	Air	None	0	None
	Head group+H_2O	19±3	10±1	8±2
	Tail group	37±3	7.5±1	12±4
	Lipid multilayer structure 8 repetitions			
	TiO_2	37±1	30±4	10±3
	Ti	636±5	36±2	10±3
	Si	None	20±1	3±2

The first option for obtaining titanium surface coatings similar to those on silicon is to use another organic solvent that would be more adhesive to titanium. For this purpose, isopropanol was applied, but the POPE lipids were poorly soluble in this solvent, and no signal from a multilayer was detected, even in off-set measurements.

The second option was to change the properties of the titanium surface prior to the drop-coating. The use of the Ti6Al7Nb alloy yielded a well-organized, multilayer structure similar to that obtained with the pure silicon wafer. The reflectivity curve which was measured the day after the exposure of this sample to water for two hours is presented in Figure 29. The analysis of the Ti6Al7Nb+POPE reflectivity curve revealed that the structure of the POPE coating was quite similar to the POPE coating of the silicon wafer and the SLD profiles of the POPE bilayer were completely

identical for both. The only difference was the number of bilayers, which was slightly less (25 repetitions) for the Ti6Al7Nb coated Si-wafer. Again, the shape of the model curve was very sensitive to the intermediate layer, which was equivalent to the intermediate layer used previously for the silicon wafer. The final box model is given in Table 6.

Thus, the important result of this work is that drop-coating can be successfully applied to samples coated with the Ti6Al7Nb alloy. The POPE multilayer structure attached to such a surface is well ordered and seems to be stable in water

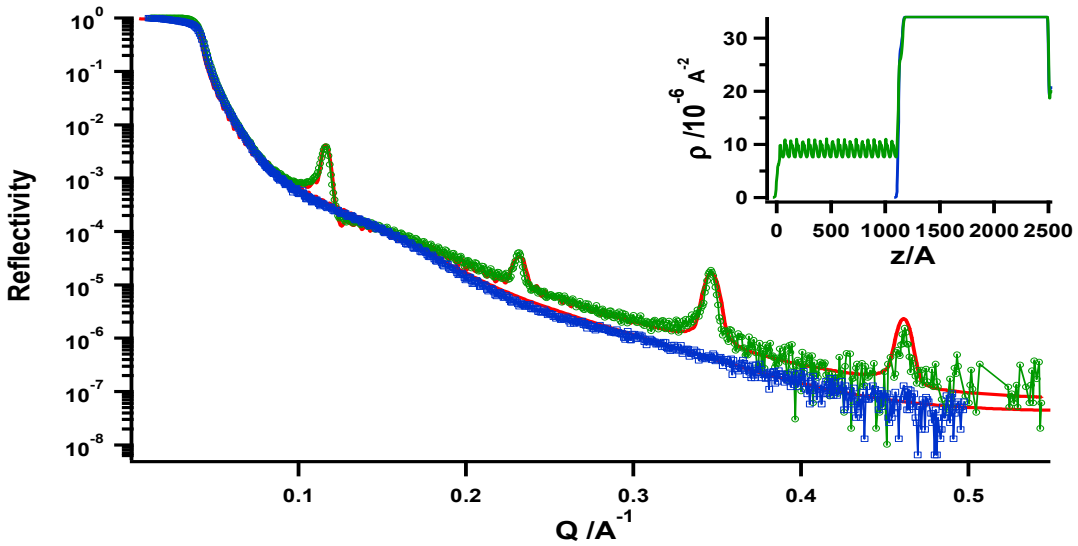

Figure 29. X-ray reflectivity of the titanium alloy substrate drop-coated with POPE. Blue cubic dots correspond to the uncoated Ti6Al7Nb substrate; Green round dots – POPE drop coating; The red curves – the theoretical curves.

Table 4. X-ray SLD profile of the Ti6Al7Nb+drop coated Si-wafer.

Sample	Material	Thickness, Å	SLD, 10^{-6} Å^{-2}	Roughness, Å
Ti6Al7Nb + POPE	Air	None	0	None
	Intermediate layer	26±1	6.5±0.5	8±2
	Lipid multilayer structure 25 repetitions			
	Water layer	3±1	9.6±0.5	2±1
	Head group	6±2	13±1	5±2
	Tail group	36.7±3	7.5±0.8	10±4
	Head group	6±2	13±1	5±2
	Water layer	3±1	9.6±0.5	2±1
	Basement			
	TiO_2	39±1	28±4	8.5±3
	Ti6Al7Nb	1390±6	36±1	10±3
	SiO_2	8±2	19±1	4±1
	Si	None	20±1	3±2

3.3 Controlled Deposition

3.3.1 X-ray Experiment – OPA coating

The comparison of the reflectivity curves of the uncoated and OPA-coated specimens clearly demonstrates that the curve shape is modified (see Figure 30). In the Q_z-range of 0.1 – 0.2 ($Å^{-1}$), the reflectivity of the Ti+OPA coated Si-wafer decays faster than that of the native specimen. The identical position of the "beating point" for both curves indicates that the chemical procedure did not alter the titanium dioxide layer. The reflectivity curve was fitted by adding an additional layer of OPA to the model used for the unmodified Ti coated Si-wafer (see Table 7). The SLD value for the OPA layer depends on both the chemical composition of the OPA molecule and the density of the layer, i.e., how densely the molecules are packed on the surface. The desirable density for this layer corresponds to the density of the alkyl chains of the lipid membrane at the condensed phase (0.86 g/cm^3). Under this assumption the SLD (8.3 10^{-6} $Å^{-2}$ – X-rays and -3.1 10^{-7} $Å^{-2}$ – neutrons) of the OPA layer was calculated by the Motofit program. For these SLD values, the thickness of the OPA layer was determined to be approximately 23 Å thick with a roughness of approximately 10 Å. This thickness value is in good agreement with previously reported values (19-22 Å) [69, 70] indicating that the titanium surface was fully coated with a monolayer of OPA with preferable packing.

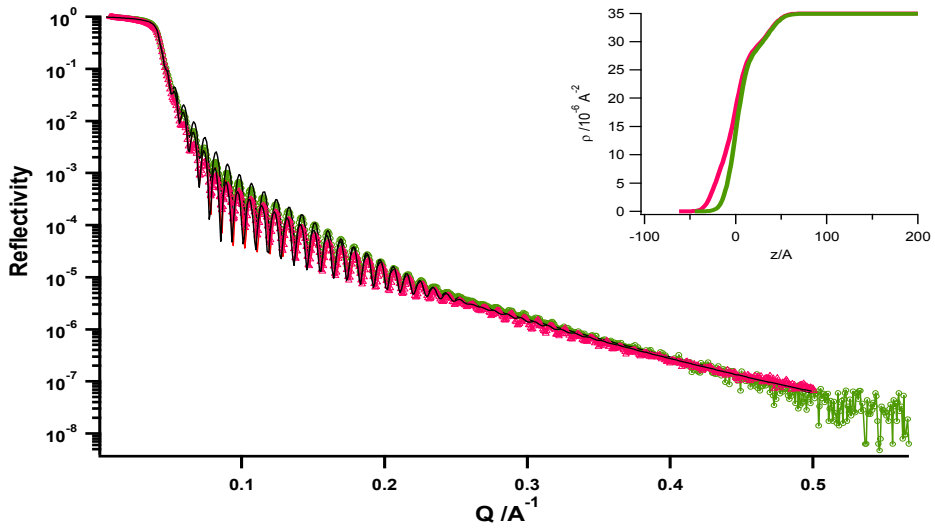

Figure 30. X-ray reflectivity curves. The green curve corresponds to the Ti coated Si-wafer, and the red curve corresponds to the Ti+OPA coated Si-wafer.

After the OPA modification of the Ti6Al7Nb coated Si-wafer, the reflectivity curve displayed a change in its slope similar to that for the first sample and displayed a shift in the position of the first maximum to 0.14 $Å^{-1}$ (see Figure 31). The following

model is constructed based on the assumption that the OPA coating procedure does not affect the titanium dioxide layer, as observed for the Ti coated Si-wafer.

To fit the curve, as in the previous case, one more layer was added to the SLD profile of the Ti6Al7Nb coated Si-wafer. The SLD value of this additional OPA layer was kept constant at the X-ray value of 8.3 10^{-6} $Å^{-2}$. The fitting of the layer thickness indicated that the best fit was obtained assuming a thickness of 15 Å and a roughness of 8.5 Å. This value for the thickness is less than the value for the first sample but can be explained by a tilt of the hydrocarbon tails in the monolayer due to an increased area per OPA molecule. Such a tilt has been observed by Kuhl for octadecyltrichlorosilane covalently attached to a quartz plate [71], where the sinus of the tilt angle was determined as the ration between the found thickness of the monolayer and the length of octadecyltrichlorosilane molecule. In our case, this tilt appears because the OPA molecules are most likely not attached to Al and Nb. The angle of the tilt in this case equals 51°.

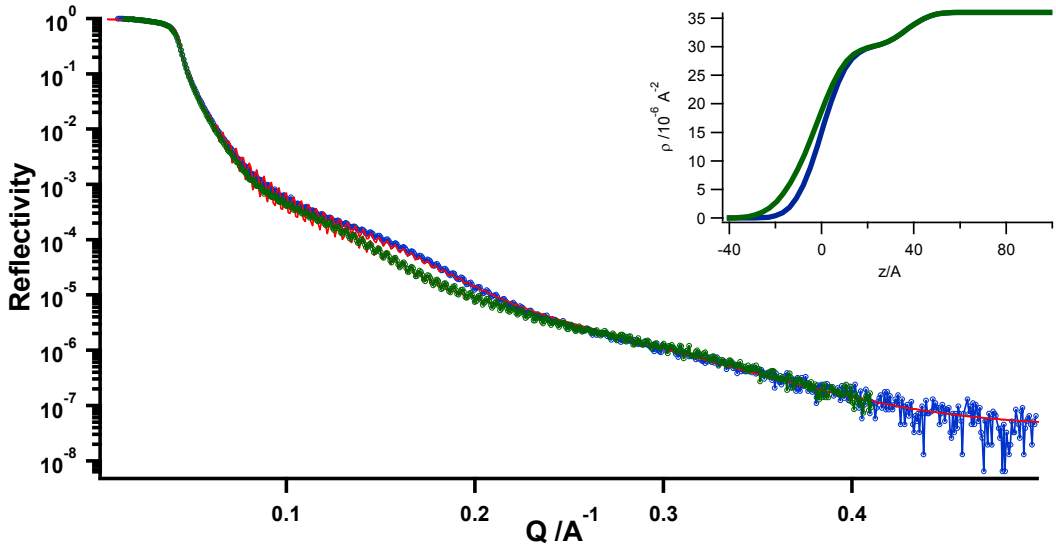

Figure 31. X-ray reflectivity curves of the Ti6Al7Nb coated Si-wafer (blue curve) and the Ti6Al7Nb+OPA coated coated Si-wafer (green curve).

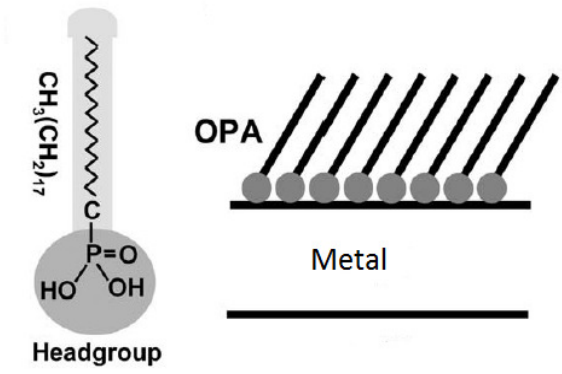

Figure 32. Separate OPA molecule and "tilted" monolayer of OPA on top of the metal surface.

Table 7. OPA coating, X-ray SLD profiles

Sample	Material	Thickness, Å	SLD, 10^{-6}Å^{-2}	Roughness, Å
Ti+OPA coated Si-wafer	Air	None	0	None
	OPA layer	23±2	8.3±1	10±3
	TiO_2	37±1	30±4	10±3
	Ti	636±5	36±2	10±3
	SiO_2	None		
	Si	None	20.1	3
Ti6Al7Nb +OPA coated Si-wafer	Air	None	0	None
	OPA layer	15.3±1	8.3±1	9±3
	TiO_2	39±1	28±4	8.5±3
	Ti6Al7Nb	1390±6	36±1	10±3
	SiO_2	8±2	19±1	4±1
	Si	None	20±1	3±2

3. 3. 2 Neutron Experiment - From OPA Coating to Protein Binding

The goal of the study is to clarify whether a biomimetic phospholipid coating comprised of several bilayers can be formed on a metal surface and whether it is stable enough to persist under physiological conditions. Neutron reflectivity experiments are ideally suited to investigate samples under realistic conditions because neutrons can probe liquid-solid interfaces due to their large penetration depth in matter. Another advantage of using neutrons as a probe is their high sensitivity to low-mass materials, which creates sufficiently large scattering contrasts to distinguish biological objects. The SLD contrast between lipid alkyl chains, head groups and D_2O is much stronger for neutrons compared to X-rays, and this contrast allows the structure to be studied in more detail. The experiment was performed on the time of flight reflectometer Figaro (ILL, France).

Three Ti-coated samples were prepared for this measurement. According to the neutron data analysis, all three were initially identical and had a SiO_2 layer of 40 Å, a TiO_2 layer of 24 Å and a Ti layer of 368 Å (for more details, see Chapter 3. 1. 3). Two of the samples were coated with OPA; the third sample was left unmodified as a reference sample. All other treatments, such as heating and sonication in organic solvents, were applied to all three samples to determine how the mechanical stress during the OPA coating procedure affects the titanium surface.

The reference measurement of the heated Ti coated Si crystal was performed against D_2O (see Figure 33). Comparing the reflectivity curves measured before and

after heating of the Ti coated crystal reveals that the oscillations from titanium are shifted. This shift becomes larger for each subsequent oscillation ($\Delta Qz=0.00294$ Å^{-1} for the first oscillation, 0.0044 Å^{-1} for the second, 0.0055 Å^{-1} for the third). This shift indicates that the titanium layer becomes smaller, most likely due to the oxidation process that occurred between the two measurements. In addition, in the second reflectivity curve, the amplitude of the oscillations is smaller than the amplitude in the first curve. Because these two measurements were performed with the same resolution, 4.2% weaker oscillations indicate that an additional roughness should be applied to fit the data. To take this additional roughness into account, a gradient in the SLD profile between the TiO_2 layer and D_2O was applied (see the SLD profiles in Figure 33).

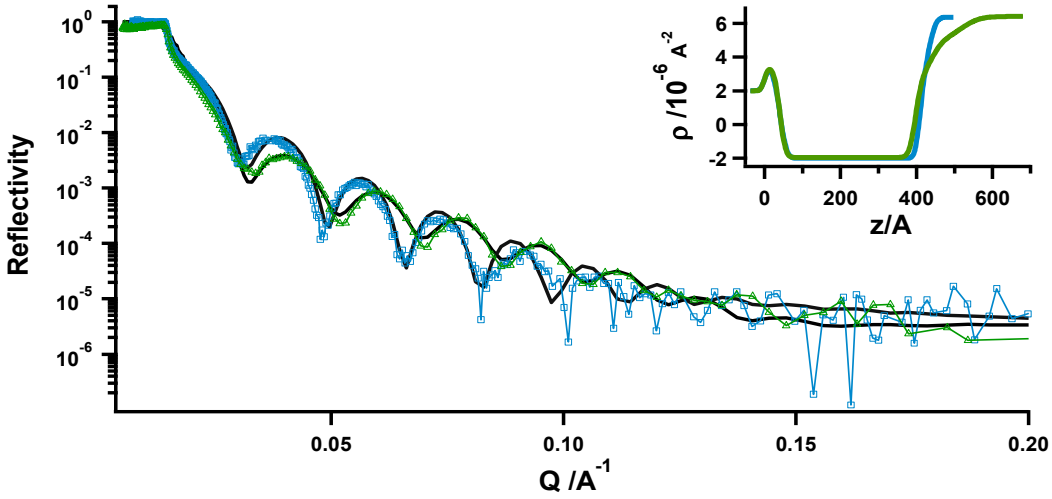

Figure 33. Neutron reflectivity curves of the Ti coated Si-crystal measured vs. D_2O: 1) the blue curve was measured before the heating procedure; 2) the green curve was measured after the heating procedure. The SLD profiles are presented in the upper-right corner, the start of the scale corresponds to the border Si/SiO_2.

The easiest explanation of the appearance of such a gradient is that some undesired cracks at the surface are filled with D_2O and thus change the average SLD of the last layer of titanium dioxide. Based on the scattering length density profile, the average depth of the cracks is approximately 40 Å; this depth corresponds roughly to the thickness of the titanium dioxide layer. These undesired cracks in the TiO_2 layer could be the result of the heating procedure to 120 °C as a part of the OPA covering (see reference [25]).

To prove that cracks had appeared the Ti coated crystal was probed by SEM. In contrast to the SEM images of a freshly prepared Ti coated Si crystal (before heating), the SEM images of the heat treated Ti coated Si crystal demonstrated that

some cracks were present on the surface (see Figure 34). The typical width of the cracks was in a range of 3000 Å. The cracks could have occurred because the thermal expansion coefficient for titanium (titanium dioxide) is three times larger than the thermal expansion coefficient for silicon – 9 x 10^{-6} $°C^{-1}$ and 3 x 10^{-6} $°C^{-1}$, respectively [72]. This effect is not apparent by X-ray reflectivity because the silicon wafers used for the titanium deposition are ten times thinner than the silicon crystals, and thus, the tensile force applied to the titanium layer during the heating process is ten times weaker. Thus, the tension force is not strong enough to lead to crack formation.

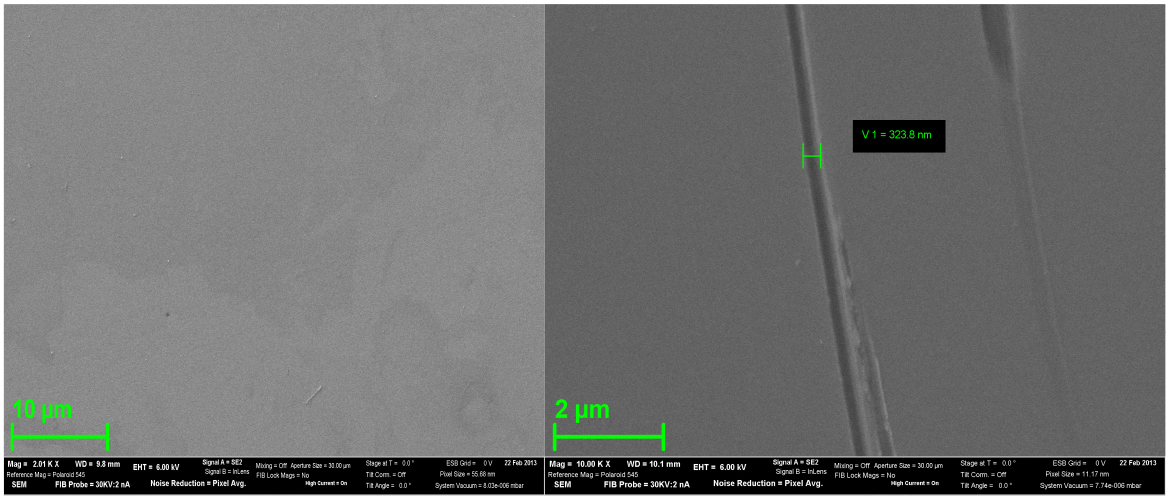

Figure 34. Typical SEM pictures of the Ti coated Si-crystal before heating (A) and after heating (B)

Based on the curve analysis, the resulting model of the fitting procedure consists of a layer of silicon dioxide with a thickness of 40 Å and a roughness of 8 Å, a layer of titanium with a thickness of approximately 358 Å and a roughness of 12 Å and, finally, a top layer of titanium dioxide with a thickness of approximately 48 Å and a roughness of 13 Å.

Next, two Ti+OPA coated Si-crystals were also probed against D_2O. The two crystals yielded similar reflectivity curves, demonstrating the excellent reproducibility of the sample preparation (Figure 35, one curve as an example).

By comparing the reflectivity curves of the heated Ti coated crystal and the additionally OPA coated, the following changes in the curve shape were observed in the region below 0.07 $Å^{-1}$:

1) The intensity of the reflectivity curve of the OPA coated specimen was lower than that of the unmodified one.

2) The first oscillation of the reference curve at Q_z=0.0385 Å^{-1} split into two oscillations for the reflectivity curve of the OPA covered specimen: the first oscillation at Q_z=0.032 Å^{-1} and the second one at Q_z=0.044 Å^{-1} (see Figure 35).
For Q_z higher than 0.07 Å^{-1}, the reflectivity curves have almost the same shape up to the level of background.

Because the positions of the oscillations have not changed at high Q_z values, we can apply the model found for the heated Ti coated crystal without changes as a basic assumption for the Ti+OPA coated crystal in a first approximation.

The modeling of the curve demonstrated that only one layer has to be added to the scattering length density profile of the heated Ti coated crystal without OPA modification. This additional layer is interpreted as an OPA monolayer. The SLD of this layer corresponded to the SLD of a CH_2 group with the density of the alkyl chains of the lipid membrane at the condensed phase (0.86 g/cm^3). The thickness of the OPA layer was determined to be 24 Å.

As for the analysis of the reference curve, some gradient must be used for satisfactory modeling (see Table 8). To examine the surface for cracks, the Ti+OPA crystal was also probed by SEM, which indicated similar cracks on the surface as for the Ti coated Si-crystal after heating.

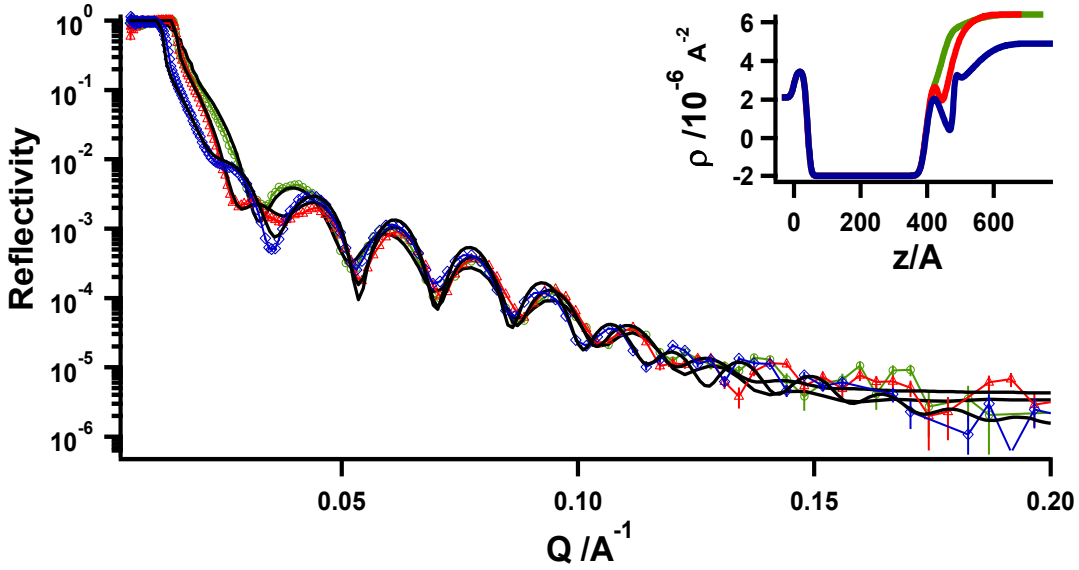

Figure 35. Neutron reflectivity curves measured against D_2O and the corresponding SLD profiles of 1) the Ti coated Si-crystal after heating – green dots; 2) the Ti+OPA coated Si-crystal – red dots; 3) the Ti+OPA+POPE crystal – blue dots.

The system of the asymmetric bilayer consisting of OPA plus POPE layers was then prepared. The Langmuir-Blodgett and Langmuir-Schaeffer technique were used for the POPE deposition as described in Chapter 2. 1. 3. 2 Langmuir-Blodgett

Deposition. During the measurement, the sample's cell was connected to the thermostat to maintain the temperature inside the cell at 20°C to maintain the POPE lipids in the gel phase. It was expected that the lipids would be better ordered than in the liquid crystalline state. The reflectivity curves obtained after the LB deposition of POPE lipids (Ti+OPA+POPE+2xPOPE coated crystal) are shown in Figure 36.

The first observation in the analysis of the reflectivity curve measured against D_2O is the shift in the critical angle. The shifting of the plateau is an indication that some H_2O due to incomplete H_2O-D_2O exchange was still present in the sample chamber during the measurement process.

The sample was installed into the sample's cell in H_2O to avoid missing POPE lipids after the Langmuir-Schaeffer transfer. The H_2O in the sample cell was then exchanged with D_2O. To perform this exchange, we injected D_2O into the chamber. The injected volume of D_2O was 5 times higher than the volume of the cell. However, this volume was insufficient for complete exchange. The reflectivity curve of the Ti+OPA+POPE+2xPOPE crystal was successfully fitted after applying the D_2O-H_2O mixture (80% -20%) as the real contrast in this measurement (see the SLD profile in Figure 36).

The second observation was a slight shift of oscillations to the region of smaller Q_z compared to the OPA-coated sample (see Figure 35). This shift can only indicate that there is an additional coating on top of the OPA layer.

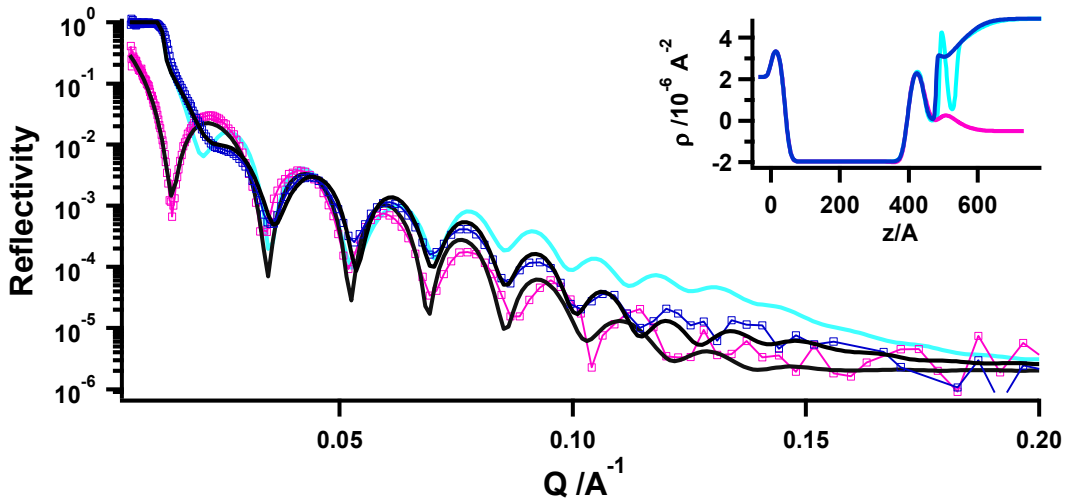

Figure 36. Neutron reflectivity curves of the Ti+OPA+POPE coated crystal, contrast variation experiment: 1) blue square **– vs. D_2O-H_2O mixture (80-20); 2) pink** square **– vs. H_2O; 3) turquoise curve – the theoretical curve expected for an ideal coating.**

The attachment of an additional phospholipid layer to the Ti+OPA coated crystal can also be concluded from the reflectivity curve measured from this sample

and presented in Figure 35. The first two oscillations, at Q_z=0.032 $Å^{-1}$ and Q_z=0.044 $Å^{-1}$, become two to three times stronger compared to the corresponding oscillation of the reflectivity curve obtained from the Ti+OPA coated crystal. According to the simulation such a change in the shape of the reflectivity curve should indicate an increased thickness of the hydrogen-rich region between Ti dioxide and the contrast mixture at the solid – liquid interface.

The final models for fitting take into account all three steps of POPE deposition (see Figure 37) and contain the following layers:

1) silicon crystal; 2) silicon dioxide layer; 3) titanium layer; 4) titanium dioxide layer; 5) OPA layer; 6) tail group region 1; 7) head group region 1; 8) tail group region 2; 9) head group region 2; 10) intermediate - gradient layer.

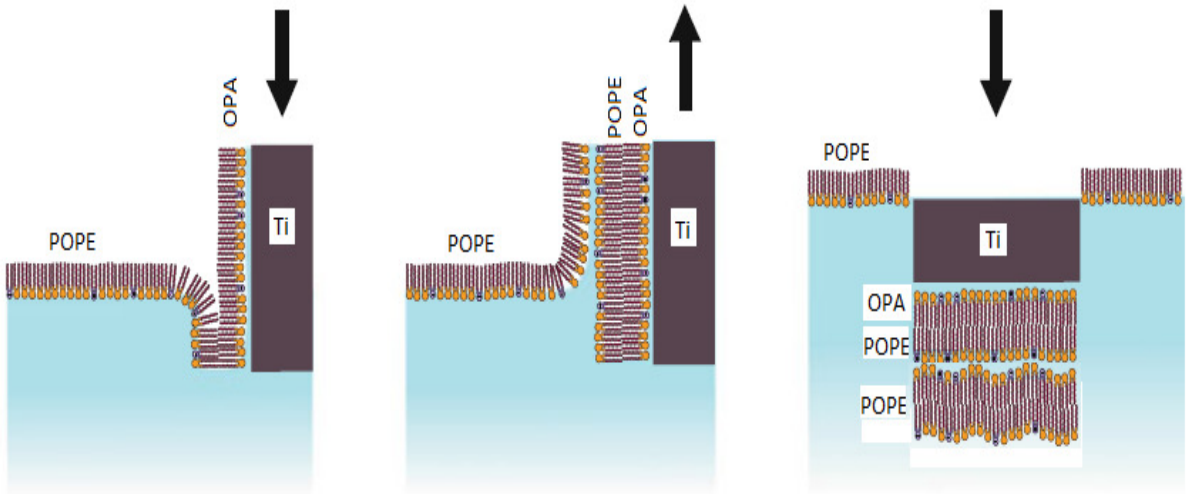

Figure 37. POPE deposition. Adapted from [73]

The fitting parameters for the first five layers (up to the OPA layer) are fixed and were obtained previously from the fit of the Ti+OPA coated Si-crystal. The water layer between the POPE monolayer adjacent to the OPA and the next POPE bilayer cannot be distinguished within the data because this water layer is only a few angstroms thick and the border area in the SLD profile is smeared out due to the cracks in the TiO_2 layer. These two head group regions and the water layer are combined into one box-layer titled “Head group region 1” in Table 8.

The present work focuses on SLD values and roughnesses because these parameters provide information about the quality of the coating at each step of the deposition. The thicknesses of the tail group and the head group were kept fixed at 34 and 8 (Å), respectively. These values of the thicknesses were based on values in the literature [74, 75] for the deposition of DPPE lipid in a similar manner on the top

of silicon and quartz surfaces. Figure 30 shows the theoretical curve in the case of the ideal coating, in which the SLD of the hydrocarbon region is -0.3 x 10^{-6} $Å^{-2}$ and the SLD of the PE head group is 2.2 x 10^{-6} $Å^{-2}$. The fit demonstrates that the measured SLD for the tail region should be higher because the coating is not complete and these layers contain some heavy water molecules.

From the SLD values, it is possible to predict the percent of the coated surface from the calculation:

$\rho_{measured} = \phi\ \rho_{tail's} + (1- \phi)\rho_{contrast}$

Here, it is possible to say that the LB deposition coated approximately 65% of the surface and that the Langmuir-Schaeffer transfer led to 45% (see Figure 38). This model is confirmed by the analysis of the second reflectivity curve measured from the Ti+OPA+POPE+2xPOPE crystal in H_2O.

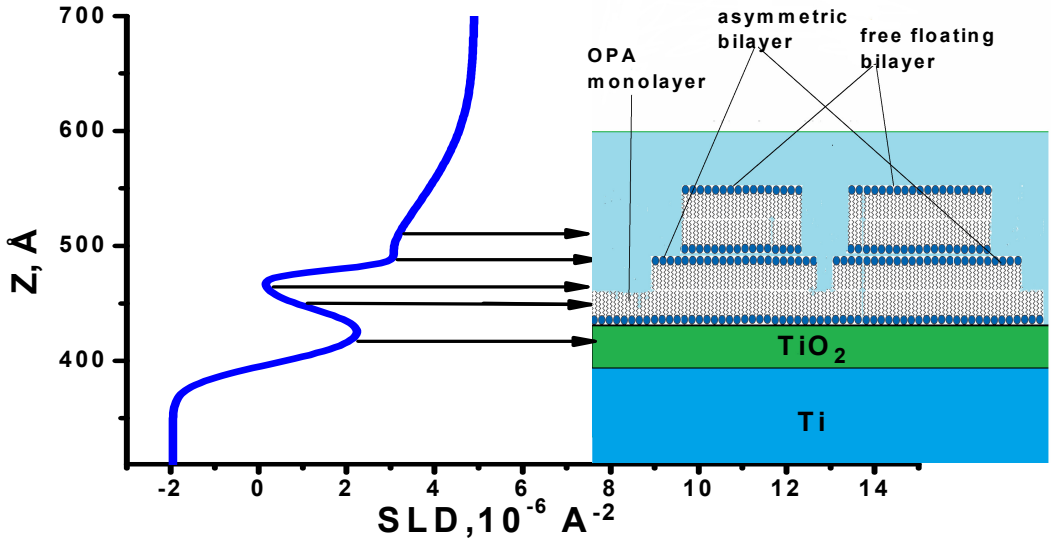

Figure 38. Schematic correlation between the Ti+OPA+POPE+2xPOPE SLD profile obtained before the protein injection and the real coating.

As the last step, deuterated HSA was injected into the sample chamber containing the Ti+OPA+POPE+2xPOPE crystal. The protein was dissolved in D_2O; the concentration of the protein in the solution was 30 mg per 10 mL. A total of 4 mL of this solution was injected into the sample cell (the volume of the cell was 2 mL). The time provided for the absorption of the protein was two hours.

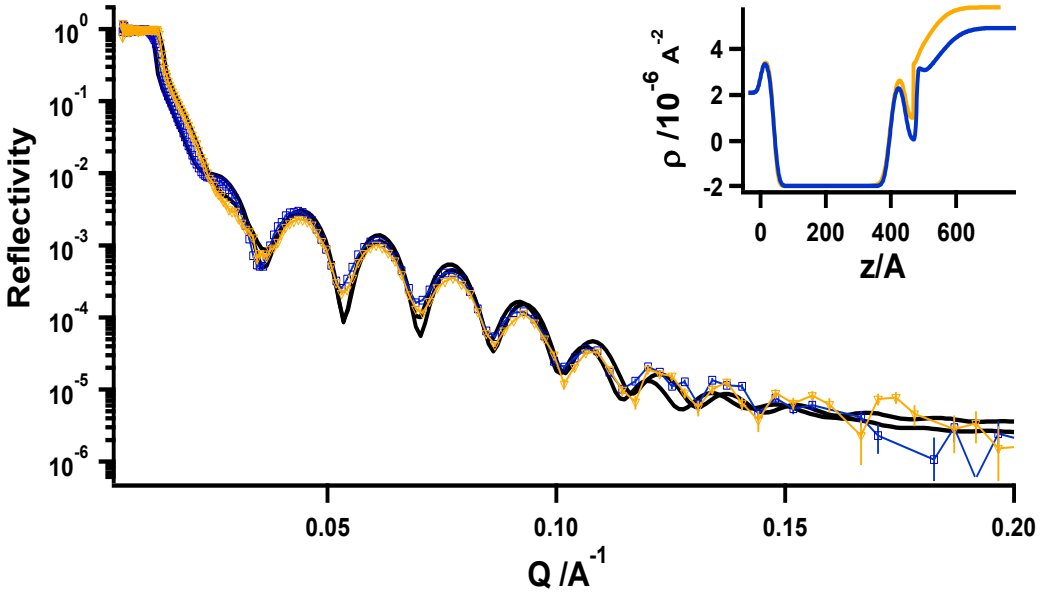

Figure 39. Neutron reflectivity curves – effect of protein exposure. 1) The blue curve was measured before the injection of the protein; 2) the orange curve was measured after the injection of the protein.

The reflectivity curve measured from the last sample displays a small shift in the critical region. The shift is a result of the last injection of D_2O with the protein. The data analysis (see Figure 39) indicates that the hydrocarbon reach region is becoming smaller because the first oscillation at Q_z=0.032 $Å^{-1}$ is almost invisible.

This change cannot be fitted by adding one more layer to the profile of the Ti+OPA+POPE+2xPOPE crystal. Most likely, the protein was not attached to the surface, and moreover, the top POPE bilayer was unstable and washed away at the last contrast change. However, it seems that the first POPE monolayer is stable and well attached to the OPA layer – according to the fit, approximately 60% of the surface is still coated.

Table 8. Neutron scattering length densities

Sample	Material	Thickness, Å	SLD, 10^{-6} $Å^{-2}$	Roughness, Å
Ti coated Si-crystal after heating vs. D_2O	Si	None	2	None
	SiO_2	40±5	3.4	8±4
	Ti	357±2	-1.96	12±2
	TiO_2	48±3	2.4	13±2
	Gradient layer	60±10	6.36	60±10
	D_2O	None	6.36	0
Ti+OPA coated Si-crystal vs. D_2O	Si	None	2	None
	SiO_2	40±5	3.4	8±4
	Ti	357±2	-1.96	12±2
	TiO_2	48±3	2.4	13±2
	OPA layer	24±1	-0.3	12±2
	Gradient layer	60±10	6.36	60±10
	D_2O	None	6.36	0
Ti+OPA+POPE+2x POPE bilayer vs. D_2O-H_2O mixture (80-20)	Si	None	2	None
	SiO_2	40±5	3.4	8±4
	Ti	357±2	-1.96	12±2
	TiO_2	48±3	2.4	13±2
	OPA	24±1	-0.3	12±2
	Tail group region 1	17±2	1.5±0.4	12±4
	Head group region 1	16±2	2.6±0.4	5±2
	Tail group region 2	34±3	2.2±0.4	10±3
	Head group region 2	8±1	3.4±0.4	5±3
	Gradient layer	60±10	4.9	60±10
	D_2O	None	4.9	0
Ti+OPA+POPE+2x POPE vs. H_2O	Si	None	2	None
	SiO_2	40±5	3.4	8±4
	Ti	357±2	-1.96	12±2
	TiO_2	48±3	2.4	13±2
	OPA	24±1	-0.3	12±2
	Tail group region 1	17±2	-0.3±0.4	12±4
	Head group region 1	16±2	1.2±0.4	5±2
	Tail group region 2	34±3	-0.4±0.1	10±3
	Head group region 2	8±1	0.5±0.3	5±3
	Gradient layer	60±10	-0.5	60±10
	D_2O	None	-0.5	0
Ti+OPA+POPE+2xPOPE vs. D_2O after adding dHSA	Si	None	2	None
	SiO_2	40±5	3.4	8±4
	Ti	357±2	-1.96	12±2
	TiO_2	48±3	2.4	13±2
	OPA	24±1	-0.3	12±2
	Tail group region 1	17±2	1.5±0.4	12±4
	Head group region 2	8±1	3.4±0.4	5±3
	Gradient layer	60±10	6	60±10
	D_2O	None	6	0

3. 4 X-ray Characterization of POPE Multilayer Structure

As mentioned in the previous chapter, if pure titanium is used as an implant material, the drop-coating method is not an appropriate way to deposit POPE, and an alternative method is needed. The OPA pre-coating followed by applying the Langmuir-Blodgett technique as it is shown in the previous Chapter 3.3 improve the distribution of POPE over a titanium surface and lead to a stable OPA-POPE coating, however, a significant part of the surface remains uncoated by lipids. In order to perform a complete POPE coating of a titanium surface an air brush can be used to spread lipids evenly. In this case, lipids are deposited onto the pure titanium surface as an aerosol so that the drops of methanol and chloroform evaporate before they start to move on the surface. The air brush method of coating is also easier to use than the spin coating method, which is difficult to apply for a real implant with a complicated shape.

The spray-coated titanium surface was probed by SEM and AFM (see Figure 40 and Figure 41). The images indicate that the surface was coated with many POPE “islands” with an average size of 20 μm.

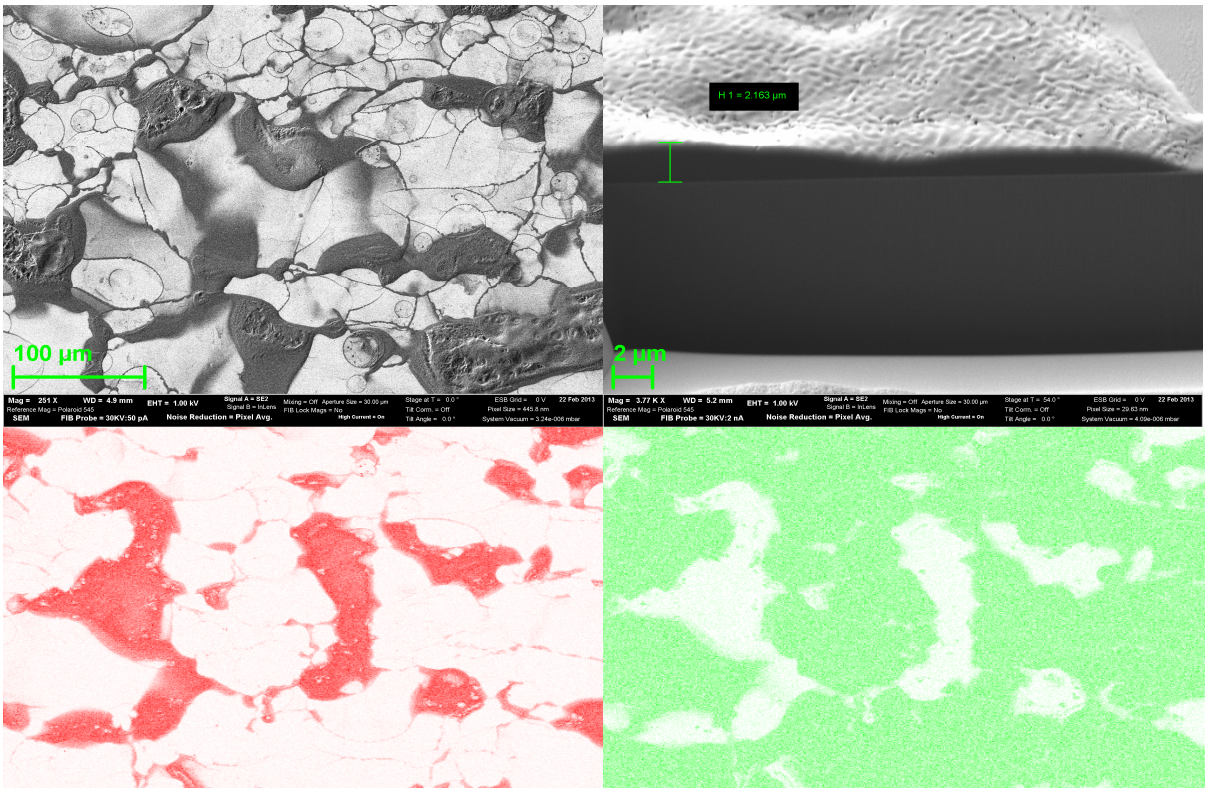

Figure 40. SEM images of the spray-coated Ti coated Si-wafer: 1) overview picture; 2) cut of the surface; 3-4) mapping of the chemical composition: the red color corresponds to carbon, and the green color corresponds to titanium.

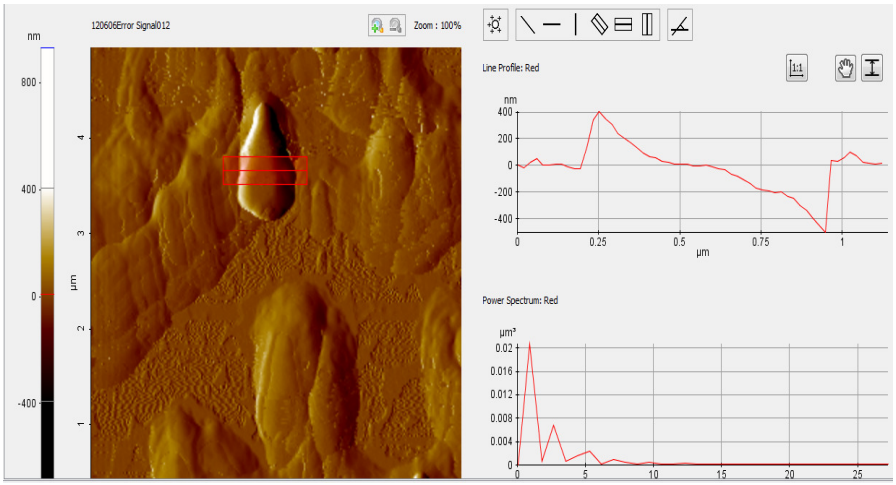

Figure 41. AFM image of the spray-coating

To evaluate the thickness of these islands, the spray-coated sample was cut with a Ga beam with an energy of 30 kV (see the second image in Figure 40). This cut revealed that the thickness of the islands was on the order of 1-2 μm. The mapping of the chemical composition demonstrated that most of the POPE lipids were concentrated on these islands; however, the areas between the islands were also coated with POPE, which is an important result with respect to implant modification.

The Ti+spray coated Si-wafer was examined before exposure to water for 4 hours and the day after exposure by X-rays. The behavior of the reflectivity curve is similar to the case of the Ti+drop coated Si-wafer: 1) the curve measured just after the deposition has no Bragg peaks, and only a weak peak is visible in the off-set scan at Qz=1.05; 2) the Bragg peaks appear after the sample was exposed to water (see Figure 42). As in the case of the drop-coated samples, the appearance of the Bragg peaks after exposure to water is due to the decrease in roughness due to hydrophobic forces. Therefore the POPE multilayer structure, which was smeared out by roughness, is better organized after exposure to water.

The strong Bragg peaks shown in Figure 42 clearly demonstrate that the average number of POPE bilayers in the multilayer structure was larger for the Ti+spray coated Si-wafer than for the drop-coated plate, for which only one weak peak was observed. Thus, the spray coating method is more appropriate for depositing a POPE multilayer structure on the titanium surface.

Before fitting the reflectivity curves measured from the spray-coated sample, one specific feature of the curves must be considered. As clearly shown in Figure 42,

there is a decrease in intensity at the region in which the total reflection is observed for the drop-coated samples. Such a decrease was also reported by Koltover [76] in his investigation of bacteriorhodopsin membranes on top of a silicon surface. The decrease in the intensity at a critical edge can be explained by incorporating absorption into the model, which cannot be negligible in this case due to the huge amount of POPE lipids attached to the surface (see Figure 40). For the drop-coating, most of the substrate is coated with only 25-30 POPE bilayers, which leads to a smaller decrease in the specular intensity at the critical edge compared to the experiment in which an air brush was used.

There is one important difference, however, between the spray-coating and Koltover's investigated system. The SEM and AFM images (Figures 40 and 41) demonstrate that there are two types of coating present: 1) the first coating - very thick islands that are quite rough; and 2) the second coating – the thin coating, which is located in between the islands. The sizes, i.e. the average diameter of the area of these two types of coatings is about to 150-200 μm that is larger than the coherence length of the used x-ray or neutrons that expected to be in order 1-10 μm, therefore the reflectivity curve should be the result of two incoherent contributions. The model developed for the data analysis is the following:

1) The ordered multilayer structure is placed close to the metal surface and leads to the appearance of Bragg peaks.
2) The unstructured part of the lipids is modeled by a very thick layer with a SLD corresponding to the SLD of the "heads-and-tails" group.

Thereby, the final reflectivity can be calculated as:

$R=\alpha R_{\text{multilayer structure}}+(1-\alpha)R_{\text{unstructured lipids}}$,

where α is the coating coefficient, which ranges from 0 to 1, $R_{\text{multilayer structure}}$ is the reflectivity of the first type of coating, and $R_{\text{unstructured lipids}}$ is the reflectivity of the second type of coating.

The blue reflectivity curve presented in Figure 43 matches $R_{\text{multilayer structure}}$, and it is generated for 50 bilayers of POPE on top of the Ti coated Si-wafer. The repeat distance corresponding to the Bragg peaks considered here is 1 Å smaller than that for the drop-coated samples, and thus, the SLD profile of the bilayer cannot be determined without changing the fitting parameters of the data from the drop-coated silicon wafer. To obtain an appropriate fit, the profile was changed by reducing the

layer of the tail group to 35.7 Å. According to the simulations, all other parameters of the profile seem to remain the same as for the drop-coated samples.

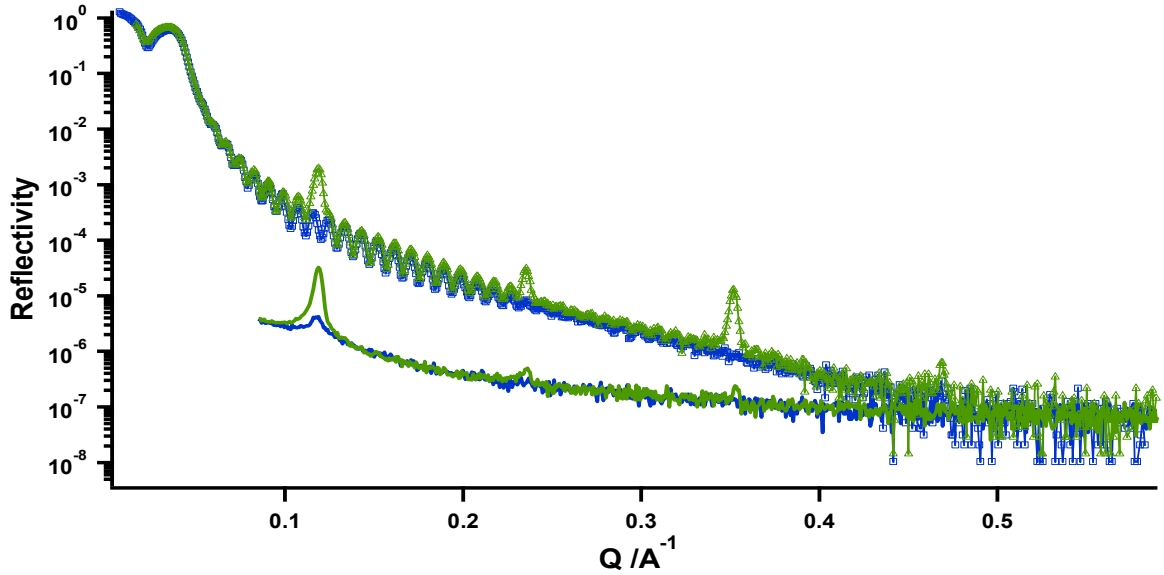

Figure 42. X-ray reflectivity and off-set curves of the Ti+spray coated Si-wafer: 1) the blue curves were measured before exposure to water; 2) the green curves were measured the day after exposure.

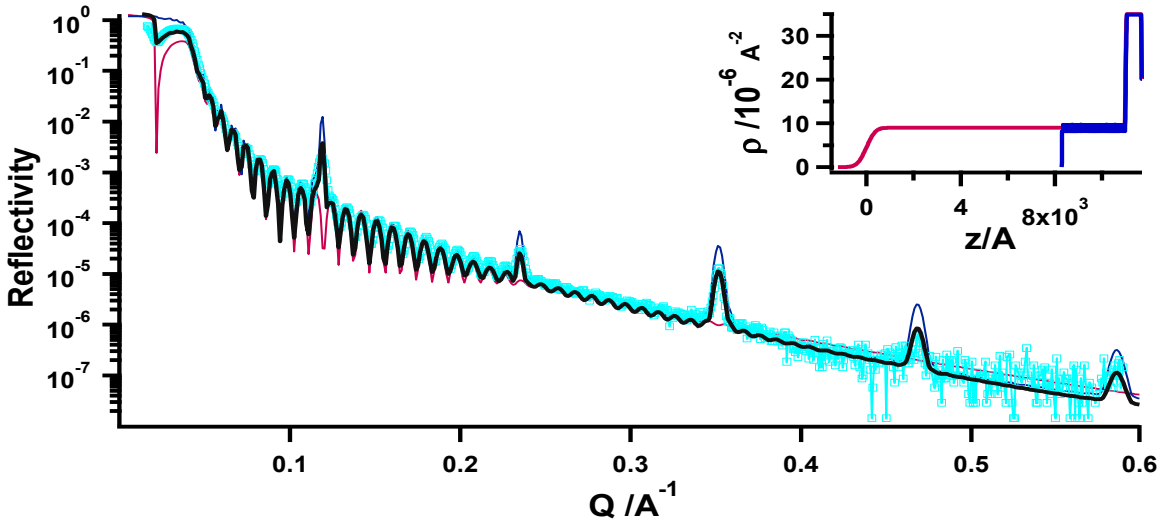

Figure 43. The model of incoherent scattering: 1) the cyan curve is the reflectivity scan of the Ti+spray coated Si-wafer; 2-3) the blue and violet curves are the model curves, which correspond to the multilayer structure on top of the metal surface and to the thick unstructured layer, respectively; 4) the black curve is the final model curve obtained assuming incoherent scattering.

The $R_{\text{unstructured lipids}}$ reflectivity is also presented in Figure 43 as the violet curve. To generate this curve, the model of a very thick and rough layer placed on top of the Ti coated Si-wafer was used. The SLD value for this thick layer was calculated as an average of the SLDs of the tail group and the head group. The simulations indicate that the decrease in the intensity close to the critical angle region depends on the

imaginary part of the SLD and on the thickness and roughness of this layer. The thickness of the thick layer is 1.1 μm based on the SEM images, and the image SLD is calculated for the POPE molecule as $5*10^{-8}$ $Å^{-2}$. According to the simulations, the roughness of the thick layer at such a thickness and SLD value needs to be in the range of 300 Å to 500 Å, which was confirmed by the SEM and AFM measurement.

Finally, the coating coefficient α was determined to be approximately 0.6 - 0.7, which fits both the SEM data and the X-ray reflectivity experiment. The final fitting curve and the corresponding SLD profiles are given in Figure 43. All of the fitting parameters can be found in Table 9.

Table 9. X-ray SLD profiles of the Ti+spray coated Si-wafer

Sample	Material	Thickness, Å	SLD, 10^{-6} $Å^{-2}$	Roughness, Å
Ti+POPE spray-coating	air	None	0	None
	Unstructured lipids			
	Thick coating	11000±1000	ReSLD 10±0.5 ImSLD 0.05±0.01	350±50
	Lipid's multilayer structure 50 repetitions			
	Water layer	3±1	9.6±0.5	2±1
	Head group	6±2	13±1	5±2
	Tail group	35.7±3	7.5±0.8	10±4
	Head group	6±2	13±1	5±2
	Water layer	3±1	9.6±0.5	2±1
	Basement			
	TiO_2	37±1	30±4	10±3
	Ti	636±5	36±2	10±3
	Si	None	20±1	3±1

The main difficulty of the analysis is that the structure of the thick layer is not clear. From the X-ray data, it is not possible to determine if the thick layer contains some well-organized bilayers that will contribute to the Bragg peaks. Simulations are not sensitive to position of such a multilayer structure (see the simulations in Figure 44). From the X-ray reflectivity experiment, it is only possible to conclude that the amount of POPE lipids on the titanium surface remains constant after the sample's exposure to water. The precise argument for this conclusion is that the decrease in the intensity at the critical angle remains the same in the reflectivity curves measured before and after exposure to water.

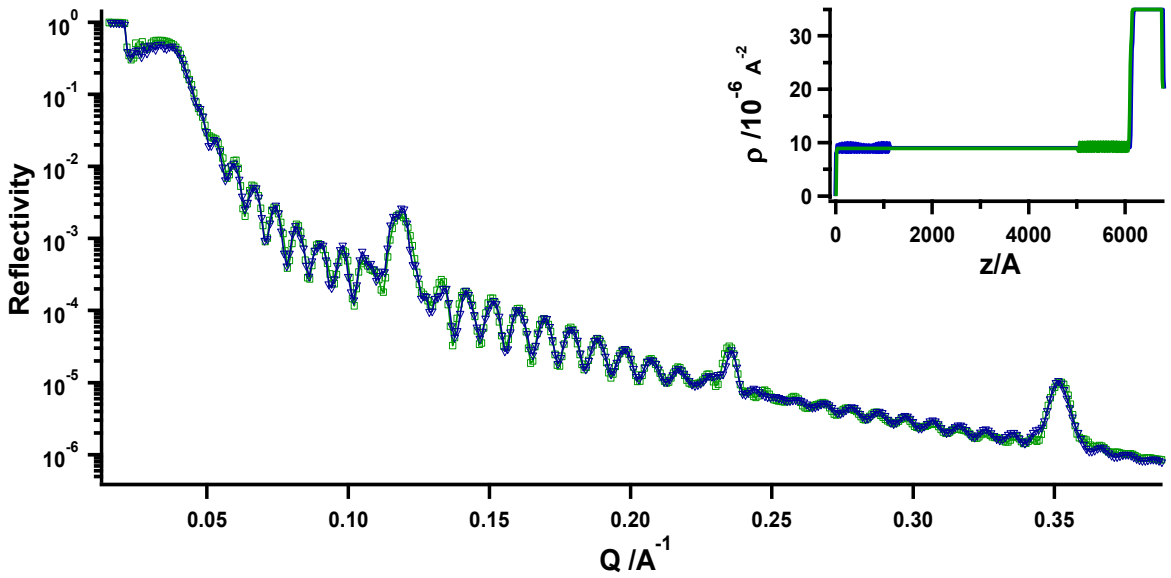

Figure 44. X-ray reflectivity simulation: 1) the blue curve corresponds to the case in which a well-organized POPE multilayer structure is placed on the titanium surface and the thick unstructured layer is placed on it; 2) the green curve corresponds to the case in which the multilayer structure is placed on the titanium surface underneath the thick layer.

Because there is no loss of POPE lipids after exposure to water, all POPE lipids must be organized in bilayers. Nevertheless, the measured Bragg peaks correspond only to 30 bilayers, with a maximum of 60 bilayers. Such behavior has been mentioned in a number of papers by Salditt [66] in which the theory of thermal fluctuation was developed. According to this theory, some well-ordered bilayers that are flat on a macroscopic scale can be found close to a solid substrate. In turn, thermal fluctuations play a role in the lipid bilayers that are located away from a solid surface such that the higher orders disappear due to the loss of the long-range order. The amplitude of the thermal fluctuation is limited only for a finite number of bilayers in a multilayer structure [50]. For a bulk system, the amplitude of the oscillations is macroscopic in scale, which is the case for our system – POPE bilayers in the islands are dramatically smeared out. To clarify the number of macroscopically flat bilayers close to the solid flat surface, neutron experiments were performed as shown in the next section.

3. 5 Neutron Characterization of the POPE Multilayer Structure

This part of the work presents neutron investigations of the POPE coating to characterize the structure of the coating under wet conditions. The one-dimensional SLD profile in the direction normal to the membrane plane of the POPE bilayer was first calculated by performing a neutron diffraction experiment. The replacement of water by heavy water facilitates phasing in a one-dimensional diffraction, which is not possible for X-ray diffraction. Furthermore, the amount of water absorbed by the POPE membrane can be determined from the diffraction experiment.

The spray-coating was then investigated in a liquid environment. It is important to directly clarify the structure of the implant coating in a liquid environment, and the use of neutrons to perform these experiments in a solid-liquid cell with a thin water layer is suitable for our purposes.

The neutron reflectivity part of this work began with the investigation of the spray-coating of the Si surface. A 2D detector was used for data collection, which allowed us to simultaneously detect the diffuse scattering, providing information about the lateral correlations in POPE bilayers.

Finally, the spray-coating of a titanium surface was examined by neutron reflectivity experiments. This study allowed us to observe the changes in the structure of the coating due to adhesion of the protein and to investigate the behavior of this coating at a range of physiological temperatures.

3. 5. 1 Calculation of the Membrane SLD Profile

The experiment presented below was performed on the membrane diffractometer V1 at the Berlin Neutron Scattering Center of the Hahn-Meitner-Institute (Berlin, Germany).

The lamellar spacing of the lipid bilayer was determined from the observed 2θ values of the Bragg peak positions $n\lambda=2d\sin\theta$, where n is the diffraction order and λ is the selected neutron wavelength (4.53 Å). The d spacing of the POPE bilayer was determined to be 60 Å ± 0.5 Å at 20 °C and 50 Å ± 0.5 Å at 37 °C.

The integrated intensities were analyzed by a Gaussian function, which can be used in this case as a suitable model for describing the shape of the reflection (see some example of the peak analysis in Figure 45). The intensity was also corrected according to the absorption and Lorentz factor. Table 10 summarizes the structure

factors obtained from the analysis of the Bragg peaks. The use of the different D_2O:H_2O mixtures permitted the determination of the phase assignment of the structure factor (see Figure 45) because the structure factors are linearly related to the D_2O:H_2O ratio [77, 78].

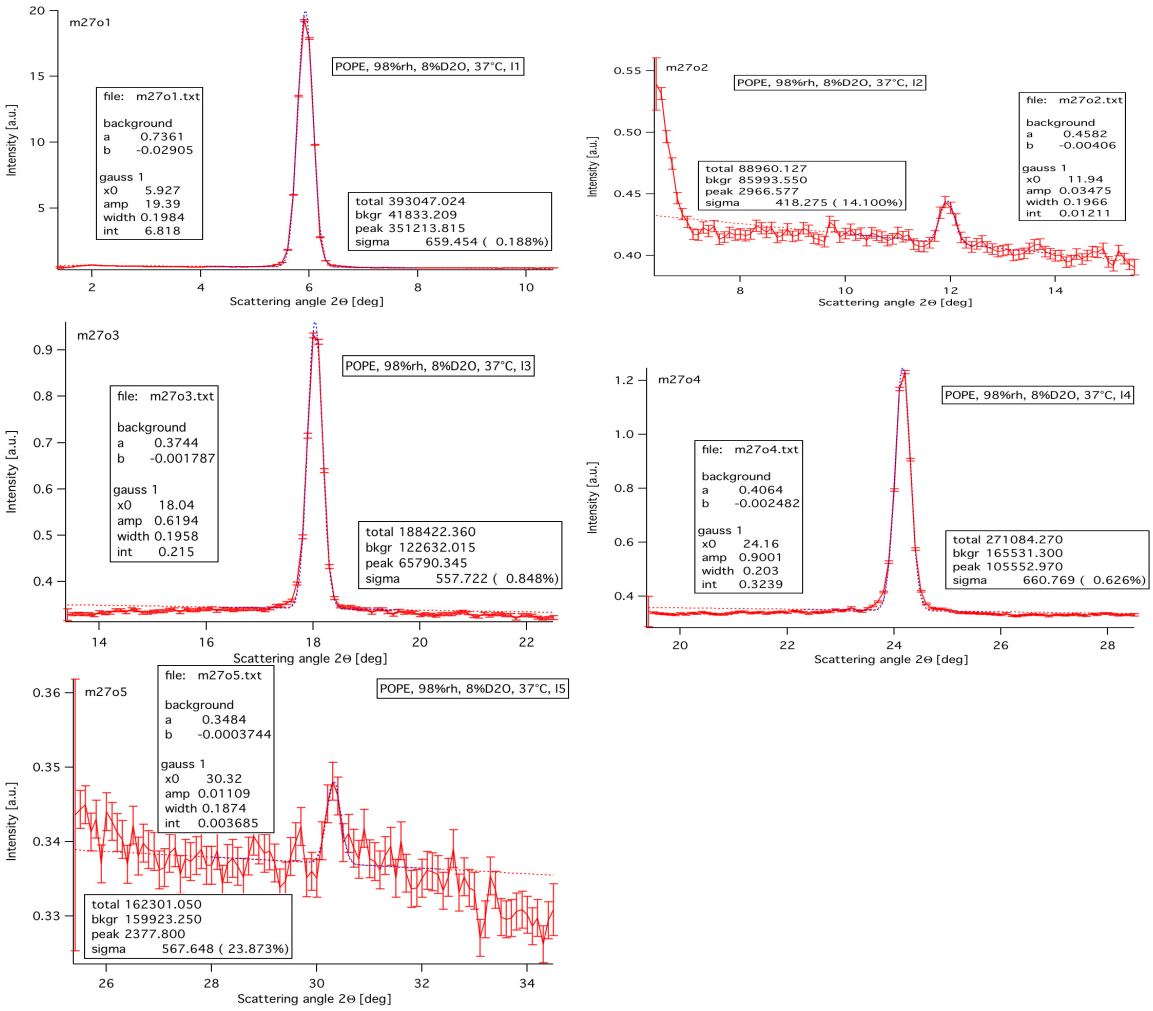

Figure 45. FWHM analysis of the five measured Bragg peaks for POPE multilayer stack measured against D_2O:H_2O – 8%:92% at 37 °C.

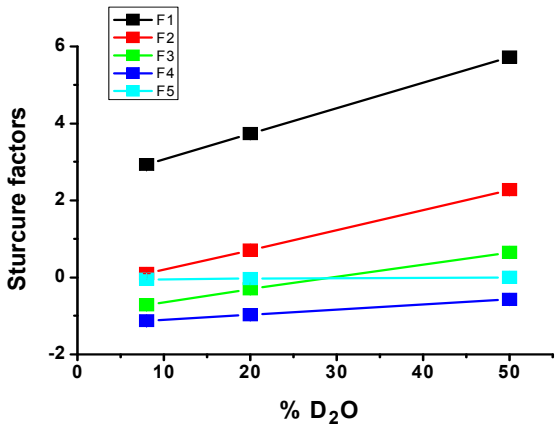

Figure 46. Structure factors of the POPE membrane at 37 °C at different contrasts

The one-dimensional SLD profiles corresponding to the observed structure factors are given in Figure 47. The profiles are symmetric around zero and display the scattering length density with respect to the distance from the center of the POPE bilayer. The two main peaks present in the SLD profiles for the mixture D_2O:H_2O (8%:92%) correspond to the polar lipid-head group. According to Figure 47, the peak's positions are +19.7 Å and -19.7 Å at 20°C and are shifted to +22.7 Å and -22.7 Å, respectively, at 37 °C. The unsaturated bond in the hydrocarbon chains is responsible for the second type of maxima, which are located closer to the center of the bilayer, as shown by Büldt [79]. These maxima are located at positions -6.5 Å and 6.5 Å at both temperatures.

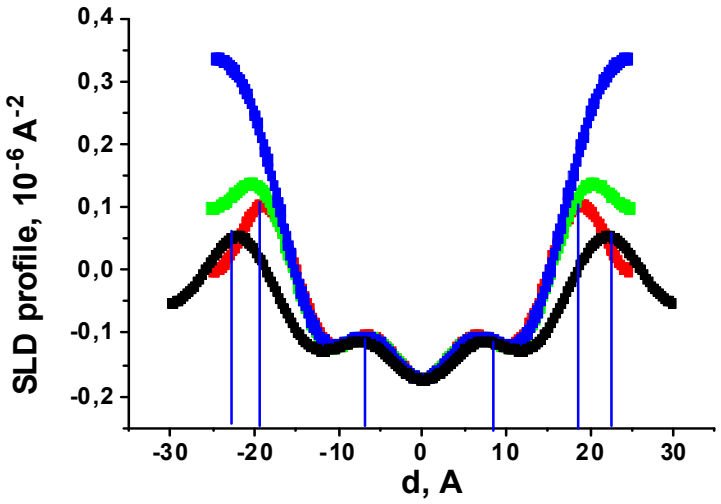

Figure 47. Calculated SLD of the POPE bilayer: 1) the blue curve corresponds to the measurement at 37 °C with D_2O:H_2O mixture (50%:50%); 2) the green curve – 37 °C with D_2O:H_2O (20%:80%); 3) the red – 37 °C, with D_2O:H_2O (8%:92%); 4) the black curve – 20 °C with D_2O:H_2O (8%:92%). The neutron SLD profiles are consistent with the X-ray SLD profile given in the Chapter 3. 2. 1

Table 10. Experimental structure factors

Contrast	F(1)	F(2)	F(3)	F(4)	F(5)
POPE 37 °C					
50% D_2O	5.72±0.05	2.28±0.06	0.64±0.05	-0.57±0.05	-0.05±0.05
20% D_2O	3.73±0.05	0.7±0.06	-0.30±0.05	-0.97±0.05	-0.035±0.05
8% D_2O	2.93±0.05	0.1±0.06	-0.72±0.05	-1.13±0.05	0±0.05
POPE 20 °C					
8% D_2O	2.67±0.04	-0.27±0.06	-0.95±0.05	-1.59±0.05	-0.48±0.08

This experiment enables the evaluation of the amount of water molecules in the heads group of the POPE lipids. The information about the swelled water is derived from the differences in the profiles (see Figure 48).

Because the center of the profiles remains unaffected for all contrasts, the region between the positions -17 Å and 17 Å, where the SLD differences are equal to zero, can be approximated as the alkyl chains. In turn, considering the two border regions, where the SLD differences are non-zero, it can be to concluded that the penetration depth of water into the bilayer is between 7-10 Å. These results strongly support the assumption of penetration of water into the bilayer head group region. This determined value of the penetration depth is in good agreement with the result of McIntosh and Simon. They showed that for the PE polar group, there are approximately 7 and 10 water molecules in the solid and fluid crystalline phases, respectively, with about half of these water molecules in the head group region [80].

This information was later used as a starting point for fitting reflectivity data obtained from direct measurements in water for when the metal surface was used as a wafer for lipid coating.

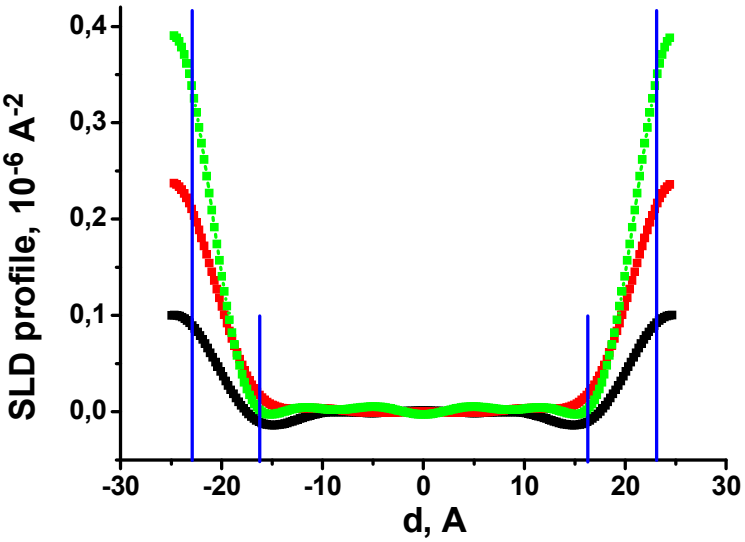

Figure 48. SLD profile differences: 1) the black curve corresponds to the difference between the contrasts D_2O:H_2O (20%:80%) and D_2O:H_2O (8%:92%); 2) the red curve corresponds to the difference between the contrasts D_2O:H_2O (50%:50%) and D_2O:H_2O (20%:80%; 3) the green curve corresponds to the difference between the contrasts H_2O (50%:50%) and D_2O:H_2O (8%:92%)

3. 5. 2. Spray Coating of the Silicon Surface

The X-ray investigation of the POPE spray-coating presented in the Chapter 3. 4 was focused on the structure of the coating in the direction perpendicular to the titanium surface. However, from the X-ray data it was not possible to determine a lateral structure of the spray-coating that is a key parameter to understand the organization of lipids in the thick POPE coating. In order to fill this gap, the Si crystal was used as substrate at the first step of the neutron reflectivity investigation. Such a simplification of the investigated system allowed to perform the simulation of the off-specular reflectivity. The found model of the lateral structure was then applied as a starting point for more complicated case, where POPE lipids were deposited onto Ti coated Si-crystals and where the influences of the protein and of the temperature change was considered in details.

3. 5. 2. 1 Specular Scattering

The spray-coating was very stable in water. The measured reflectivity curve remained constant after 16 hours of exposure in water. One of the curves is presented in Figure 49 as an typical example. The reflectivity at the critical edge does not equal one due to the over-illumination of the sample, and here, the footprint correction must be taken into account as for the X-ray experiment described above. The reflectivity curve in Figure 49 shows a strong Bragg peak at the position corresponding to a bilayer repeat distance of 61 Å, which is evidence for the existence of a multilayer structure on top of the crystals. The rocking scan indicated that the off-specular background for the Bragg peak was rather high as it was only 4 times less than the intensity of the peak (see Figure 53).

As observed in the X-ray measurement, no Kiessig fringes were visible on the curves, and thus, the total number of lipid bilayers in the multilayer structure cannot be precisely determined. However, the “Debye–Scherrer powder method” can be used to estimate the average number of layers because the full width of the Bragg peak at half maximum (FWHM) is related to the number of coherent scattering domains N within the sample [67, 68]. After calculating FWHM and taking into account the resolution of the measurement, the number of coherent scattering domains was determined to be 55-65 bilayers.

The first simulations demonstrated that the most appropriate model includes 50 layers of POPE lipids with scattering length densities which is consisted with the results from Chapter 3. 5. 1 (see Table 11). The simulations of the reflectivity curve were not sensitive to the complicated bilayer model because higher-order Bragg peaks were not measured. Nevertheless, the SLD profile of the POPE bilayer is consistent with the results of the diffraction experiment (see Chapter 3. 5. 1). From the simulations, it was possible to estimate the silicon dioxide layer, which was not visible in the X-ray measurement due to the weak contrast. The silicon dioxide layer was determined to be 35 Å thick and 10 Å rough, with a SLD slightly greater than the theoretical value, most likely due to the presence of D_2O.

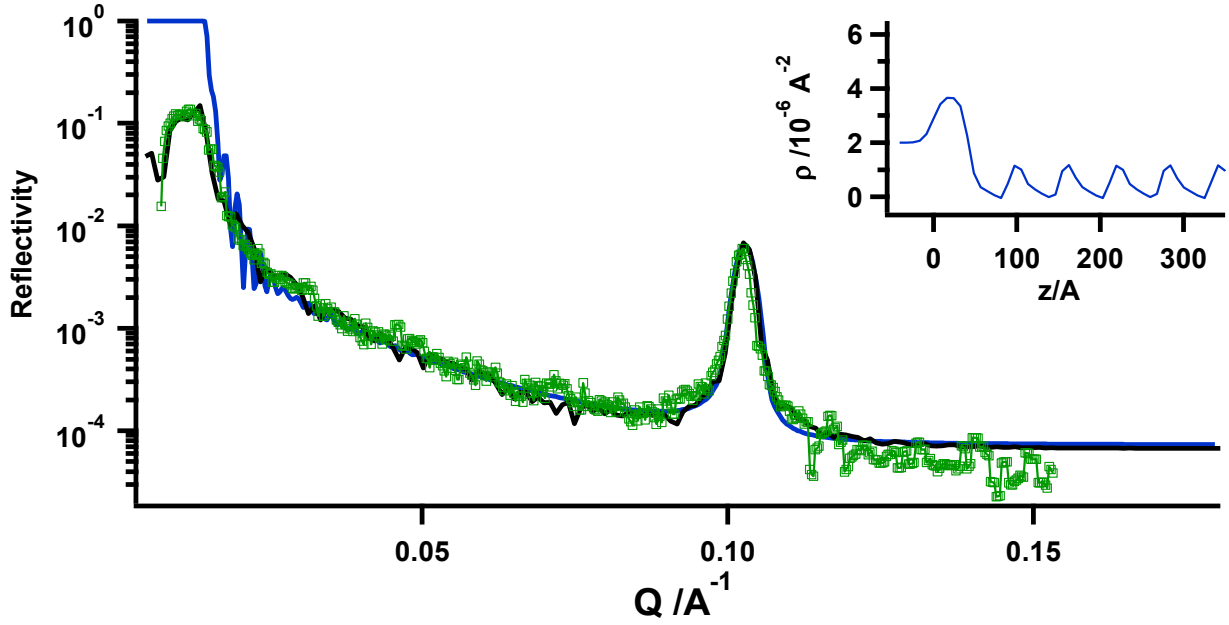

Figure 49. Neutron reflectivity and SLD profiles of the POPE spray-coated silicon crystal: 1) the green dots correspond to the data points; 2) the blue curve corresponds to the model reflectivity curve without the footprint correction; 3) the black curve corresponds to the model curve obtained from the simulated Pi_Pf map, for which the footprint correction was not performed.
In the upper right corner, the SLD profile is presented. The profile is given in the range from -50 Å to 350 Å to enlarge the bilayer profile used in modeling.

The model presented above does not include a thick layer of unstructured lipids, which is required for the analysis of the X-ray data. Nevertheless, SEM demonstrates that such a layer is present on the surface and coats approximately 50% of the surface. According to the reflectivity simulation, adding a thick layer to the profile should lead to the following changes: 1) a reduction in the Kiessig fringes, as shown in Appendix 4; and 2) the reflectivity curve at the critical edge should display a decrease in intensity because the thick coating will absorb part of the beam. Unfortunately, due to the over-illumination of the sample, the information about the

thick coating cannot be obtained. However, considering the off-specular data permits the clarification of some quantitative information about the thick POPE coating.

Table 11. Neutron SLD profile of the spray-coated silicon wafer.

Sample	Material	Thickness, Å	SLD, 10^{-6} Å^{-2}	Roughness, Å
Si+POPE	Silicon	None	2	None
	Silicon dioxide	40±3	3.8±0.5	10±3
	Lipid multilayer structure 50 repetitions			
	Water layer	7±1	2±0.5	6±3
	Head group	5±2	1±0.5	4±2
	Tail group	36.7±3	-0.3±0.5	15±8
	Head group	5±2	1±0.5	4±2
	Water layer	7±1	2±0.5	6±3
	D_2O	None	6.34	100±20

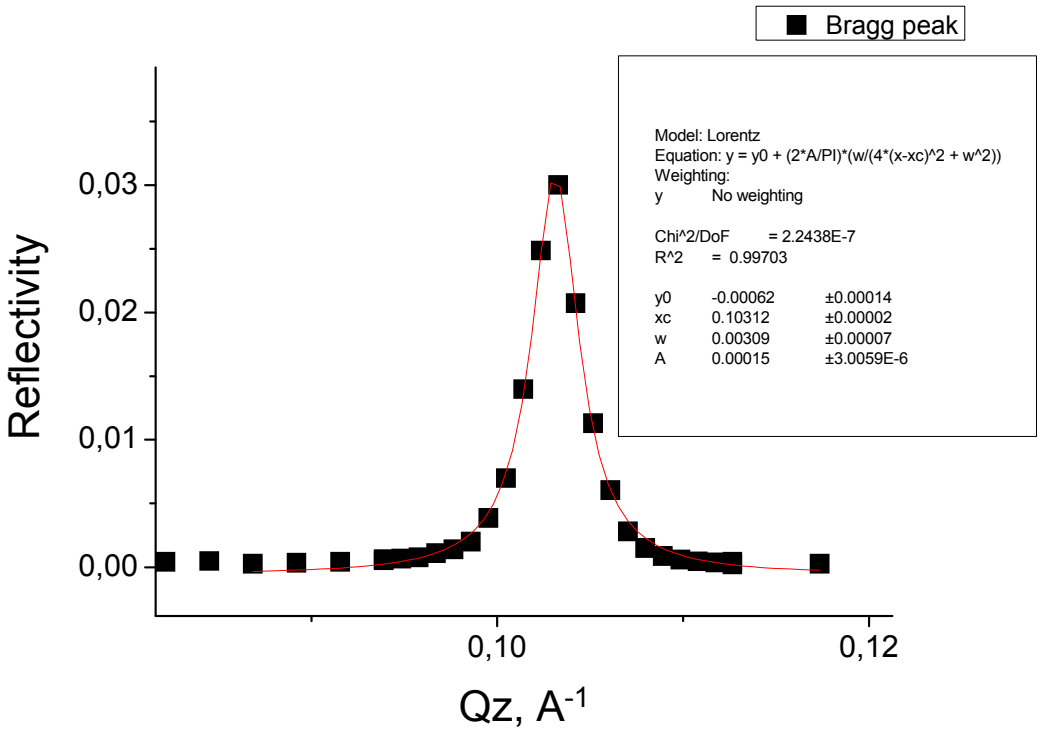

Figure 50. FWHM analysis of the Bragg peak

3. 5. 2. 2 Off-Specular Scattering

As evident from the Alpha_i Alpha_f map presented in Figure 51, where Alpha_i is the incident angle and Alpha_f is the scattered angle, the diffuse scattering is concentrated in the sheet in the reciprocal space. The Bragg sheet is modulated by the standing wave effect whenever the angle of incidence or exit is equal to a Bragg angle 2dsinα=nλ [81]. The fact that there is no edge of the Bragg sheet observed up to the Yoneda wings indicates a high roughness conformation [57] in the multilayer system. A rocking curve measured around the first Bragg peak demonstrates that the off-specular scattering is 4 times less than the intensity of the peak, indicating a high roughness of the layers [82]. For the following data analysis, the Alphai_Alphaf map was converted to a Q_x Q_z map.

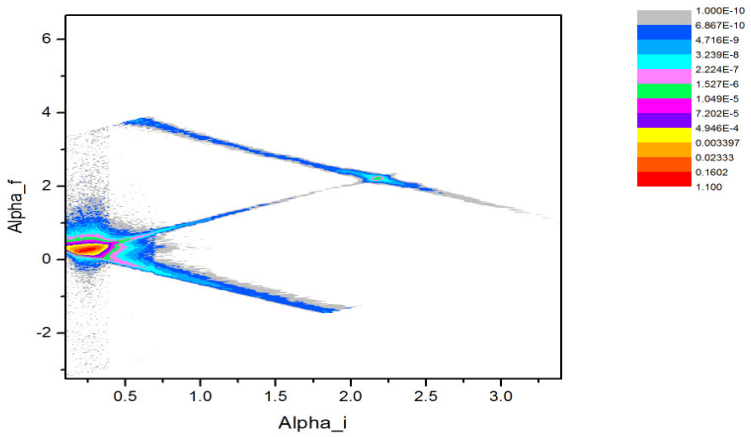

Figure 51. Alpha_i Alpha_f map of the Si crystal covered with POPE vs. D2O

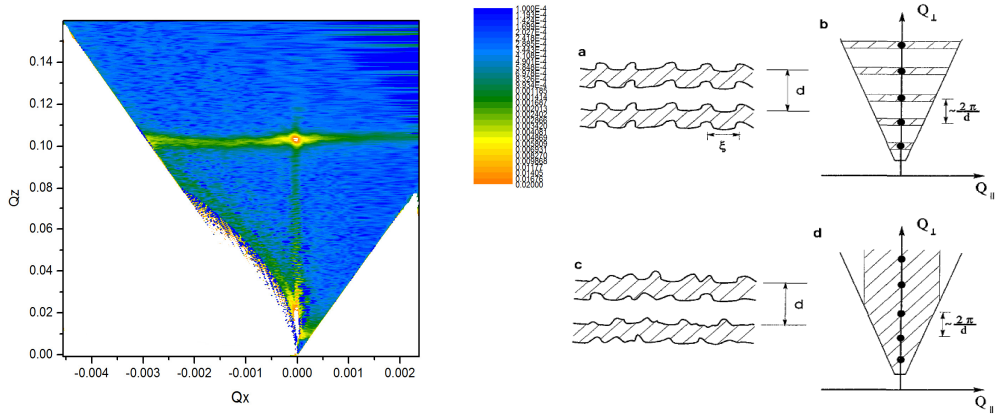

Figure 52. Q_xQ_z map of the Si crystal covered with POPE lipids vs. D_2O

The analysis of the diffuse scattering was started by considering the rocking curve measured at Qz=0.102, which corresponds to the Bragg peak position.

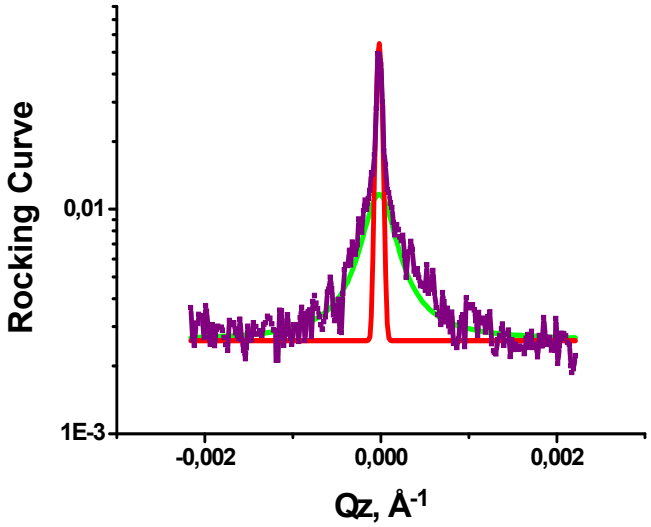

Figure 53. The analysis of the rocking curve

Figure 53 shows that the shape of the curve could be fitted by two peaks: a sharp Gaussian peak (specular scattering) and a broad Lorentz peak (diffuse scattering). The ability to separate specular and diffuse scatterings indicates that the investigated system is a system with a cut-off length: if the length of the in-plane vector r is higher than the correlation length ξ, the surface looks smooth, and when r is smaller than the cut-off length, the surface is rough and diffuse scattering occurs; ξ can be determined by analyzing the Lorentz peak width. According to the value of FWHM, ξ equals 15,700 Å.

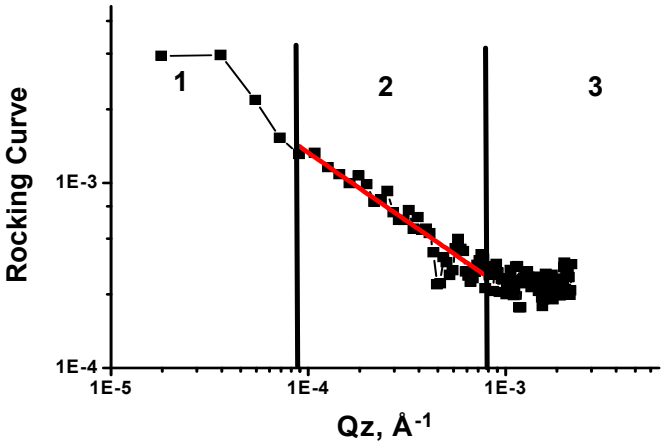

Figure 54. The log-log plot of the rocking curve at Qz=0.102 of the spray-coated silicon crystal. Region 1 corresponds to the Gaussian-like specular reflection. Region 2 is the kinematical region, which is characterized by the power law. Region 3 is the region in which dynamic scattering dominates.

The information about the cross-cross correlation function averaged over every interface of the multilayer structure can be obtained from the decay of the diffuse intensity with Q_x far from the specular region and at constant Q_z. According to the analysis presented in Figure 54, the power law at the position of the first Bragg sheet is $S_{diff}(Q_x) \sim Q_x^{-0.74}$. This behavior indicates a very strong diffuse scattering and cannot be explained in terms of thermal fluctuation theory, which is usually expected for a system of fully hydrated membranes [83]. Thermal fluctuation theory predicts that the slope of the power law region, which is defined as Region 2 in Figure 54, must be slightly less than -2, which is approximately two times larger than the here observed slope. Such a strong diffuse scattering, however, can be expected for free capillary waves, for which the power law can be written as $S_{diff}(Q_x) \sim Q_x^{\frac{k_B T}{2\pi\gamma} Q_z^2 - 1}$. Taking this model into account, it is possible to determine the surface tension, which is calculated to be 1.8 10^{-7} N/m^2.

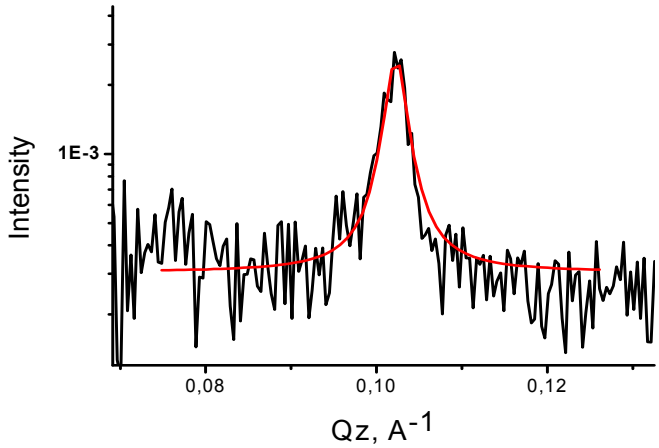

Figure 55. Cut along the Qz axis at Qx=-0.001. The black line corresponds to the experimental data; the red line is the fit by the Lorentz function

Another characteristic of a multilayer structure is the vertical correlation length ξ_z, which, in the general case, is a function of Q_x [82]. To evaluate this parameter, the width of the Bragg sheet must be examined as a function of Q_x. In this particular case, however, no changes in the Bragg sheet width are observed. The FWHM is approximately equal to ΔQ_z=0.003 Å^{-1} for all values of Q_x up to the Yoneda wings. Calculating ξ_z as $2\pi/\Delta Q_z$ shows that it is approximately equal to 2,090 Å. Because ΔQ_z does not change under specular and off-specular conditions, it is possible to

conclude that the solid substrate does not reduce the number of bilayers with correlated roughness and that this number is the same (or very close to) the general number of the bilayers in the system.

In the next step, off-specular scattering data were analyzed quantitatively to obtain information about the in-plane structure, which is cannot be achieved from the SEM and AFM techniques. This analysis was performed in close collaboration with Prof. Boris Toperverg (Ruhr-University Bochum), who provided a code for a DWBA-based simulation program. Pi_Pf maps were simulated by applying an in-plan height-height correlation function within the DWBA theory. It was assumed that that this system was dominated by capillary waves. The Fourier transformation of the height-height correlation function for each interface of the POPE multilayer structure was defined as $\left\langle \left| u\left(Q_x\right)\right|^2 \right\rangle \sim \frac{1}{1+\left(Q_x \xi\right)^2}$. Such a height-height correlation function was considered in detail and successfully used previously to investigate Langmuir-Blodgett films [84]. However, in our case, a bending model was not taken into account. If the bending model is included in the calculation of the height-height correlation function, the FWHM of the simulated Bragg sheet becomes larger at high Q_x, which does not reflect the data presented here.

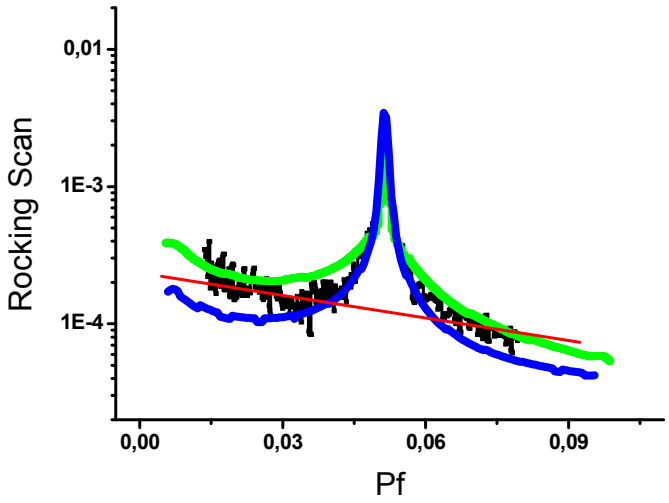

Figure 56. The simulations of the Bragg sheet with the assumption of coherent scattering. 1) The black curve corresponds to the real data; 2) the green curve is the model curve, which corresponds to ξ = 2,000 Å; 3) the blue curve is the model curve, which corresponds to ξ = 50,000 Å. For both simulations, the roughness of all interfaces in the multilayer structure is 3 Å.

The program takes into account the experimental setup parameters, such as the resolution, the illumination angle and the divergence of the incoming and out-going beam, enabling the generation of Pi_Pf maps that are very similar to the

experimental measured maps. At the first stage of the diffuse simulation, the SLD profile obtained from the fit of the specular curve is implemented into the simulation program. The correlation length can then be found by modeling the shape of the Bragg sheet. The simulated Pi_Pf maps are compared with the real data by performing two cuts: the first one is made along the specular ridge, where Pi=Pf, and the second cut corresponds to the Bragg sheet – Pi+Pf=0.1 $Å^{-1}$. There are two main characteristics of the Bragg sheet's shape: the peak intensity in the middle and the intensity distribution on the "shoulders".

The assumption of coherent scattering enables the construction of many different SLD profiles, that satisfy the specular curve are presented in Figure 49. However, none of these curves is useful for the diffuse simulation because the shape of the Bragg sheet is not reproducible. Figure 56 reveals two typical examples of the simulated Bragg sheets with the assumption of coherent scattering:

1) The blue curve in Figure 56 corresponds to a correlation length of ξ = 50000 Å. For such a large value the diffuse scattering is concentrated around the Gaussian-like specular peak, which enables a properly shaped peak in the middle of the Bragg sheet. Nevertheless, the intensity of the "shoulders" is not strong enough and cannot be increased due to the background level because such a high background was not observed in the evaluation of the specular curve.

2) The green curve in Figure 56 represents the case of ξ = 2000 Å. For a shorter correlation length, the diffuse scattering concentrated at high Q_x, and thus the shoulder's intensities are better reproduced, but the peak's width, however, is much broader as it should be.

To obtain a proper correlation between the peak's shape and the intensities of the "shoulders", an incoherent model was developed. As shown in Figure 57 and as observed in the X-ray experiment, the spray-coating leads to two types of coating. The following is assumed: 1) each type of POPE coating contains a specific POPE multilayer structure, and 2) these multilayer structures are characterized by different correlation lengths. For the incoherent model, the specific shape of the Bragg sheet can be obtained as a superposition of two Bragg sheets, the first of which has a strong diffuse peak, while the second contains very intense "shoulders".

Figure 58 reveals the final simulation of the Bragg sheet in frame of the incoherent model:

1) The green curve was obtained for 50 POPE bilayers with a roughness on the order of 2-3 Å for each interface. The corresponding correlation length is 10000 Å.

2) The cyan curve was generated for 50 bilayers with a higher roughness of approximately 10-12 Å for each interface. The correlation length in this case was 200 Å.

3) The pink curve is the superposition of the two simulated Bragg sheets assuming that the first multilayer structure coats 60% of the silicon surface and the second multilayer structure coats 40%.

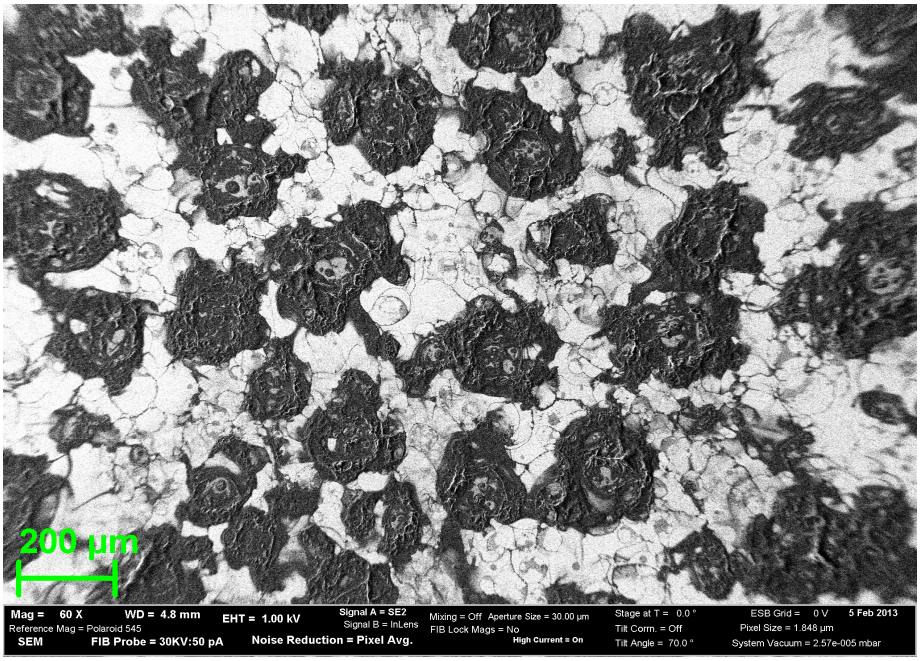

Figure 57. SEM image of the spray-coated silicon crystal

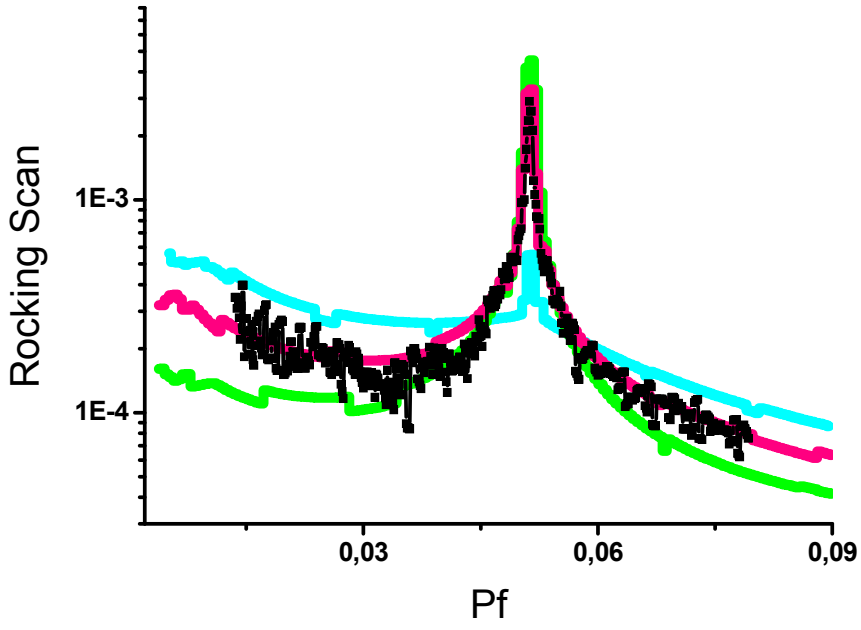

Figure 58. Incoherent modeling of the Bragg sheet

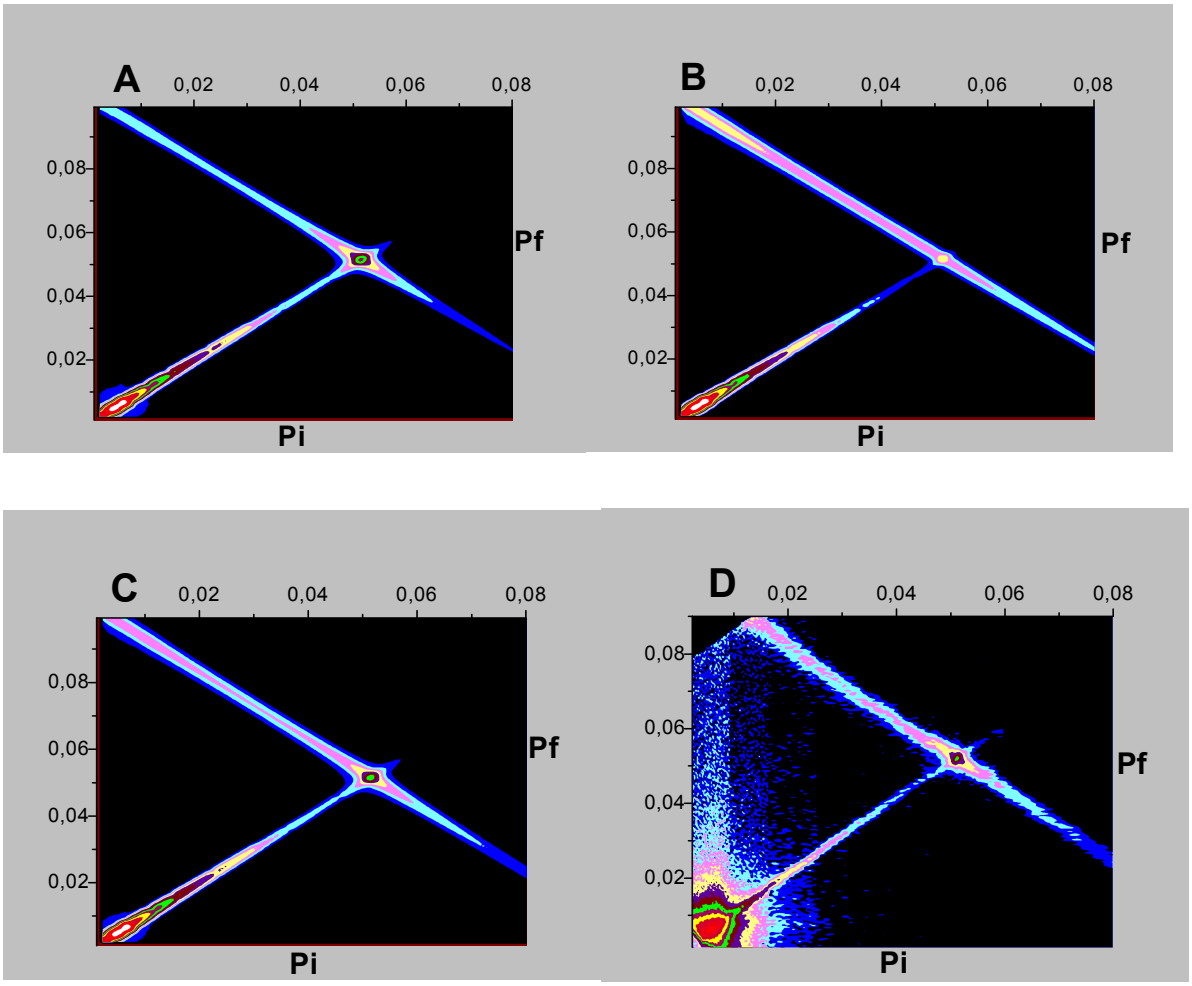

Figure 59. Incoherent modeling of the Pi_Pf map of the spray-coated silicon crystal. 1) Figure A corresponds to the first type of POPE coating, which is characterized by a roughness of 2.5 Å and ξ=40,000 Å; 2) Figure B shows the map generated for the second type of POPE coating (the roughness is 12 Å, ξ=500 Å); 3) Figure C is the superposition of the two previous maps; 4) the measured data are presented in Figure D.

The corresponding Pi_Pf maps are presented in Figure 59. The specular cut of the final Pi_Pf map correctly reproduces the measured specular curve (see Figure 49). One mismatch remains between the final simulated Pi_Pf map and the measured map. There is some intensity at small Pi values in the measured Pi_Pf map; this intensity corresponds to the Yoneda wing. In the simulated map, the Yoneda wing is not visible due to the large value of the illumination angle applied in the simulation. This large illumination angle is needed to obtain the proper intensity at the critical edge (see the model reflectivity curve in Figure 49). However, the illumination angle used in the simulation is higher than that used in the real one, which was defined by the setup of the instrument. This difference indicates that part of the beam was absorbed due to the large amount of POPE lipids on the silicon surface. This

conclusion was confirmed by the ToF reflectivity experiment, which is shown in the following chapter.

This system which contains two types of lipid multilayer structures with different correlation lengths (see Figure 59) has not been reported in the literature. The obtained values of the correlation length are consistent with those reported by other authors; in the context of capillary wave theory, the correlation length of a DPPC bilayer deposited by the Langmuir-Schaefer technique was determined to be 1-11 μm [84]. For a stack of lipid bilayers repeat period of the ripping is approximately 140 Å [85].

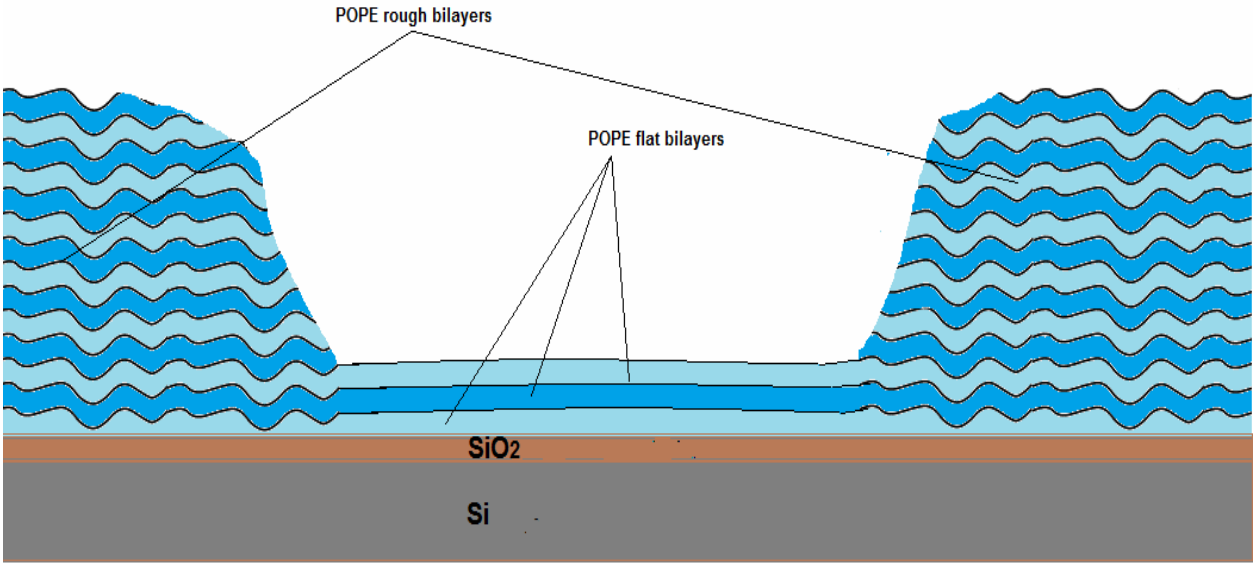

Figure 60. Sketch of the spray-coated silicon crystal

Summarizing this section it is possible to conclude:

1) The neutron reflectivity experiment demonstrated that the POPE coating was stable in water because no changes were observed in the reflectivity curve upon exposure to water.
2) The analysis of the off-specular scattering indicated that the surface was coated by two types of POPE coating. Both coatings are characterized by multilayer structures, although these structures were not identical. The first multilayer structure had very flat bilayers, with a roughness on the order of 2-3 Å and a corresponding correlation length for the first multilayer structure of approximately 10000 Å. The roughness of the second multilayer structure was larger and approximately equal to 10-13 Å. The lateral structure of the second multilayer structure can be represented by a short correlation length on the order of 100-500 Å.

3. 5. 3 Spray Coating of the Titanium Surface

3. 5. 3. 1 Temperature Effect

This part of the work presents the results of the ToF reflectivity experiments. The behavior of the reflectivity curve of the spray-coated sample at the critical edge must be estimated because this region contains the information about the ratio between the two types of POPE coating present on the surface. The investigation of the temperature dependence of the spray coating on the top of the titanium surface is also presented.

The experiment was performed on the ToF reflectometer with a horizontal scattering plane - FIGARO (Fluid Interfaces Grazing Angles ReflectOmeter) at Institute Laue-Langevin in Grenoble.

Based on the measurement of the Ti+spray coated Si-crystal at the lowest incident angle (0.624°) against D_2O, the two critical edges are clearly defined on the reflectivity curve (see Figure 61). The observed decrease in the intensity can be explained by the attenuation of the beam, which passes through the thick POPE coating. Such a decrease has been reported in the literature by Zarbakhch in his neutron reflectivity investigation of 1-2 μm thick oil layers placed in between a silicon crystal and a D_2O interface [86]. In our case, the SEM images demonstrated that there were two types of POPE coating on the titanium surface, and there were two incoherent contributions to the measured reflectivity from each type of coating. In the case of the thin POPE coating, the reflectivity curve had the same critical edge as that for the Ti coated Si-crystal. For the thick POPE coating, the absorption is not negligible, and thus, the reflectivity can be approximated by the formula [87]

$$R(Q_z) = R_1(Q_z) + \frac{(1-R_1(Q_z))^2 R_2(Q_z) A(D)}{1-R_1(Q_z)R_2(Q_z)A(D)} \qquad 26$$

Where $A(D) = Exp\left[-\frac{2*\mathrm{Im}\,SLD*D}{Sin(\theta_{in})}\right]$, $R_1(Q_z)$ is the reflectivity from the TiO_2/lipid interface and $R_2(Q_z)$ is the reflectivity from the lipid/D_2O interface. D is the thickness of the POPE coating, ImSLD is the linear absorption coefficient, and θ_{in} is the incident angle of the beam. From the analysis of the decrease in the intensity at the critical edge, the thickness and the linear absorption coefficient can be evaluated. The calculations revealed that the ImSLD was approximately 1-3 10^{-8} $Å^{-1}$. This ImSLD value is in the range of previously obtained values for thick oil layers [86, 88], the

chemical composition of which contains mostly CH_2, with a density of approximately 0.77 g/mL. The thickness of the thick coating was determined to be approximately 2 ± 1 μm, in good agreement with the SEM results.

The comparison of the reflectivity curves of the Ti coated Si-crystal and the Ti+spray coated crystal (see Figure 61) reveals that the shape of the oscillations from titanium is changed; the position of the oscillation shifts to smaller Q_z values. This shift indicates the attachment of an additional layer to the surface. Moreover, the reflectivity curve of the spray-coated titanium sample contains a beating point at Q_z position 0.035 $Å^{-1}$. From the position of the beating point, it is possible to determine that the thickness of the additional coating is 55-60 Å. This thickness corresponds to the spacing of the POPE bilayer. Finally, it is possible to obtain a proper fit of the oscillations when applied to the POPE bilayer on top of the titanium dioxide layer. This shift and the corresponding beating point were observed independently for the two crystals with different thickness of the titanium layer.

From the simulations, it can to be estimated that POPE lipids deposited on top of a titanium surface are organized slightly differently than those deposited on a silicon crystal. Let us consider some simulations to prove this statement. The violet curve in Figure 61 shows the case of 25 identical POPE bilayers attached to the titanium surface. The SLD profile for the POPE bilayer is taken from the diffraction experiment described in the Section 3. 5. 1. The simulations are very sensitive to the roughness of the last interface. This roughness corresponds to the slope of the curve: if the transition from the last bilayer to D_2O is sharp, the decay of the reflectivity curve does not fit the real reflectivity curve. The rough transition from the multilayer structure to D_2O corresponds to one or two incomplete bilayers on top of the multilayer structure.

Nevertheless, even with a proper general slope of the curve, it is not possible to obtain a beating point in the curve; the oscillations from the titanium are shifted, but the beating point does not appear. Thus, it should be concluded that one bilayer must be separated from the other bilayers. Such a separation of POPE bilayers most likely occurs due to the difference between the in-plane structures. As observed from the experiment with the pure silicon crystal, capillary waves are dominant in the multilayer structure, and an influence of the solid substrate cannot be detected. For the titanium coated crystal used as a substrate, it can be concluded that this influence occurs as a jump from the first attached POPE bilayer to all other bilayers.

For those bilayers, the in-plane structure is defined by thermal capillary waves. Such a scenario is shown in the sketch in Figure 62. The simulation is not really sensitive to the thickness of the transition layer in between the well-attached bilayer and the multilayer structure. The SLD value of the transition layer, however, must correspond to the hydrocarbon region.

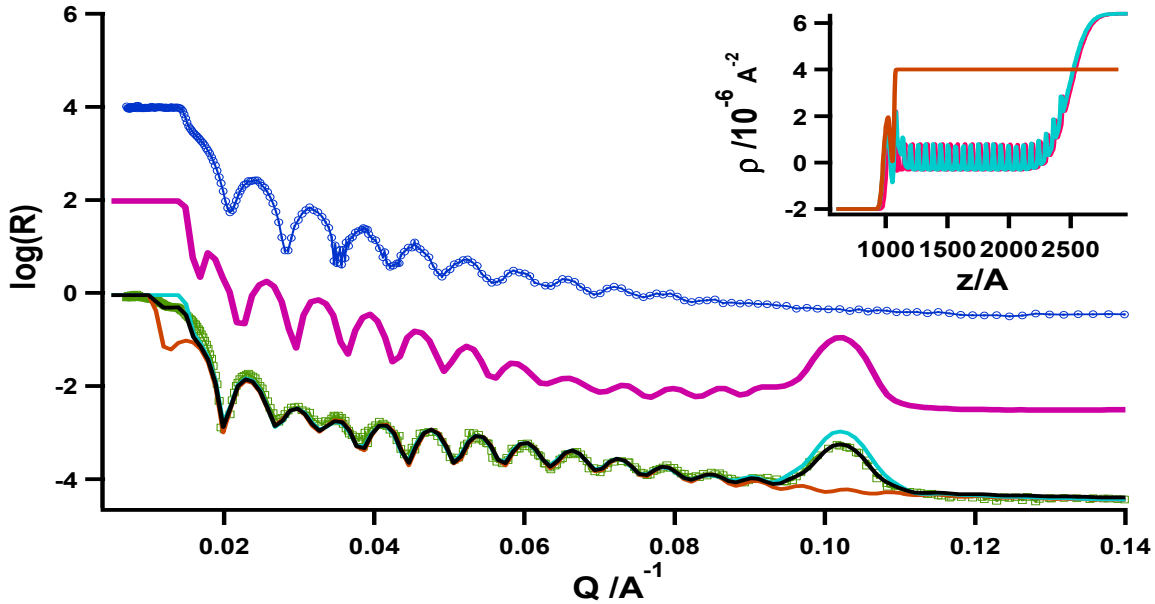

Figure 61. Neutron specular reflectivity curves measured against D_2O. The blue curve corresponds to the Ti coated Si-crystal. The violet curve is the modeled reflectivity curve, which reveals the case of 25 POPE bilayers attached to the Ti coated Si-crystal. The green curve is the real measured curve of the Ti+spray coated Si-crystal at 20 °C. The cyan and orange curves correspond to the modeled specular reflectivity curves of the thin coating and thick coating, respectively. The black curve reveals the final fit within the incoherent model. The corresponding SLD profiles are given in the upper right corner.

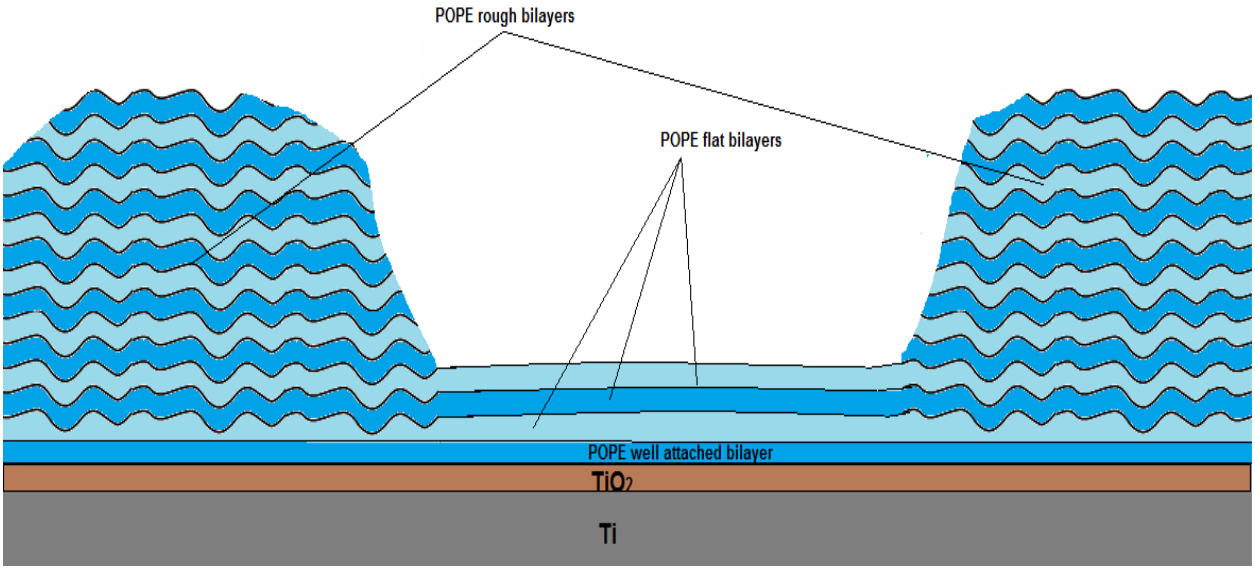

Figure 62. Sketch of the Ti+spray coated Si-crystal.

The final fit is presented in Figure 61 as a superposition of the two model reflectivity curves calculated separately for the two types of POPE coatings.

The temperature behavior of the spray-coated sample was then probed from 20 °C to 42 °C. As shown in Figure 63, the shape and positions of the oscillations remain unaffected for all chosen temperatures, while the Bragg peak shifts to the region of higher Q_z as the temperature increases. At 25 °C, the POPE lipid undergoes a phase transition from the gel phase to the liquid crystalline phase due to the melting of the hydrocarbon region of the bilayers. The effect of the phase transition is evident in the green specular reflectivity curve in Figure 63 as the double Bragg peak, which indicates that both phases are present in the POPE multilayer stack.

Table 12. Neutron SLD profile of the Ti+spray coated Si-crystal at 20 °C.[1]

Sample	Material	Thickness, Å	SLD, 10^{-6} Å^{-2}	Roughness, Å
Ti coated Si-crystal	Si	None	2	None
	SiO_2	40	3.4	8
	Ti	985	-1.96	20
	TiO_2	35	2.4	20
Well attached POPE bilayer	Head region	12	3±0.5	9
	Tail region	37	-0.3±0.5	15
	Head region	12	3±0.5	9
	Transition layer	80±20	-0.3±0.5	80±20
POPE thin coating				
Lipid Multilayer structure 40 repetitions	Water layer	6±2	1.3±1	5±3
	Head group	6±3	0.5±0.5	8±3
	Tail group	36.7±3	-0.3±0.5	15±6
	Head group	6±3	0.5±0.8	10±4
	Water layer	6±2	1.3±1	5±3
POPE thick coating				
Smeared out POPE bilayers	Smeared out POPE bilayers	20000±5000	4±1	8±3

For each applied temperature, the position of the Bragg peak is defined from the fit by a Lorentzian function. Thus, it is possible to obtain the temperature dependence of the POPE d-spacing (see Figure 64). After the phase transition temperature, the d-spacing of the POPE bilayers changes linearly with temperature.

[1]The fitting parameters for the titanium crystal were taken without modification from the analysis of the reflectivity curve measured from the uncoated crystal (for more details, see chapter 5.3).

This linear behavior of the POPE bilayer thickness was previously observed in X-ray diffraction experiment by Rappolt [89]; however, in the diffraction experiment, the POPE multilayer stack was not in contact with liquid, in contrast to our experiment. From the literature [90], it is known that the decrease in the POPE bilayer thickness with increasing temperature is caused by continuous formation of trans-gauche rotamers within the alkyl chains.

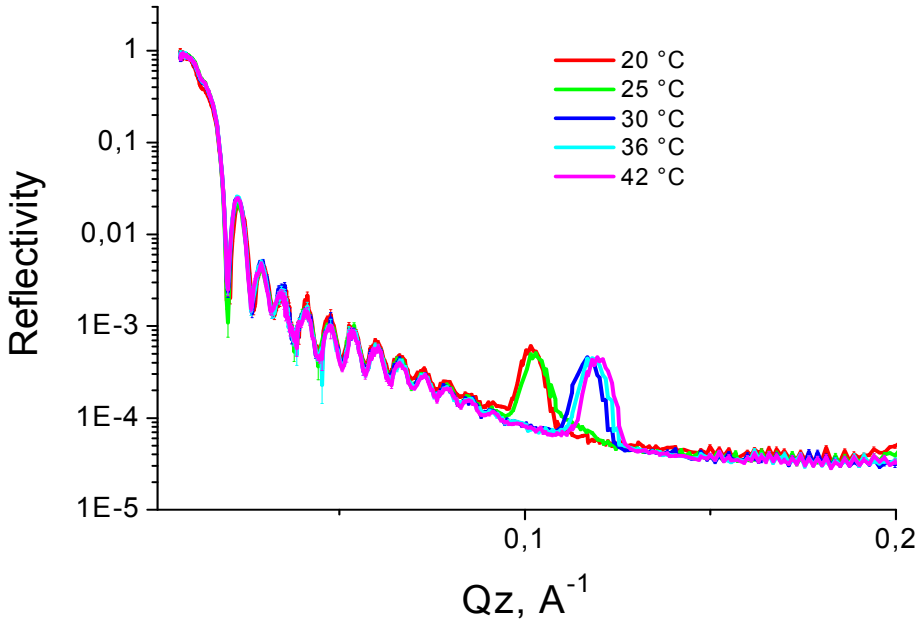

Figure 63. Neutron reflectivity curves – the temperature behavior of POPE bilayers

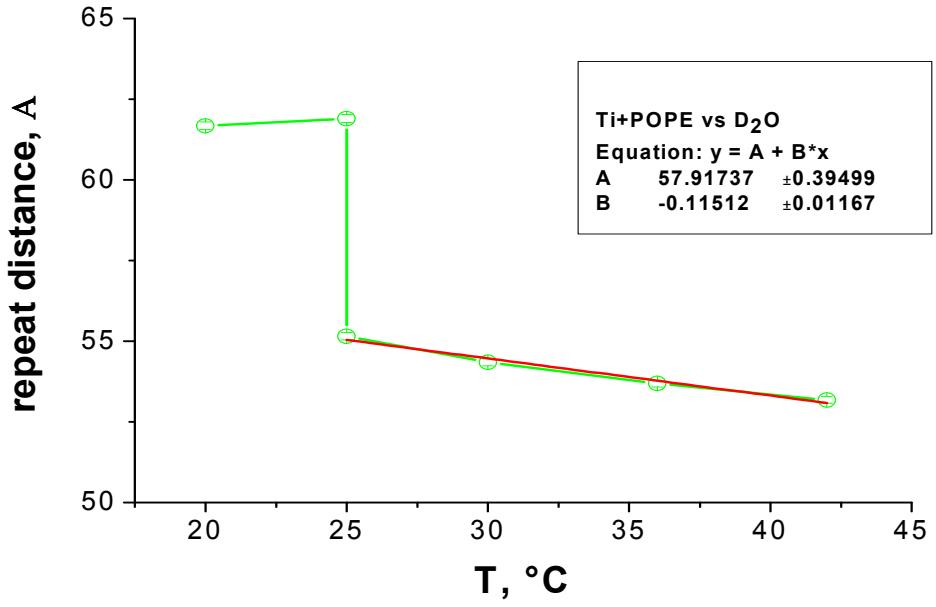

Figure 64. Temperature behavior of the Bragg peak position: 1) Green dots correspond to the d-spacing of the POPE bilayer at different temperatures; 2) The red line – linear fit.

A unique aspect of the POPE lipid is the inter-bilayer interaction, which is clearly different from that of other lipids due to the presence of the PE head group. Lipids with the PE head group do not absorb additional water molecules with increasing temperature, and thus, the thickness of the water layer between the PE bilayers remains constant [90]. The stability of the water layer was confirmed in our neutron experiment because all of the neutron reflectivity curves presented in Figure 63 can be successfully fitted by varying the thickness of the tail group in the box model given in Table 12.

The inter-bilayer interaction is the key parameter of the stability of the POPE spray coating because undulations of the POPE bilayer are suppressed due to the apparently strong inter-bilayer coupling expressed by the small bilayer separation. This is a great advantage of POPE lipids compared to lipids with another type of head group. For example, it is known from the literature that the thickness of the water layer between PC bilayers increases with temperature, and thus, the undulation forces may overwhelm the van der Waals attraction at a certain temperature [91], allowing the PC bilayers to fluctuate freely without correlation to each other. Thus, PC bilayers are not really stable in a liquid environment and are very sensitive to any physical stress.

It can be concluded that POPE may be one of the most appropriate lipids to prepare a mimic coating that is extremely stable with time in a liquid environment in the range of physiological temperatures. The stability of the POPE coating is the result of a strong inter-bilayer interaction that is established from a very high level of inter-bilayer correlation.

3. 5. 3. 2 Effect of Growth Medium and HSA on Spray-Coating of the Titanium Surface

The goal must be investigate the POPE spray coating under conditions that are as similar as possible to those of a real implant. One important issue is the influence of biologically active molecules on the structure of the coating. In this part of the work, the ToF reflectometry investigation of the spray POPE coating in the presence of growth medium and the model protein HSA is presented. HSA was chosen as the model protein because it is water soluble and comprises approximately 50% of blood plasma [92]. HSA is a transport protein and is primarily responsible for the colloidal osmotic pressure of blood. It is important to clarify how the protein intercalates into the multilayer structure since this intercalation appears to be a positive factor in cell growth.

The experiment was performed on the time of flight reflectometer FIGARO (ILL, Grenoble, France). In the first step, the Ti+spray coated Si-crystal was measured against D_2O. This measurement was repeated multiple times. An equilibrium state of the spray coating was observed because the measured reflectivity curve did not change.

The reflectivity curve of the Ti+spray coated Si-crystal (see the green curve in Figure 65) reveals the following features when compared to the curve of the uncoated specimen: 1) a shift in the positions of the oscillations to the region of smaller Q_z; 2) a beating point at the Q_z position 0.035 $Å^{-1}$; 3) a decrease in the intensity at the critical edge; and 4) two Bragg peaks. The analysis indicates that the structure of the spray coating is quite identical to the previously considered multilayer structure in Chapter 3. 5. 3:

1) To interpret the collected data, the case of incoherent scattering from the two types of coatings must be considered. The reflectivity curve from the thick coating, which corresponds to the smeared out POPE bilayers, will yield a decrease in the intensity at the critical edge. The thin coating is expected to include 20-25 flat POPE bilayers, which lead to the appearance of the Bragg peaks.

2) The beating point indicates that one POPE bilayer is well attached to the surface.

The incoherent model, which was previously presented in Table 12, of the thin and thick coatings is correct and remains unaffected for the spray coating on the new titanium specimen. To obtain the final theoretical model, which is presented in Figure

65, the proper parameters for the Ti coated Si-crystal must be inserted in place of the previously used parameters for the Ti coated Si-crystal of the second type (Table 3).

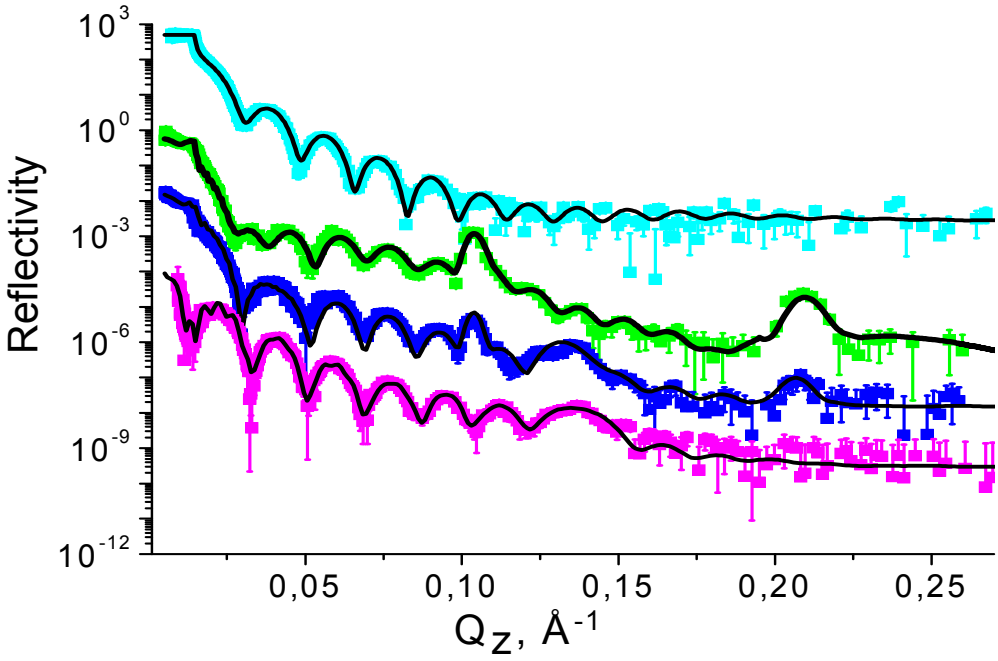

Figure 65. Neutron specular reflectivity curves. The cyan curve corresponds to the Ti coated Si-crystal measured against D_2O. The green curve corresponds to the Ti+spray coated Si-crystal measured against D_2O. The blue curve corresponds to the Ti+spray coated Si-crystal measured against D_2O-based growth medium with deuterated HSA. The violet curve corresponds to the Ti+POPE+dHSA sample against H_2O. The black curves reveal the fits of the measured curves. Some curves are offset vertically for clarity.

D_2O-based growth medium was then injected into the sample cell. The reflectivity curve measured in this case does not show any change compared to the Ti+spray coated Si-crystal measured against pure D_2O. This set of experiments proves that the POPE spray coating is not affected by the mechanical stress due to the exchange of the growth medium.

Interesting experimental features appear after the previously measured spray-coated titanium specimen was exposed to a solution of deuterated HSA in D_2O-based growth medium (hence referred to as Ti+POPE+dHSA). The first feature is that the beating point is no longer observed in the Ti+POPE+dHSA reflectivity curve. This phenomenon is most likely caused by a separation of the first POPE bilayer from the surface, eliminating the transition between the first POPE bilayer and other bilayers in the multilayer structure.

Table 13. Neutron SLD profile of the Ti+spray coated Si-crystal at 20 °C in the presence of dHSA.

Sample	Material	Thickness, Å	SLD, 10^{-6} Å^{-2}	Roughness, Å
Ti coated Si-crystal	Si	None	2	None
	SiO_2	40	3.4	8
	Ti	368	-1.96	13
	TiO_2	25	2.4	15
POPE thin coating – the first multilayer structure				
Lipid Multilayer structure 25 repetitions	Water layer	6±2	1.3±1	5±3
	Head group	6±3	0.5±0.5	8±3
	Tail group	36.7±3	-0.3±0.5	15±6
	Head group	6±3	0.5±0.8	10±4
	Water layer	6±2	1.3±1	5±3
POPE-dHSA complex – the second multilayer structure				
8 repetitions	dHSA	23	4±0.8	7
	POPE lipid	24	2.5±0.8	7
POPE thick coating				
Smeared out POPE bilayers	Smeared out POPE bilayers	20,000±5000	4±1	8±3

Another feature is that the reflectivity curve measured from the Ti+POPE+dHSA sample contains an additional broad Bragg peak, which corresponds to a second multilayer structure of approximately 10-15 repetitions with d-spacing of 45.7 Å (see the blue curve in Figure 65). The origin of the additional Bragg peak, which was reproduced a couple of times for independent sets of experiments with freshly prepared POPE spray coatings, is obviously due to the presence of the protein in the system. Most likely this structure change occurred due to the softness and the flexibility of the POPE multilayer coating in contrast to the OPA-POPE coating, for which any structure change has not been observed (Chapter 3. 3. 2).

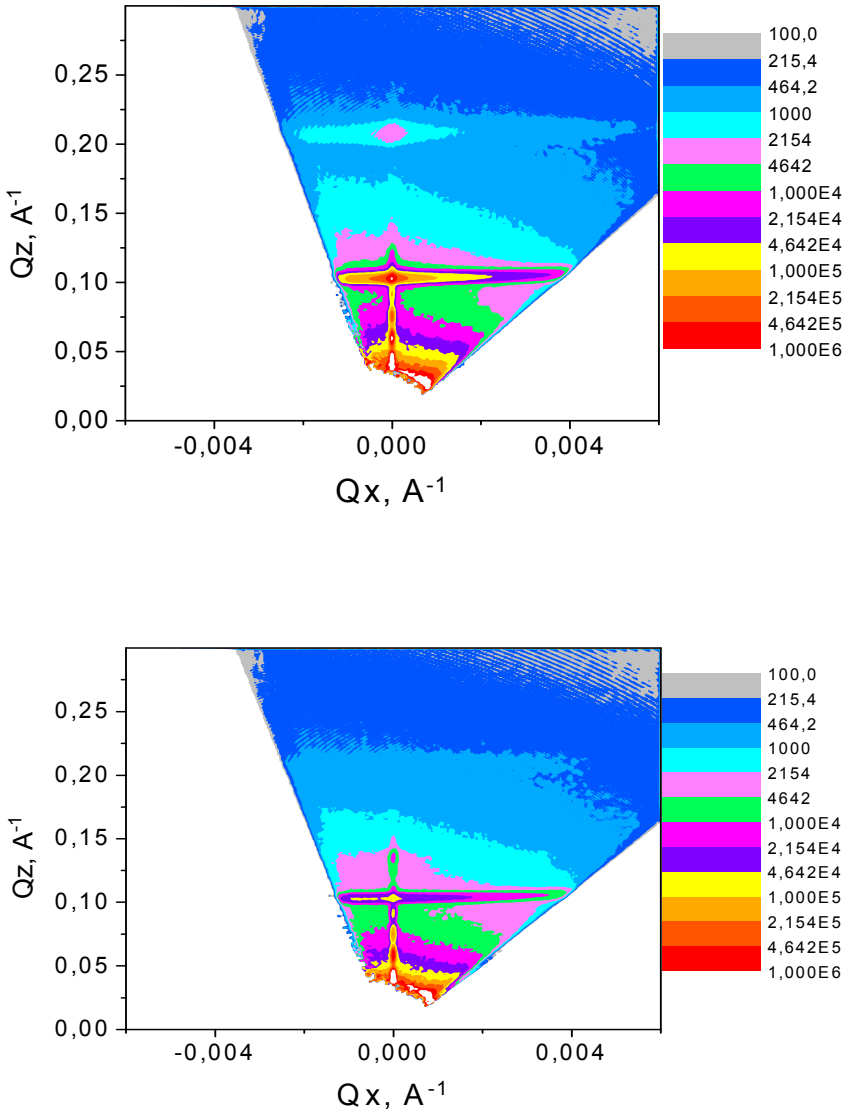

Figure 66. Q maps – POPE lipids on the Ti coated Si-crystal measured in D_2O (A graph) and in D_2O-based growth medium powder with deuterated HSA (B graph).

If a cut along the measured Ti+POPE+dHSA Q-map at the position of the additional Bragg peak Q_z = 0.136 $Å^{-1}$ is considered, it is possible to clarify that the intensity is concentrated in the specular region where Q_x is smaller than $2x10^{-4}$ $Å^{-1}$ and that the off-specular intensity is comparable to the background level, in contrast to the Bragg sheet from the POPE multilayer structure. This shape of the Bragg sheet indicates that the second multilayer structure consists of well-defined layers. This in-plane structure is consistent with the in-plane structure of the thin POPE coating, which could be an indirect indication that the second multilayer structure is related to the thin coating and is located between the islands of the thick coating.

Nevertheless, even after the location and the in-plane structure of the second multilayer structure are assumed, it is not clear which model can explain the Ti+POPE+HSA data. The first assumptions to explain the second multilayer structure involve lipid reorganization due to the tail's incorporation or tilt. Such a reorganization could occur if a part of the POPE lipids are picked up by the protein from the surface, in such a way that the area per molecule of POPE molecules left on the surface increases. This model sounds reasonable because the transport function of lipids is one of the main functions of HSA. In addition, the intensity of the first Bragg peak of the Ti+POPE+HSA reflectivity curve is twice smaller than the intensity of the corresponding Bragg peak before dHSA was added to the sample cell, confirming the proposed POPE reorganization (see Figure 65).

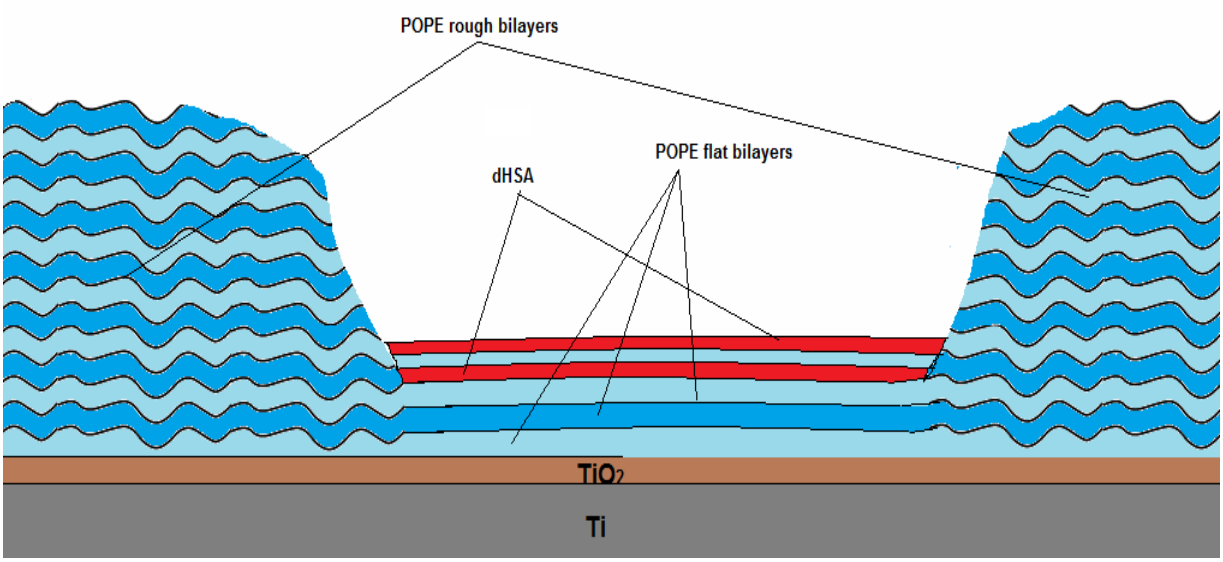

Figure 67. Sketch of the Ti+spray coated Si-crystal in the presence of dHSA.

Based on the simulations, it is possible to postulate that the number of bilayers present prior to the injection of the protein into the sample cell is equal to the sum of the number of bilayers in the first multilayer structure and the second one.

However, this model breaks down after the additional contrast variation experiment in which pure H_2O was injected into the sample cell. The measured reflectivity curve in this case does not contain the Bragg peaks originating from the normal POPE bilayer, as expected due to the weak contrast. However, the additional Bragg peak remains unaffected (see the violet curve in Figure 65), which should not be the case if the origin of the second multilayer structure is lipid reorganization. Therefore, the last measurement vs. H_2O is the direct indication that dHSA is attached to the top of the thin POPE coating (see Figure 67).

Finally, it was possible to fit the Ti+POPE+dHSA reflectivity curve by reducing the number of POPE bilayers from 40 to 25 and by applying the second multilayer structure on the top of the well-defined POPE bilayer (see Figure 65 and Table 13).

The neutron specular (off-specular) results clearly reveal the stability of the POPE spray coating in contact with water due to a strong inter-bilayer interaction that does not break down in the range of physiological temperatures. The strong inter-bilayer interaction and the resulting small inter-bilayer separation are postulated from the very intensive Bragg sheet observed in all measured Q maps. With respect to the stability requirements of a biomimetic implant coating, it can be concluded that POPE may be one of the most appropriate lipids for successful implant modification.

4 Discussion

The aim of this work was to test new deposition techniques on titanium-based implant surfaces and to structurally characterize the coatings to identify which technique is the most appropriate. POPE lipids are known to have a positive impact on cell growth [93]. However, as shown in the present study, the quality of the coating depends on the applied deposition technique. The stability of the coating is a critical parameter, because bone cells can adhere to phospholipid coatings but can be washed away with the underlying phospholipid layer [94]. The second parameter that is important to consider is the completeness of the phospholipid coating; uncoated regions are undesirable.

In a number of studies, lipid coatings on top of a silicon surface have been probed [66], which has an advantage for the reflectivity technique due to a small roughness in order 5 Å. This classical experiment is useful for determining the structure of a lipid bilayer. There are two classical deposition techniques described in the literature. The first is simple adhesion with an organic solvent, which is acceptable for silicon surfaces. However, as shown in section 3. 2. 2, methanol and chloroform are not adhesive liquids for titanium surfaces. Consequently, POPE lipids cannot ultimately distribute on these surfaces, and most of the surface is not coated. This outcome is not acceptable for implant technology, for which it is necessary that the whole implant surface be coated with lipids. The second classical deposition technique is spin coating [95]. Performing this type of coating is difficult for real implants that have a complicated design.

In this work, a few methods to improve the quality of a POPE coating were considered in detail. The first was to use T6Al7Nb as a material for implant production. The resulting change in the surface chemistry leads to a similar POPE coating after drop deposition as occurs when a pure silicon surface is used. X-ray experiments prove that the POPE multilayer structure containing 25-30 POPE bilayers coats the whole surface and remains unaffected after exposition in water. Thus, the first conclusion is that the combination of T6Al7Nb alloy and POPE drop coating is a prospective method for implant development.

The second method uses a pure titanium surface. It involves a controlled method of lipid deposition, which includes chemical pre-coating with OPA followed by Langmuir-Blodgett and Langmuir-Schafer deposition. X-ray and neutron reflectivity experiments show the presence of a well-ordered monolayer of OPA forming on the

titanium surfaces after the OPA deposition procedure. Self-assembled OPA layer thickness of 24 Å and roughness of 8 Å are in agreement with previously studies of OPA monolayers on the mike surface. The high quality of the coating was confirmed independently by X-ray and neutron specular reflectivity techniques. The unwanted cracks detected in the SEM experiment should not occur in real implants made completely from metal, because the cracks are caused by differences in the thermal expansion coefficients of silicon and titanium. The OPA+POPE+2xPOPE coating was examined at the solid/liquid interface in a neutron reflectivity experiment. The analysis of the neutron data clearly revealed that Langmuir-Blodgett deposition of POPE lipids on top of the modified titanium surface leads to a POPE monolayer that coats 65% of the surface. Our data analysis also demonstrates that an additional, free-floating POPE bilayer coats approximately 45% of the surface. The free-floating POPE bilayer was not stable in an aqueous solution containing human serum albumin; however, the hybrid OPA-POPE bilayer was unaffected, leading to a positive result. It can be concluded that the OPA pre-coating improves the stability of the POPE coating significantly because unsaturated hydrocarbon chains of POPE lipids generally lead to the formation of an unstable bilayer that is not easy to handle when applying the Langmuir-Blodgett technique. Thus, the presence of a POPE coating surrounding a real implant material under wet conditions is important with respect to the biomimetic requirements of implant surfaces.

The third deposition technique considered in this study was spray coating, which has the following advantages compared to the control deposition method: 1) easier to handle and 2) fully coats the surface with lipids. Conversely, spray coating leads to smeared lipid bilayers that potentially could lead to coating instability under wet conditions. Therefore, it has been considered a poor prospective deposition method in the literature [95], however, so far POPE lipids have not been deposited by the spray coating technique. AFM and SEM measurements indicated that the POPE spray coating led to two types of surface coatings. The first type contained 45-55 macroscopically flat POPE bilayers that coated approximately 60% of the titanium surface. The second coating was a bulk system that was 1-2 µm thick and coated up to 40% of the surface.

The crucial question here is whether the POPE bilayers on top of the coating are stable. This question might be difficult to answer by applying direct methods of investigation such as AFM and SEM, because in the case of a thick POPE coating,

some lipids remain even after the top bilayer is lost. Nevertheless, the reflectivity experiment allows the total amount of POPE on the surface to be monitored due to a drop in the intensity at the critical edge of the measured reflectivity curve, because there is a straightforward correlation between the thickness of the coating and the absorbed part of the beam. The X-ray and neutron reflectivity experiments clearly proved that exposure to water affects the coating by changing the lateral structure only – the quantity of deposited POPE lipids remains constant even under wet conditions. This result indicates that the spray-coating method satisfies all the requirements for an implant modification technique, including stability and completeness.

The neutron reflectivity experiment showed that the d-spacing of the POPE bilayer decays linearly with temperature after the phase transition temperature. This result is in agreement with the previous X-ray diffraction experiment of Rappolt [89]; however, in contrast to our experiment, the POPE multilayer stack was not in contact with liquid in the diffraction experiment. It is known that such linear behavior indicates that the POPE bilayer thickness changes are caused only by melting of the hydrocarbon region [91]. Our simulations revealed that the neutron data for different temperatures can be successfully fitted only by varying the thickness of the tail group. The fact that POPE bilayers do not absorb additional water molecules as temperature increases when applied as an implant modification is a great advantage of POPE lipids compared to lipids with other types of head groups. For example, the thickness of the water layer between PC bilayers increases with temperature. Thus, the undulation forces may overwhelm the van der Waals attraction at a certain temperature [91], allowing the PC bilayers to fluctuate freely without correlation to each other. Therefore, PC bilayers are not really stable in a liquid environment and are very sensitive to any physical stress.

Off-specular scattering analysis indicated that both coatings were characterized by multilayer structures, although these structures were not identical. The first multilayer structure had very flat bilayers with roughness on the order of 2-3 Å and a corresponding correlation length for the first multilayer structure of approximately 10,000 Å. The roughness of the second multilayer structure was larger and approximately equal to 10-13 Å. The lateral structure of the second multilayer structure can be represented by a short correlation length on the order of 100-500 Å. The main significance of the off-specular data is that the interbilayer interaction does

not break down and the whole POPE multilayer system fluctuates as one unit independently from the level of POPE bilayer alignment and from the number of POPE bilayers. Such a high level of the POPE bilayer organization, which cannot be detected by any other technique except scattering reflectivity, minimizes the possibility that the top bilayer of the multilayer structure is lost even when a high number of bilayers are present, in contrast to lipids with a PC head group.

POPE may be one of the most appropriate lipids for the preparation of a mimic coating that is extremely stable over time in a liquid environment and within the physiological temperature range. The stability of the POPE coating is the result of strong interbilayer interactions that are established through a very high level of interbilayer correlation.

Given the results of the present study, I conclude that the success of the POPE coating completely depends on how lipids eventually become distributed over an implant surface. Once POPE lipids are attached to the surface, they remain on it under wet conditions until a special treatment with organic solvents is performed. Such a coating was stable under gentle mechanical stress, as shown by neutron experiments in which water flow during contrast exchange in a sample cell did not affect the POPE coating. However, during a real surgery, mechanical contact with a coated surface is inescapable and represents a significant challenge for a mimetic coating. The solution could be to use porous titanium materials. The pores serve the following two purposes: 1) to be a “lipid catcher” as schematically shown in Figure 68, which concentrates lipids inside titanium pores after solvent evaporation and leads to a more eventually distribution of POPE lipids than a polished titanium surface and 2) to save the lipids inside from direct mechanical contact.

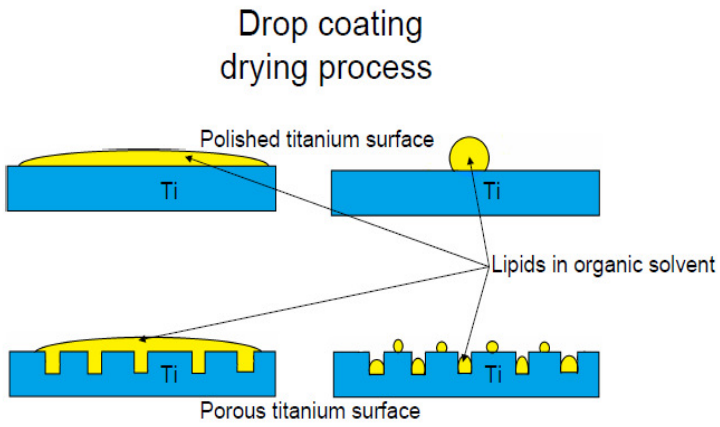

Figure 68. Drop coating of a polished titanium surface and a porous titanium surface.

Direct stability control of the POPE coating inside pores might be an extremely hard task, because even the scattering technique fails due to the macroscopic roughness of a metal surface. However, according to our off-specular investigation, it is possible to estimate that the POPE structure inside pores would be similar to the structure of the thick POPE coating that is stable in a liquid environment due to a high level of correlation despite the POPE bilayers being poorly aligned. The combination of porous titanium-POPE drop coating might stimulate cell “ingrowth” into porous metallic implant material, as has already been reported by Regine Willumeit et al. [96] for porous Ti6Al4V material.

5 Conclusions

In this work, structural analysis of biomimetic implant coatings is performed using a combination of X-ray and neutron specular (off-specular) techniques to identify the most relevant method of lipid deposition:

1) It is shown that the controlled deposition promotes a OPA-POPE bilayer which coats 65% of the surface and remains stable under wet condition and mechanical stress. At the same time the additional free-floating POPE bilayer is not stable in an aqueous solution. It can be concluded that the OPA pre-coating improves the stability of the POPE monolayer due to the additional van der Waals interaction between the OPA monolayer and POPE. However, the requirement of the completeness of the coating is not satisfied entirely.

2) The spray deposition leads to two types of surface coatings: a) the first coating contained 45-55 macroscopically flat POPE bilayers that coats approximately 60% of the titanium surface; b) the second coating is a bulk system that is 1-2 μm thick and coats up to 40% of the surface. The analysis of the off-specular data proves the extremely high level of bilayer organization, even for a 1-2 μm POPE coating under wet conditions and at physiological temperature. Thus, POPE may be one of the most appropriate lipids for preparing a biomimetic coating due to a strong interbilayer interaction and a high level of interbilayer correlation. Our results indicate that the spray-coating method satisfies all the requirements for an implant modification technique, including stability and completeness.

A deep understanding of the structure of the POPE multilayer stack promotes the success of the biological cell experiment with titanium-based porous materials drop-coated by POPE lipids. The main conclusion is that the combination of porous titanium and POPE drop (as well as spray) coating might be the most promising methods of implant modification due to 1) the eventual distribution of the POPE lipids over a titanium surface, 2) the stability of the coating under wet conditions and 3) the possible reduction of stress from mechanical contact with the POPE-coated surface.

This is the first time that a biologically relevant surface on a model implant has been described by X-ray and neutron reflectometry techniques.

Acknowledgments

First of all, I would like to express the deepest appreciation to my supervisors: Prof. Andreas Schreyer and Prof. Regine Willumeit, who gave me the opportunity to write this work and helped me complete it successfully.

My special thanks are given to Dr. Dieter Lott and Dr. Vasyl Haramus, who followed me in my experiments and supported my data analysis. Furthermore, I wish to thank all of the individuals from HZG, DESY, FRM 2, and ILL who were involved in this project.

Finally, I would like to thank my family for their love and faith in me.

Bibliography

1. Bosco R., et al., *Surface Engineering for Bon Implants: A Trend from Passive to Active Surfaces.* Coatings, 2012. 2: p. 95-119.
2. Zethraeus N.,et al., *Cost-effectiveness of the treatment and prevention of osteoporosis.* Oseoposros. Int., 2007. 18: p. 2-23.
3. Roach H. I., et al., *Pathobiology of asteoarthritis: pathomechanisms and potential therapeutic targets.* Current Drug Targets, 2007. 8(2): p. 271-282.
4. Barrere F., et al., *Advanced biomaterials for skeletal tissues regeneration: Instructive and smart functions.* Mater. Sci. Eng. Rep., 2008. 59: p. 38-71.
5. Williams D.F., et al., *On the mechanism of biocompatibility.* Biomaterials, 2008. 29: p. 2941-2953.
6. Tengvall P., et al., *Physico-chemical consideration of titanium as biomaterial.* Clin. Mater, 1992. 9: p. 115-134.
7. Willumeit R., et al., J. Mater. Sci: Mater. Med., 2007. 18: p. 367-380.
8. Willumeit R., et al., *European Cells and Materials.* 13, 2007: p. 11-25.
9. *Phosphatidylethanolamine*. 2012 11 November 2012 at 21:09; Available from: http://en.wikipedia.org/wiki/Phosphatidylethanolamine.
10. Wellner N., et al., *N-acylation of phosphatidetethanolamine and its biological function in mammals.* Biochim Biophys Acta., 2012. 12: p. 1388-1981.
11. Willumeit R., et al., *Biological Multi-layer Systems as Implant Surface Modification.* Materialwissensschaft und Werkstofftechnik, 2004. 34(12): p. 1084-1093.
12. avanty.com.
13. Rand R., et al., *Hydration Forces Between Phospholipid Bilayers.* Biochim. Biophys. Acta, 1989. 988: p. 351-376.
14. Carter D. C., et al., *Three-Dimension Structure of Human Serum Albumin.* Science, 1989. 244
15. Liebmann-Vinson A., et al., *A Neutron Reflectometry Study of Human Serum Albumin Adsorption in Situ.* Langmuir, 1996. 12: p. 2256-2262.
16. *HUMAN SERUM ALBUMIN COMPLEXED WITH MYRISTATE AND AZAPROPAZONE*. 2013; Available from: http://www.rcsb.org/pdb/explore.do?structureId=2BXI.

17. *Human Serum Albumin*. 2013; Available from: http://en.wikipedia.org/wiki/Human_serum_albumin.
18. Gao W., et al., *Self-Assembled Monolayers of Alkylphosphonic Acids on Metal Oxides.* Langmuir, 1996. 12(26): p. 6429-6435.
19. Fabre R. M., et al., Stable Supported Lipid Bilayers on Zirconium Phosphonate Surfaces. Langmuir, 2009. 25(21): p. 12644-12652.
20. Salditt T., et al., *Thermal Fluctuation and Stability of Solid-Supported Lipid Membranes.* Journal of Physics: Condensed Matter, 2005. 17: p. 287-314.
21. Russel R.T., *On the Reflectivity of Polymers: Neutrons and X-rays.* Physica B: Condensed Matter, 1996. 221(1-4): p. 267-283.
22. Zabel H., *X-ray and Neutron Reflectivity Analysis of Thin Flms and Superlattices.* Appl. Phys. A, 1994. 58: p. 159-168.
23. Petrash S.. et al., *Neurtron and X-ray REflectivity Studies of Human Serum Albumin Adsorption onto Functionalized Surfaces of Self-Assembled Monolayers.* Biotechnol. Prog., 1997. 13: p. 635-639.
24. *Profile Coating Technology*. Available from: http://www.hzg.de/institute/materials_research/structure/materials_technology/nano/coating_technology/index.html.en.
25. Gawalt E. S., et al., *Self-Assembly and Bonding of Alkanephosphonic Acids on the Native OXide Surface of Titanium.* Langmuir, 2001. 12: p. 5736-5738.
26. NIMA, K. *Lanmuir and Langmuir-Blodgett Troughs*. 2013; Available from: http://www.ksvnima.com/langmuir-and-langmuir-blodgett-troughs?_kk=langmuir%20blodgett%20trough&_kt=a3e5987e-a2e1-4647-85c0-b4b1369fe61d&gclid=CPr1xIGU3rQCFY65zAod8WoAQw.
27. Girard-Egrot A. P., et al., *Langmuir-Blodgett Technique for Synthesis of Biomimetic Lipid Membranes*.
28. Ma G., et al., *DPPC Langmuir monolayer at the air-water interface: probing the tail and head groups by vibrational sum frequency generation spectroscopy.* Langmuir, 2006. 22(12): p. 5341-9.
29. Quinn, P.J., et al., *The liquid-ordered phase in membranes.* Biochim Biophys Acta, 2009. 1788(1): p. 33-46.
30. foi.se/surfbiotech/tt/Films.htm.
31. http://en.wikipedia.org/wiki/Atomic_force_microscopy.
32. *XE-100*. 2013; Available from: http://www.parkafm.com/product/product_view.php?gubun=R&id=2&product_name=XE-100.
33. *X-Ray Diffractometer for the Analysis of Phases, Residual Stress, and Texture, as well as Reflectometry*. Available from: http://www.hzg.de/central_departments/genf/instruments/003331/index_0003331.html.en.
34. http;//www.ncnr.nist.gov/reflpak/reflpak/html/reflred/footprint_correction.html.
35. Daillant J., et al., *X-Ray and Neutron Reflectivity: Principles and Applications.* Lecture Notes in Physics: N.s. M, Monographs, 1999. 58.
36. Salditt T., et al., Europhys. J. E, 2002. 7(105): p. 7105.
37. http://www.helmholtz-berlin.de/pubbin/igama_output?modus=einzel&sprache=en&gid=1704&typoid=39942#seitenanfang.
38. Dante S., et al., *Beta-amyloid 25 to 35 in intercalated in anionic and zwitterionic lipid membranes to different extents.* Biophysical Journal, 2002. 83(5): p. 2610-2616.

39. Dante S., et al., *Insertion of externally administered amyloid beta peptide 25-35 and perturbation of lipid bilayers.* Biophysical Journal, 2003. 42(46): p. 13667-13672.
40. http://www.helmholtz-berlin.de/media/media/grossgeraete/nutzerdienst/neutronen/instrumente/inst/bensc_v1.pdf.
41. Kreuzer M., Solid-Supported Lipid Membranes and Their Response to Varied Environmental Conditions. Dissertation, 2011.
42. Campbell R. A., et al., *The New Horizontal Neutron Reflectometer at the ILL.* The European Physical Journal Plus, 2011. 126(107).
43. Ott F., et. al., *Off-Specular Data Representations in Neutron Reflectivity.* Jornal of Applied Crystallography, 2011. 44: p. 359-369.
44. Holden D.A., et. al., *Resistive-pulse detection of multilamellar liposomes.* Langmuir, 2012. 28(19): p. 7572-7.
45. Zhai Y., et al., *Physical properties of archaeal tetraether lipid membranes as revealed by differential scanning and pressure perturbation calorimetry, molecular acoustics, and neutron reflectometry: effects of pressure and cell growth temperature.* Langmuir, 2012. 28(11): p. 5211-7.
46. Tolan, M., *X-Ray Scattering Form Soft-Matter Thin Film.* Springer-Verlag, Gerlin Heidelberg, 1999.
47. Dianoux A-J., *Neutron Data Booklet.* ILL 2nd edition, 2003.
48. J. Fitter, T.G., J Katsaras, *Neutron Scattering in Biology.* 2005.
49. Daillant J., et al., *X-ray and Neutron Reflectivity: Principles and Applications.* Lecture Notes in Physisc. Vol. 58. 1999.
50. Constantin D., et al., *Solid-supported lipid multilayers: structure factor and fluctuations.* Eur Phys J E Soft Matter, 2003. 12(2): p. 283-90.
51. Majkrzak C., et al., *In Magnetic Multilayers.* World Scientific, 1994: p. 299.
52. Fitter J., et al., *Neutron Scattering in Biology*. 2006: Springer.
53. Katsaras J., et al., *X-Ray Diffraction Studies of Oriented Lipid Bilayers.* Biochem. Cell Biol., 1995. 73: p. 209-218.
54. Katsaras J., Adsorbed to a Rigid substrate, *Dimyristoylphosphatidylcholine Multibilayers Attain Full Hydration in all Mesophases.* Biophys J, 1998, 75(5); p. 2157-62
55. Servantes M. E., *A Study of Supported Lipid Multilayers in a Humidity-Controlled Environment*. 2011, Northern Illinois University. p. 45.
56. Petrache H.I., et al., *Fluid phase structure of EPC and DMPC bilayers.* Chem Phys Lipids, 1998. 95(1): p. 83-94.
57. Zabel H., *X-Ray and Neutron Reflectivity Analysis of Thin Films and Superlattices.* Applied Physics A, 1994. 58: p. 159-168.
58. Sinha S. K., et al., *X-ray and Neutron Scattering from rough Surfaces.* Physical Review B, August 1988. 38(4).
59. Schlomka J. P., et al., Phys. Rev. B, 1995. 51(4).
60. Jablin M. S., et al., *In-Plane Correlations in a Polymer-Supported Lipid Membrane Measured Be Off-Specular Neutron Scattering.* Physical Review Letters, 2001. 106.
61. Yano Y. F., et al., *Simultaneous Measurement of X-Ray Specular Reflection and Off-Specular Diffuse Scattering from Liquid Surfaces using a Two-Dimention Pixel Array Detector: the Liquid-Interface Reflectometer of BL37XU at SPring-8.* Jornal of Synchrotron Radiation, 2010. 17: p. 511-516.

62. Sanyal M.K., et al., *X-ray-scattering study of capillary-wave fluctuations at a liquid surface.* Phys Rev Lett, 1991. 66(5): p. 628-631.
63. Nevot L., et al., Rev. Phys. Appl., 1980. 15.
64. Wong J. Y., et al., *Polymer-Cushioned Bilayers. I. A Structural Study of Various Preparation Methods Using Neutron Reflectometry.* Biophysical Journal, 1999. 77: p. 1445-1457.
65. Nelson A., *Co-Refinement of Multiple-Contrast Neruton/X-ray reflctvity data using MOTOFIT.* Journal of Applied Crystallography, 2006. 39: p. 273-276
66. Saldit T., *Thermal Fluctuations and Stability of Solid-Supported Lipid Membranes.* J. Phys.: Condens. Matter, 2005. 17: p. 287-317.
67. Weinbach S. P., et al., *Self-assembled crystalline monolayers and multilayers of n-alkanes on the water surface.* Advanced Materials, 1995. 7(10): p. 857-862.
68. Jensen T. R., et al., *Novel methods for studying lipids and lipases and their mutual interaction at interfaces.* Part 2. Surface sensitive synchrotron X-ray scattering. Biochimie, 2001. 83(5): p. 399-408.
69. Nie H.-Y., et al., *Optical Properties of an Octadecylphosphonic Acid Self-Assembled Monolayer on a Silicon Wafer.* Thin Solid Films, 2008. 517: p. 814-818.
70. Woodward J. T., et al., *Self-Assembled Monolayer Growth on Cctadecylphosphonic Acid on Mica.* Langmuir, 1996. 12: p. 3626-3629.
71. Kuhl T. L., et al., *A Neutron Reflectivity Study of Polymer-Modified Phospholipid Monolayers at the Solid-Solution Interface: Polyethylene Glycol-Lipids on Silane-Modified Substrates.* Biophysical Journal, 1998. 75: p. 2352-2362.
72. Tipler P. A., et al., *Physics for Scientsts and Engineers: Mechanics, Oscillations and Waves, Thernodynamics*. Vol. 1. 2008: W.H. Freenan.
73. Fragneto G., et al., *Floating lipid bilayers: models for physics and biology.* Eur Biophys J, 2012. 41(10): p. 863-74.
74. Stidder B., et al., *Structure and Stability of DPPE planar bilayers.* Soft Mater, 2006. 3: p. 214-222.
75. Fragneto G., et al., *A Fluid Floating Bilayer.* Europhys. Lett., 2001. 53(1): p. 100-106.
76. Koltover I., et al., *Crystalline Sheets of the Membrane-Protein Bacteriorhodophsin: A Specular and Diffuse Reflectivity Study.* Phys. Rev. Lett, 1998. 81(12): p. 2494-2497.
77. Franks N. P., et al., *The Structure of Lipids Bilayers and the Effects of Generla Anaesthetics.* Journal of Molecular Biology, 1979. 133: p. 469-500.
78. Dante S., et al., *Isertion of Externlly Administered Anyloid Beta Peptide 25-30 and Perturbaion of Lipid Bilayer.* Biochemistry, 2003. 42: p. 13667-13672.
79. Buldt G., et al., *Neutron diffraction studies on phosphatidylcholine model membranes. I. Head group conformation.* J Mol Biol, 1979. 134(4): p. 673-91.
80. McIntosh T. J., et al., *Area per Molecule and Distribution of Water in Fully Hydrated Dilauroylphosphatidylethanolamine Bilayers.* Biochemistry, 1986. 25: p. 4948-4952.
81. Salditt T., et al., *Kinetic Roughness of Amorphous Multilayers Studied by Diffuse X-ray Scattering.* Physical Review Letters, 1994. 73(16): p. 2228-2231.
82. Salditt, T., et al., *Specular and diffuse scattering of highly aligned phospholipid membranes.* Physical Review E, 1999. 60(6): p. 7285-7289.
83. Safran S.A., *Curvature Elasticity of Thin Film.* Advances in Physics, 1999. 48(4): p. 395-448.

84. Jablin M.S., et al., *In-plane correlations in a polymer-supported lipid membrane measured by off-specular neutron scattering.* Phys Rev Lett, 2011. 106(13): p. 138101.
85. Nagle J.F. et al., *Structure of lipid bilayers.* Biochim Biophys Acta, 2000. 1469(3): p. 159-95.
86. Zarbakhsh A., et al., *A New Approach for Measuring Neutron Reflection from a Liquid/Liquid Interface.* Meas. Sci. Technol., 1999. 10: p. 738-743.
87. Clifton B. J., et al., *The Structure of Block Copolymers at the Fluid/Fluid Interface.* Physica B, 1998. 248: p. 289-296.
88. Lee L.T., et al., *Neutron reflectivity of an oil-water interface.* Phys Rev Lett, 1991. 67(19): p. 2678-2681.
89. Rappolt M., et al., *Structure and Elasticity of Phospholipid Bilayers in the Lα phase: a Comparison of Phosphatilylcholine and Phosphatidylethanolamine Membrane.* Recent Research Developments in Biophiscs, 2004. 3: p. 363-392.
90. Rappolt M., et al., *Flexibility and Structure of Fluid Bilayer Interfaces.* Structure and Dynamics of Membranous Interfaces, 2008: p. 45-81.
91. Lipowsky R., et al., *Unbinding Transitions of Interacting Memranes.* Phys. Rev. Lett, 1986. 56: p. 2541-2544.
92. Farrugia A., *Albumin usage in clinical medicine: tradition or therapeutic?* Transfus Med Rev, 2010. 24(1): p. 53-63.